Technische Universität München
TUM School of Medicine and Health

TUΠ

Characterization of the ubiquitin ligase FBXL6 as a novel vulnerability in acute myeloid leukemia

Anna Karolina Sperk

Vollständiger Abdruck der von der TUM School of Medicine and Health der Technischen

Universität München zur Erlangung einer

Doktorin der Naturwissenschaften (Dr. rer. nat.)

genehmigten Dissertation.

Vorsitz: Prof. Dr. Marc Schmidt-Supprian

Prüfer der Dissertation:

1.   Prof. Dr. Florian Bassermann
2.   Prof. Dr. Bernhard Küster

Die Dissertation wurde am 29.08.2023 bei der Technischen Universität München eingereicht

und durch die TUM School of Medicine and Health am 03.01.2024 angenommen.

Content

Abbreviations

°C	degree Celsius
3D	three-dimensional
aa	amino acid
ABL1	Abelson murine leukemia viral oncogene homolog 1
AEBSF	4-(2-aminoethyl)benzenesulfonyl fluoride hydrochloride
AF	Alexa Fluor
AHS	Apoptosis in Hematopoietic Stem Cells research unit
AML	Acute myeloid leukemia
AMP	adenosine monophosphate
APC	Allophycocyanin
APL	acute promyelocytic leukemia
APS	ammonium persulfate
ASXL1	additional sex combs-like 1 transcriptional regulator
ATP	adenosine-5'-triphosphate
ATRA	all-trans retinoic acid
BCL-2	B-cell lymphoma 2
BCOR	BCL6 corepressor
BCR	Breakpoint cluster region
BES	N,N-Bis(2-hydroxyethyl)-2-aminoethanesulfonic acid
BFP	blue fluorescent protein
Blast	blasticidin
BM	bone marrow
bp	base pair
BSA	bovine serum albumin
C-terminal	carboxy terminal
CAA	chloroacetamide
CatG	Cathepsin G
CBFB	core-binding factor subunit-β
CD11b	Cluster of differentiation molecule 11B
cDNA	complementary DNA
CEBPA	CCAAT/enhancer-binding protein-α
CHAPS	3-[(3-cholamidopropyl)dimethylammonio]-1-propanesulfonate
CHX	cycloheximide
cm	centimeter
CML	Chronic myeloid leukemia
Conc. FT	concentrator flow through
CPM	counts per million reads mapped
CRISPR	clustered regularly interspaced short palindromic repeats
CRL	cullin-RING ligase
CSF1R	Colony stimulating factor 1 receptor
Ctrl	control
CUL1	Cullin 1
Da	Dalton
DAVID	Database for annotation, visualization and integrated discovery
DFP	di-isopropyl fluorophosphate
dH$_2$O	distilled water
DiGly	Lysine-ϵ-Glycine-Glycine ubiquitin remnant motiv
DLBCL	diffuse large B-cell lymphoma
DMEM	Dulbecco's Modified Eagle's Medium
DMSO	dimethylsulfoxid
DNA	deoxyribonucleic acid

DNMT3A	DNA methyltransferase 3A
dNTP	2'-desoxynukleosid-5'-triphosphat
Doxy	doxycycline
Doxy	doxycycline
DSMZ	Deutsche Sammlung von Mikroorganismen und Zellkulturen
DTT	dithiothreitol
DUB	deubiquitinase
E. coli	Escherichia coli
e.g.	for example
ECL	enhanced chemiluminescence
EDTA	ethylenediaminetetraacetic acid
ELN	European LeukemiaNet
ETV7	ETS Variant Transcription Factor 7
EV	empty vector
EZH2	enhancer of zeste 2 polycomb repressive complex 2 subunit
FA	formic acid
FAB	French-American-British
FACS	fluorescence activated cell sorting
FBP	F-box protein
FBS	fetal bovine serum
FBXL	F-box and Leu-rich repeat
FBXL6ΔN	C-terminal fragment mutant of FBXL6
FBXO	F-box only
FBXW	F-box and WD40 domain
FC	fold change
Fig.	Figure
FL	FLAG
FLAG-Ida	Fludarabine, Cytarabine, G-CSF and Idarubicin
FlCy	flowcytometry
FLT3	FMS-related tyrosine kinase 3
FSC	forward scatter
fw	forward
G2P	beta-glycerolphosphate disodium salt hydrate
GAPDH	Glyceraldehyde 3-phosphate dehydrogenase
GC	guanine-cytosine
GFP	green fluorescent protein
Glu	glutamic acid
GO	gene ontology
h, hrs	hour, hours
h.i.	heat inactivation
H2B-Ub	ubiquitylated Histone H2B
HA	hemagglutinin
HECT	homologous to E6AP C-terminus
HR	Hazard ratio
HRP	horse radish peroxidase
HSC	Hematopoietic stem cell
HSCT	Hematopoietic stem cell transplantation
HSPCs	Hematopoietic stem/progenitor cells
IB	immunoblot
Ida	Idarubicin
IDH	isocitrate dehydrogenase
IF	immunofluorescence
IgG	Immunoglobulin G

IkB-a	NF-Kappa-B Inhibitor Alpha
IMDM	Iscove's Modified Dulbecco's Media
inc.	incubation
inhib.	inhibitor
IP	immunoprecipitation
ITD	internal tandem repeat
K	lysine
K-GG	Lysine-ϵ-Glycine-Glycine ubiquitin remnant motiv
kb	kilobase
kDa	kilodalton
KMT2A	Lysine Methyltransferase 2A
KO	knockout
KRAS	Kirsten rat sarcoma virus
l.e.	long exposure
LB	Luria-Bertani
LC	Liquid chromatography
Leu	leucine
LFQ	label-free quantification
LRR	leucine rich repeat
LSC	Leukemic stem cell
LuAD	Lung adenocarcinoma
Lys	lysine
M	molar
MCS	multiple cloning site
MECOM	MDS1 And EVI1 complex locus
min	minute
ml	milliliter
MLL	myeloid/lymphoid mixed-lineage leukemia
MLL	Münchner Leukämielabor
MM	multiple myeloma
mM	millimolar
MPI	Max Planck Institute
mRNA	messenger RNA
MRTFA	Myocardin-related transcription factor A
MS	mass spectrometry
MS/MS	tandem mass spectrometry
MTS	(3-(4,5-dimethylthiazol-2-yl)-5-(3-carboxymethoxyphenyl)-2-(4-sulfophenyl)-2H-tetrazolium)
MW	molecular weight
MYH11	myosin heavy chain 11 smooth muscle
n	number
N-terminal	amino terminal
NaCl	Sodium chloride
Nava	Sodium orthovanadate (Na_3VO_4)
NE	Neutrophil elastase
ng	nanogram
NGS	next generation sequencing
nM	nanomolar
NMM	4-Methylmorpholine
NPM1	nucleophosmin
NRAS	Neuroblastoma RAS
ns	not significant
NSG	NOD scid gamma

NT	non-targeting
NUP214	Nucleoporin 214
NUP98	Nucleoporin 98
oligo	oligonucleotide
P/S	penicillin-streptomycin
PAGE	polyacrylamide gel electrophoresis
PBS	phosphate buffered saline
PCR	polymerase chain reaction
PDX	patient-derived xenograft
PFA	paraformaldehyde
PHF6	PHD finger protein 6
PI	propidium iodide
pLDDT	per residue confidence score by Alphafold
PML	promyelocytic leukemia
PMSF	phenylmethanesulfonylfluoride
PPi	pyrophosphate
PPM1G	Protein phosphatase Mg2+/Mn2+ dependent 1G
PTM	post-translational modification
PVDF	polyvinylidene fluoride
qPCR	quantitative PCR
RARA	retinoic acid receptor-α
RBM15	RNA-binding motif protein 15
RBR	RING-between-RING
RBX1	RING-box protein 1
RING	really interesting new gene
RNA	ribonucleic acid
RNA-Seq	RNA sequencing
RNase	Ribonuclease
RPKM	Reads per kilobase of transcript per million reads mapped
RPLP0	ribosomal protein large subunit P0
rpm	revolution per minute
RPMI	Roswell Park Memorial Institute
RSEM	RNA-Seq by Expectaition-Maximization
RT	room temperature
RUNX1	Runt-related transcription factor 1
RUNX1T1	RUNX1 translocated to 1
rv	reverse
S.D.	standard deviation
s.e.	short exposure
SCF	SKP1-CUL1-F-box protein
SDS	sodium dodecyl sulfate
sec	second
Ser	serine
SF	Strep-FLAG
SF3B1	Subunit 1 of the splicing factor 3b protein complex
sgRNA	single guide RNA
shRNA	short hairpin RNA
SILAC	stable isotope labeling with amino acids in cell culture
SKP1	S phase kinase-associated protein 1
SKP2	S phase kinase-associated protein 2
SMC	structural maintenance of chromosomes protein
SRSF2	serine/arginine-rich splicing factor 2

SSC	sideward scatter
STAG2	stromal antigen 2
STAT5	Signal transducer and activator of transcription 5
Std.	standard
TAE	Tris base, acetic acid and EDTA
TAP	tandem-affinity purification
TCA	trichloroacetic acid
TCGA	The Cancer Genome Atlas
TEMED	N,N,N`,N``-tetramethyl-ethylenediamine
TET2	tet methylcytosine dioxygenase 2
TFA	Trifluoroacetic acid
Thr	threonine
TLCK	Nα-tosyl-L-lysine chloromethyl ketone hydrochloride
TP53	Tumorsuppressor 53
TPCK	N-p-tosyl-L-phenylalanine chloromethyl ketone
Tris	tris(hydroxymethyl)aminomethane
U2AF1	U2 small nuclear RNA auxiliary factor 1
UBQ/Ub	ubiquitin
UPS	ubiquitin proteasome system
USP	ubiquitin-specific protease
UV	ultraviolet
V	volt
VAF	Variant allele frequency
Val	valine
vs.	versus
WB	washing buffer
WCE	Whole-cell extract
WHO	World Health Organization
WT	wild type
WT1	Wilms tumour 1
xg	times gravity
β-TrCP	β-transducin repeat-containing protein
µg	microgram
µm	micrometer
µM	micromolar

1   Summary

Acute myeloid leukemia (AML) is a heterogeneous blood-borne malignancy and represents a particularly aggressive form of leukemia accounting for the majority of leukemic deaths (Park et al., 2020). Despite substantial genetic characterization in the last decades and the development of novel agents including FLT3 and IDH inhibitors, AML treatment still largely relies on chemotherapy and hematopoietic stem cell transplantation. Therefore, the identification of new actionable vulnerabilities is highly demanded. Investigating disease-specific post-translational modifications such as ubiquitylation holds great promise to provide new target structures in AML. In addition to the identification of the E3-ubiquitin ligase FBXL2 as a tumor suppressor in AML (B. B. Chen et al., 2012), the NEDD8 inhibitor pevonedistat showed promising results in clinical trials when combined with azacytidine in AML patients (Adès et al., 2022). NEDD8 inhibitors impair Cullin-dependent ubiquitin ligases, of which SKP1-CUL1-F-box (SCF) ligases represent the largest family, thus supporting the clinical relevance of these ligases in AML.

Aiming to uncover novel vulnerabilities in AML within the group of SCF ubiquitin ligases, CRISPR/Cas9-based screening identified the barely studied F-box protein FBXL6 as a potential dependency in AML. Analysis of over 1,000 ubiquitin-related genes in an AML patient cohort encompassing over 700 cases revealed that FBXL6 was one of the highest upregulated genes in AML, supporting a pro-tumorigenic role of FBXL6. In competition assays, FBXL6-depleted AML cells had a significant growth disadvantage compared to control cells, confirming the results of the pooled CRISPR/Cas9 screen. FBXL6 knockout impaired the proliferation of AML cells, while no increase in cell death, arrest in a specific cell cycle phase, or increased myeloid differentiation was observed. A patient-derived xenograft (PDX) mouse model suggested that FBXL6 might also be a dependency *in vivo*.

In search for ubiquitylation substrates of FBXL6, the systematic integration of four independent mass spectrometry-based interaction and ubiquitylation-specific functional screens identified the protein phosphatase PPM1G as the most promising candidate. Immunoprecipitation experiments confirmed the interaction between PPM1G and FBXL6 and *in-vivo*-ubiquitylation assays demonstrated that FBXL6 overexpression specifically increases PPM1G K63-linked poly-ubiquitylation. Preliminary studies to assess the functional consequences of FBXL6-mediated ubiquitylation of PPM1G precluded a change in the subcellular localization of PPM1G.

The AML-specific occurrence of an undescribed second form of FBXL6 instigated the analysis of up-stream regulatory processes of FBXL6. *In-vitro*-cleavage assays revealed protease-dependent processing of FBXL6 as the underlying cause. Combining top-down and bottom-up proteomics, the cleavage site was located between Leu47 and Ser50 in the N-terminal region of FBXL6. Database search for enzymes with a similar cleavage motif and functional annotation of the interactome screens identified Cathepsin G (CatG) as the FBXL6-directed protease. Similar to previous reports on CatG in AML (Schuster et al., 2007), the cleavage of FBXL6 unfortunately proved to be an artifact during standard cell lysis of myeloid cells without any biological relevance in living cells.

Taken together, this study describes FBXL6, a novel vulnerability in AML, which ubiquitylates PPM1G, and highlights the necessity to perform experiments in AML cells under special precautions to avoid artifacts through excessive proteolytic activity in cell lysates.

2   Introduction

2.1   Acute myeloid leukemia

Acute myeloid leukemia (AML) is an aggressive hematopoietic cancer characterized by rapid proliferation and accumulation of immature clonal hematopoietic cells in the bone marrow and blood (Döhner, Weisdorf, and Bloomfield 2015). Despite extensive research in the last decades, the current prognosis for patients is still extremely poor and new treatment options for this disease are urgently needed.

2.1.1   Epidemiology and pathogenesis

With an annual incidence of approximately 30 to 40 per million inhabitants in Western countries, AML is the most common acute leukemia affecting adults (Dong et al., 2020). While the disease occurs at all ages, the median age of diagnosis is approximately 70 years (Khwaja et al. 2016). AML is an aggressive disease with an overall 5-year survival rate of only 25 percent (Park et al., 2020). The prognosis varies widely depending on several factors, including age, cytogenetic and molecular abnormalities, and response to the initial therapy. While AML was regarded as an incurable disease till the 1960's (Khwaja et al., 2016), younger patients below the age of 65 have since then profited from advances in intensive chemotherapy and supportive care, resulting in a long-term survival rate of 45% (Owenberg et al., 2017). In contrast to that, elderly patients are often ineligible for intensive chemotherapy and have a particularly poor prognosis with a 5-year survival below 10% (Juliusson et al., 2012).

Table 1 Frequency of genetic changes in AML categorized into functional groups

Functional groups	Examples of mutated genes in AML	Frequency in patients with AML (%)
Signaling pathways	FLT3, KIT, KRAS, NRAS, Ser/Thr kinases	59
DNA methylation	DNMT3A, TET2, IDH1, IDH2	44
Chomatin modifiers	MLL (alias KMT2A) fusions, ASXL1, EZH2	30
Nucleophosmin	NPM1	27
Myeloid transcription factors	RUNX1, CEBPA	22
Transcription factors	PML-RARA, MYH11-CBFB, RUNX1-RUNX1T1	18
Tumor suppressors	TP53, WT1, PHF6	16
Spliceosome complex	SRSF2, U2AF1	14
Cohesin complex	STAG2, RAD21, SMC1, SMC3	13

AML, acute myeloid leukemia; ASXL1, additional sex combs-like 1 transcriptional regulator; CBFB, core-binding factor subunit-β; CEBPA, CCAAT/enhancer-binding protein-α; DNMT3A, DNA methyltransferase 3A; EZH2, enhancer of zeste 2 polycomb repressive complex 2 subunit; FLT3, FMS-related tyrosine kinase 3; IDH, isocitrate dehydrogenase; MLL, myeloid/lymphoid mixed-lineage leukemia; MYH11, myosin heavy chain 11 smooth muscle; NPM1, nucleophosmin; PHF6, PHD finger protein 6; PML, promyelocytic leukemia; RARA, retinoic acid receptor-α; RUNX1, Runt-related transcription factor 1; RUNX1T1, RUNX1 translocated to 1; SMC, structural maintenance of chromosomes protein; SRSF2, serine/arginine-rich splicing factor 2; STAG2, stromal antigen 2; TET2, tet methylcytosine dioxygenase 2; U2AF1, U2 small nuclear RNA auxiliary factor 1; WT1, Wilms tumour 1. Changes within a category are largely mutually exclusive. Table adapted from Khwaja et al. 2016.

Like other cancers, AML originates from abnormalities in cell proliferation, survival, and differentiation, which are caused by various genetic and epigenetic changes in the tumor cells (Khwaja et al., 2016). About half of all AMLs are characterized by gross structural cytogenetic changes such as translocations and chromosomal gains or losses (Mroźek et al., 2012). In general, AML genomes carry far fewer mutations than other cancers such as solid epithelial tumors (Weinstein et al., 2013). Typically, more than one cooperating mutation is required to induce AML, demonstrated by experimental data from leukemogenesis mouse models (Grisolano et al., 2003; Schessl et al., 2005). Affected genes are mostly found among the functional groups of transcription factors, epigenetic modifiers, and cell signaling pathways regulating proliferation and survival. Considerable genome sequencing efforts extended these functional categories by mutations in the cohesin complex and the spliceosome (Table 1) (Weinstein et al., 2013). The coexistence of these genetic changes in functionally distinct groups, which are acquired sequentially in a multistep process, affects various cellular functions and ultimately leads to a fully transformed malignancy (Khwaja et al., 2016). The extreme heterogeneity of AML is reflected by the characteristics of recurrent mutations. While next-generation sequencing of 200 adult AML samples identified nearly 2,000 different mutated genes, only 23 of them were frequently mutated. On average, 13 mutations were identified per patient with 5 of these in recurrently mutated genes. Importantly, most recurrent mutations were present in less than 10% of all patients, while only three genes (FLT3, NPM1, DNMT3A) were mutated in more than 25% of patients (Weinstein et al., 2013).
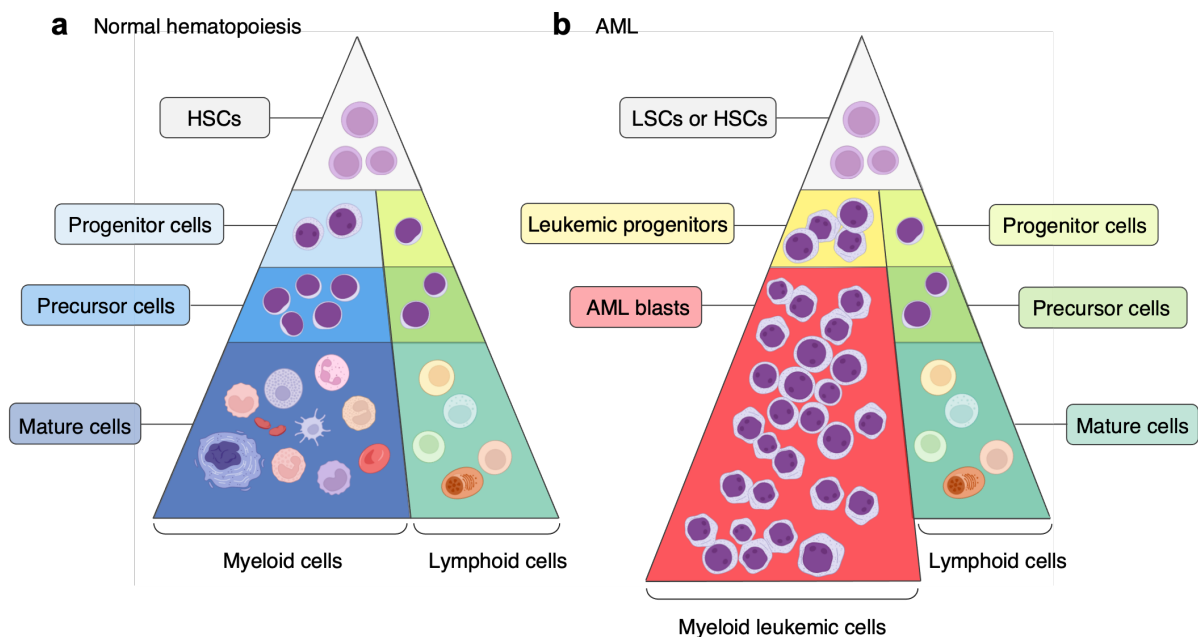
Figure 1 Normal and leukemic hematopoiesis. (a) The general hierarchical structure of normal hematopoiesis is shown. The long-term hematopoietic stem cells (HSCs), which have extensive self-renewal potential, give rise to various hematopoietic progenitor cells. These progenitor cells still have extensive proliferative capacity but have lost the ability to self-renew and are committed to one or more cell lineages. Progenitors produce various precursor cells and then mature hematopoietic cell types as indicated. **(b)** Aberrant hematopoiesis observed in acute myeloid leukemia (AML) is shown. Leukemic stem cells (LSCs) reside at the top of the developmental pyramid, giving rise to AML progenitor cells and the more mature (but still morphologically primitive) myeloid blast cells that make up the bulk of the neoplasm. Note the overall expansion of the hematopoietic cell mass. Lymphopoiesis is relatively preserved. Figure created with BioRender, adapted from Khwaja et al. 2016.

Cells with the potential for malignant myeloid transformation reside at the top of the hierarchical structure of normal hematopoiesis, comprising hematopoietic stem cells (HSCs) and myeloid progenitor cells. These cells harbor extensive proliferative capacity to fulfill the task of building and maintaining every type of mature blood cells under physiologic conditions. After acquiring genetic alterations that lead to uncontrolled proliferation and impaired differentiation, these cells become so-called leukemic stem cells or morphologically primitive myeloid blasts, which are more mature, that fill up the bone marrow and prevent normal hematopoiesis (Fig. 1) (Khwaja et al. 2016).

Beyond genetic and epigenetic aberrations, the resulting AML blasts are affected by the microenvironment, through direct or indirect contact with mesenchymal stem cells, exposure to cytokines and chemokines, and stimulation by the hypoxic milieu that exists within the AML remodeled bone marrow (Hu et al. 2019). Therefore, the biology of AML cells is a defined by combination of the pre-existing and acquired genetic and epigenetic changes and the environment the cell resides in. The possible combinations of alterations at each of these levels produce a seemingly infinite number of states and abnormalities, resulting in an extreme degree of heterogeneity (Hu et al., 2019).

2.1.2 Diagnosis and classification

AML typically manifests with nonspecific symptoms such as tiredness and a loss of appetite next to the characteristic features of bone marrow failure: fatigue and shortness of breath on exertion due to anemia, recurrent infections due to neutropenia, and an increased tendency for bruising or bleeding due to thrombocytopenia (Khwaja et al., 2016). A complete blood count is therefore an initial step in the diagnosis of the disease. For a definite diagnosis and the definition of AML subtypes, the diagnostic procedures comprise morphologic assessment of bone marrow aspirates and blood smears, analysis of cell-surface markers by flow cytometry, conventional cytogenetic testing, and molecular screening for characteristic genetic lesions (Döhner et al., 2015).

Historically, AML diagnosis and classification were solely based on cellular morphology within the French-American-British (FAB) classification (Bennett et al., 1976). Integrating genetic criteria with morphological and cytochemical characteristics, AML subtypes are now defined by the World Health Organization (WHO) classification system of hematolymphoid tumors (Khoury et al., 2022). The recently published 5th edition separates two distinct families: i) AML with defining genetic abnormalities comprising 13 subtypes, and ii) AML defined by differentiation with 8 subtypes resembling the previous FAB classification (Table 2). Especially the classification into genetic subtypes provides important prognostic information and is used to guide therapeutic decisions. Risk stratification of AML patients into the three groups 'favorable', 'intermediate', and 'adverse' is commonly assessed by genetics at initial diagnosis according to the European LeukemiaNet (ELN) guidelines (Döhner et al., 2022). Cytogenetics play an essential role in the stratification guidelines: gene fusions such as RUNX1::RUNX1T1 or CBFB::MYH11 define a favorable prognosis, while other chromosomal rearrangements and a complex karyotype are defined as adverse risk. Molecular abnormalities in the genes NPM1 and CEBPA can positively affect the outcome, while mutations in the FLT3 gene, which cause an internal tandem repeat (FLT3-ITD), and mutations in several other genes (ASXL1, BCOR, EZH2, RUNX1, SF3B1, SRSF2, and or others) indicate a worse prognosis (Döhner et al., 2022).

Table 2 Subtypes of AML according to the World Health Organization (WHO) classification system

AML with defining genetic abnormalities
APL with PML::RARA fusion
AML with RUNX1::RUNX1T1 fusion
AML with CBFB::MYH11 fusion
AML with DEK::NUP214 fusion
AML with RBM15::MRTFA fusion
AML with BCR::ABL1 fusion
AML with KMT2A rearrangement
AML with MECOM rearrangement
AML with NUP98 rearrangement
AML with NPM1 mutation
AML with CEBPA mutation
AML myelodysplasia-related
AML with other defined genetic alterations

AML, defined by differentiation
AML with minimal differentiation
AML without maturation
AML with maturation
Acute basophilic leukemia
Acute myelomonocytic leukemia
Acute monocytic leukemia
Acute erythroid leukemia
Acute megakaryoblastic leukemia

AML, acute myeloid leukemia; APL, acute promyelocytic leukemia; ABL1, Abelson murine leukemia viral oncogene homolog 1; BCR, Breakpoint cluster region; CBFB, core-binding factor subunit-β; CEBPA, CCAAT/enhancer-binding protein-α; KMT2A, Lysine Methyltransferase 2A; MECOM, MDS1 And EVI1 complex locus; MRTFA, Myocardin-related transcription factor A; MYH11, myosin heavy chain 11 smooth muscle; NPM1, nucleophosmin; NUP214, Nucleoporin 214; NUP98, Nucleoporin 98, PML, promyelocytic leukemia; RARA, retinoic acid receptor-α; RBM15, RNA-binding motif protein 15; RUNX1, Runt-related transcription factor 1; RUNX1T1, RUNX1 translocated to 1; Table adapted from Khoury et al. 2022.

2.1.3 Current treatment

The general therapeutic strategy for AML patients consists of induction therapy followed by consolidation and maintenance phases which have not changed substantially in the past decades. Despite recent advancements in targeted therapies using for example FLT3 and IDH inhibitors as well as hypomethylating agents, the current disease management still largely depends on classical chemotherapy and allogeneic hematopoietic stem cell transplantation (HSCT) (Park et al., 2020).

The standard induction therapy consists of the pyrimidine analog cytarabine for 7 days combined with an DNA-interclating anthracycline (usually daunorubicin or idarubicin) for 3 days which is termed '7 plus 3' and was first described in 1973 (Lichtman, 2013). Alternatively, FLAG-Ida is applied for remission induction, where fludarabine and granulocyte colony-stimulating factor are added on top of high-dose cytarabine and idarubicin (Khwaja et al., 2016). The tolerated dose intensity of this cytotoxic chemotherapy varies with the performance status of the patient which is strongly linked to age. Even though induction therapy achieves complete remission in 60-80% of patients younger than 60 years, most patients eventually relapse (Daver et al., 2020). To decrease the risk of relapse, consolidation therapy with lower doses of chemotherapy and/or HSCT is applied. HSCT reduces relapse rates and prolongs remission, which can be attributed to the beneficial graft-versus-leukemia effect exerted by allogeneic donor T cells and natural killer cells (Dickinson et al., 2017). However, HSCT is associated with elevated treatment-related mortality and is only chosen

for consolidation therapy in adverse-risk and a fraction of intermediate-risk AML patients who can tolerate the transplant and have a suitable donor (Döhner et al., 2015; Park et al., 2020).

In the last decade, treatment options could be improved by novel, more targeted therapies, including inhibitors of FLT3 (midostaurin, gilteritinib), IDH (enasidenib, ivosidenib), and BCL-2 (venetoclax) (Daver et al., 2020; Park et al., 2020). FLT3 and IDH inhibitors are now used in combination with intensive chemotherapy of younger patients with the respective genetic characteristics. For older patients, venetoclax can be used on top of low-dose chemotherapy and/or a hypomethylating agent like azacytidine (Park et al., 2020). Survival rates of both younger and older AML patients have increased dramatically in past decades, which is however not clearly attributed to the development of novel agents but rather the result of improved supportive care, better strategies for chemotherapy, and advances in HSCT (Burnett & Stone, 2020; Rowe, 2019).

There is only one subtype of AML that is considered curable: acute promyelocytic leukemia (APL) which is characterized by gene fusions of the retinoic acid receptor alpha (RARA) to other genes such as the promyelocytic leukemia gene PML, resulting in PML-RARA (Khwaja et al., 2016). The accompanied differentiation block can be reversed by all-trans retinoic acid (ATRA), which leads to ubiquitin-dependent degradation of the PML-RARA fusion protein and subsequently cell cycle arrest (Thomas, 2019). Even though AML is generally characterized by a differentiation block combined with uncontrolled proliferation of myeloid cells, differentiation therapy was not found to be efficient in other subtypes than APL (Koeffler, 2010; Thomas, 2019).

Taken together, thorough genomic characterization of AML has led to sophisticated risk stratification and more personalized treatment strategies. However, most patients will eventually relapse and die from this disease, resulting in a strong need for the identification of novel cellular targets that define true and non-redundant vulnerabilities in AML.

2.2   Protein ubiquitylation

Protein ubiquitylation is one of the major post-translational modifications in cells and enables rapid and reversible adjustments in protein networks to orchestrate key dimensions of cellular life including proliferation, survival, and differentiation (Hershko & Ciechanover, 1998; Komander & Rape, 2012). The covalent attachment of the highly conserved 8.5 kDa protein ubiquitin (Ub) to a target protein can lead to tremendous changes in its abundance, activity, interaction behavior, or cellular localization (Komander, 2009). Thousands of proteins have been found to be ubiquitylated by enzymes called ubiquitin ligases, emphasizing the significance of this modification (W. Kim et al., 2011). The adaptivity of the protein ubiquitylation system is accomplished by deubiquitinating enzymes (DUBs), which counteract ubiquitin ligases by erasing or modifying attached Ub. Deregulation of the ubiquitylation machinery has been reported to be associated with various diseases including cancer (Bassermann et al., 2014; Komander, 2009; Z. Wang et al., 2014).

The attachment of Ub is achieved by a three-step enzymatic cascade (Fig. 2). First, a Ub monomer is activated in an ATP-dependent manner by the ubiquitin-activating enzyme (E1) resulting in a highly reactive thioester bond between E1 and Ub. In the next step, activated Ub is transferred to a conserved cysteine residue of the ubiquitin-conjugating enzyme (E2). Finally, the E3 ubiquitin ligase specifically recognizes target proteins and

attaches Ub to a substrate by forming an isopeptide bond between the ε-amino group of the substrate and the free carboxyl group of the Ub C-terminus (Hershko & Ciechanover, 1998; Scheffner et al., 1995). Substrate proteins are typically ubiquitylated on lysine residues (Lys or K), while attachment to the N-terminal methionine has also been observed occasionally (Ciechanover & Ben-Saadon, 2004). Ubiquitin itself carries seven lysine residues (K6, K11, K27, K29, K33, K48, and K63), which can be connected to other Ub moieties to form polyubiquitin chains (Dammer et al., 2011). Depending on which lysine is used for attachment, the resulting chain type determines the consequences of polyubiquitylation by its architecture. The emerging complexity of protein ubiquitylation seems endless: next to homogenous polyubiquitin chains there can be mixed chains; branched topologies can be formed by attaching Ub moieties to more than one lysine of another Ub; monoubiquitylation can occur once or multiple times on one substrate protein (Komander & Rape, 2012; Swatek & Komander, 2016). However, the most abundant linkage type found in cells is K48 polyubiquitylation, which typically marks the substrate protein for degradation by the 26S proteasome (Dammer et al., 2011; Komander, 2009). Acting as a protein recycling machine, the 26S proteasome is a large multiprotein complex, which facilitates the recognition of polyubiquitylated proteins, the removal of Ub-moieties, and the unfolding and proteolytic cleavage of target proteins into peptides with the size of 7-9 amino acids (Coux et al., 1996). The second most common linkage type is formed via K63, which was found to have pleiotropic non-degradative functions including protein sorting and inflammation (Bhoj & Chen, 2009; Hicke & Dunn, 2003).
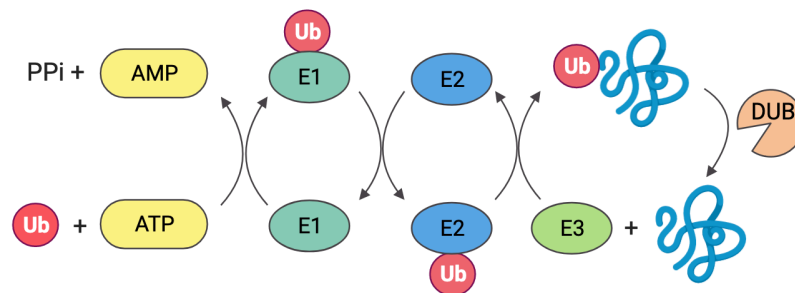
Figure 2 The enzymatic cascade of protein ubiquitylation. First, ubiquitin (Ub) is activated in an ATP-dependent manner and covalently attached to the ubiquitin-activating enzyme (E1) resulting in a highly reactive thioester bond. Next. the ubiquitin molecule is transferred to the catalytic cysteine of the ubiquitin-conjugating enzyme (E2), which recruits an E3 ligase which mediates the transfer of ubiquitin to a lysine amino acid residue of the substrate protein (depicted as a polypeptide in blue) or a ubiquitin molecule already attached to it. Ubiquitin-moieties can be removed from the substrate by deubiquitinating enzymes (DUBs) via proteolytic cleavage. ATP, adenosine-5'-triphosphate; AMP, adenosine monophosphate; PPi, pyrophosphate.

2.2.1 SCF-type E3 ubiquitin ligases

While only two E1 and approximately 40 different E2 enzymes exist in human cells, there are over 600 E3 ubiquitin ligases that confer substrate specificity to the ubiquitylation system (Buetow & Huang, 2016). According to their protein structure and mode of ubiquitin transfer, E3 ligases are grouped into three families: the RING (really interesting new gene), HECT (homologous to E6AP C-terminus), and RBR (RING-between-RING) types. HECT and RBR enzymes first bind directly to Ub before transferring it to a substrate, whereas RING-type ligases mediate ubiquitylation of a substrate by bringing it in close proximity to the E2 enzyme (Buetow & Huang, 2016; Hershko & Ciechanover, 1998). RING-type ligases that are

built on a cullin scaffold (cullin-RING ligases, CRL; Fig. 3) represent the largest family of E3 ligases (Sarikas et al., 2011). Depending on which of the eight cullin proteins encoded in the human genome is used, different multisubunit CRLs can be formed.

The best characterized CRL is the S phase kinase-associated protein 1 (SKP1)-cullin 1 (CUL1)-F-box protein (SCF) complex, which has a defined modular structure: CUL1 binds the RING domain protein RBX1 with its C-terminus to recruit the E2 enzyme. With the N-terminus, CUL1 binds to SKP1 which acts as an adaptor for recruiting one of 72 different F-box proteins (Bai et al., 1996; Petroski & Deshaies, 2005). Shared by all F-box proteins is the F-box domain, which measures approximately 50 amino acids and serves as an interface for binding SKP1 (Kipreos & Pagano, 2000). The remaining part of F-box proteins harbors different domains for substrate binding that can be classified into three subgroups: leucine-rich repeats (LRR)-containing (FBXLs), WD40-containing domains (FBXWs), and other domains (F-box only, FBXOs) (Jin et al., 2004). Substrate proteins are recognized at short conserved amino acid sequences, so-called degrons. To rapidly respond to stimuli by ubiquitylation, the binding between F-box protein and the substrate is tightly regulated, which often happens via phosphorylation of the substrate at the degron-motif (Skaar et al., 2013). One of the best characterized F-box proteins that binds to such phosphodegrons is β-transducin repeat-containing protein (β-TrCP/FBXW1), which targets several substrate proteins for proteasomal degradation by K48-ubiquitylation (Cardozo & Pagano, 2004; Lau et al., 2012). The most common linkage type transferred by SCF-type ligases is K48, however, several F-box proteins have recently been described to mediate non-proteolytic K63-ubiquitylation (Bassermann et al., 2014; Jiang et al., 2022; Li et al., 2018; Yao et al., 2018).
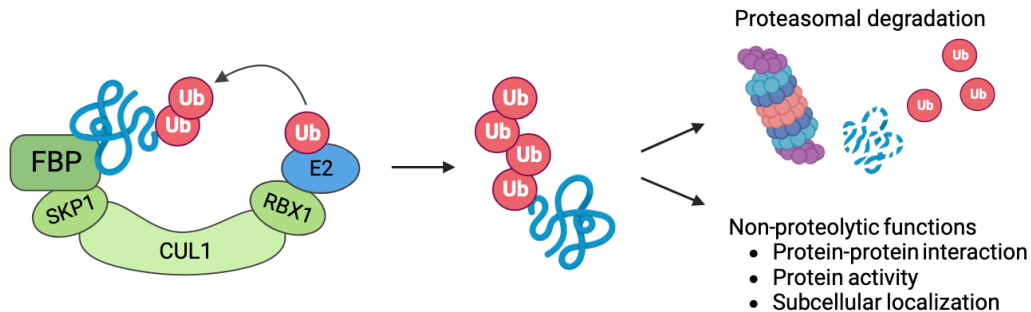
Figure 3 SCF complex-mediated (poly-)ubiquitylation and its consequences. The SKP1-cullin 1 (CUL1)-F-box protein (FBP) complex, short SCF complex, is composed of the large scaffold protein CUL1, which binds via its C-terminal part to the RING domain protein RBX1. At its N-terminus, CUL1 associates with the adaptor protein SKP1, which recruits one of 72 different F-box proteins by binding to the F-box domain. As substrate receptors of the complex, F-box proteins specifically bind to a subset of substrate proteins and ubiquitin (Ub) is eventually transferred from the RBX1-bound E2 enzyme onto the substrate or a ubiquitin molecule already attached to it. (Poly-)ubiquitylation of proteins can lead to degradation via the 26S proteasome (depicted in its barrel-like structure) or to non-proteolytic effects such as changes in protein-protein interaction, protein activity or subcellular localization.

Depending on the type of ubiquitylation, F-box proteins can have dramatic effects on the protein abundance or cellular function of their substrates. For substrate proteins involved in cancer-relevant pathways such as proliferation and survival, dysregulation of the respective regulatory SCF complex has been found to drive tumor development and progression (Tekcham et al., 2020; Z. Wang et al., 2014). For instance, the F-box protein SKP2 was found to be a potential oncogene by targeting the key cell cycle regulators p27 and p21 for proteasomal degradation (Carrano et al., 1999; Z. K. Yu et al., 1998). Besides oncogenic

properties, SCF complex components can also exert tumor-suppressive functions. By targeting oncogenes like MYC and cyclin E for proteasomal degradation, FBXW7 functions as a tumor suppressor in different types of cancer (Lau et al., 2012; Yada et al., 2004). As to hematologic cancers, implications of SCF complexes have predominantly been described for lymphoid malignancies such as DLBCL and multiple myeloma (Baumann et al., 2014; Q. Chen et al., 2008; Fernández-Sáiz et al., 2013). Nevertheless, selected reports have provided insights into the roles of SCF complexes in AML. By destabilizing cyclin D2, FBXL2 was described to have an antiproliferative function and act as a tumor suppressor in AML (B. B. Chen et al., 2012). Furthermore, the NEDD8 inhibitor pevonedistat demonstrated promising results in clinical trials when combined with azacytidine in AML patients (Adès et al., 2022). Notably, NEDD8 inhibitors impair the activation of CRL complexes, thereby supporting the clinical relevance of SCF ligases in AML.

Even though several SCF complexes have been functionally investigated including the identification of their substrate, most of the 72 human F-box proteins are only rudimentarily characterized, and identification of their ubiquitylation targets is still pending.

2.2.2 The human F-box protein FBXL6

FBXL6 is one of the barely studied F-box proteins, which was first identified and cloned in 1999 (Cenciarelli et al., 1999; Winston et al., 1999). As an evolutionarily conserved member of the FBXL family, it contains the typical F-box fold near the N-terminus, while the C-terminal part comprises twelve LRR domains (Winston et al., 1999). The FBXL6 gene on chromosome 8q24.3 encodes two isoforms, of which isoform 1 is the canonical form and harbors 539 amino acids (aa) resulting in a predicted molecular weight of approximately 59 kDa. The second isoform is generated by alternative splicing and lacks seven amino acids (aa 208-213) inside the second LRR domain (Bateman et al., 2023). FBXL6 is expressed across all human tissues and protein/mRNA expression data from cancer cell lines deposited on the Human Protein Atlas indicates low cancer specificity (Uhlén et al., 2015).

An initial report on the biological function of FBXL6 showed that ectopic expression of FBXL6 caused increased E2F-regulated transcription in colorectal cancer cells using a fluorescence-based reporter assay, hinting at a potential oncogenic role of FBXL6 in the cyclin-dependent cell cycle regulation (J. T. Kim et al., 2003). First mechanistic insights into FBXL6 function were obtained by researchers investigating transcription factors of the ETS family (derived from the erythroblastosis virus) from human cells and the fruit fly *Drosophila melanogaster*. In a yeast-two-hybrid screen, FBXL6 was identified as interaction partner of Tel (ETV6) and subsequent experiments in the human osteosarcoma cell line U2OS indicated ubiquitylation of Tel and the related transcription factor Tel2 (ETV7) by FBXL6 and its *Drosophila* homologue (Roukens et al., 2008). Even though no functional experiments were performed, these preliminary results provide a link between FBXL6 and the regulation of differentiation and proliferation by transcription factors. Regarding its function as the substrate recognition adaptor of an SCF-type E3 ligase, a cytokine receptor-based two-hybrid screen in HEK293 cells identified FBXL6 as an interaction partner of SKP1 (Lievens et al., 2009) and a mass spectrometry-based approach revealed binding of FBXL6 to immunoprecipitated FLAG-tagged CUL1 (Reitsma et al., 2017). Since concrete mechanistic and disease-specific information is absent, FBXL6 remains an understudied F-box protein which likely confers substrate specificity to an SCF complex.

2.3 Previous data on this project

Aiming to identify novel vulnerabilities in AML within the SCF-type family of ubiquitin ligases, Dr. David Brockelt initiated this project in the group of Prof. Dr. Florian Bassermann. The following section will present relevant data generated before the project was handed over to be the main topic of this thesis.

2.3.1 CRISPR/Cas9 screening identified FBXL6 as novel dependency in AML cell lines

In search for dependencies in AML within the F-box protein family, an unbiased pooled CRISPR/Cas9 screen was conducted using two independent, custom-assembled sgRNA
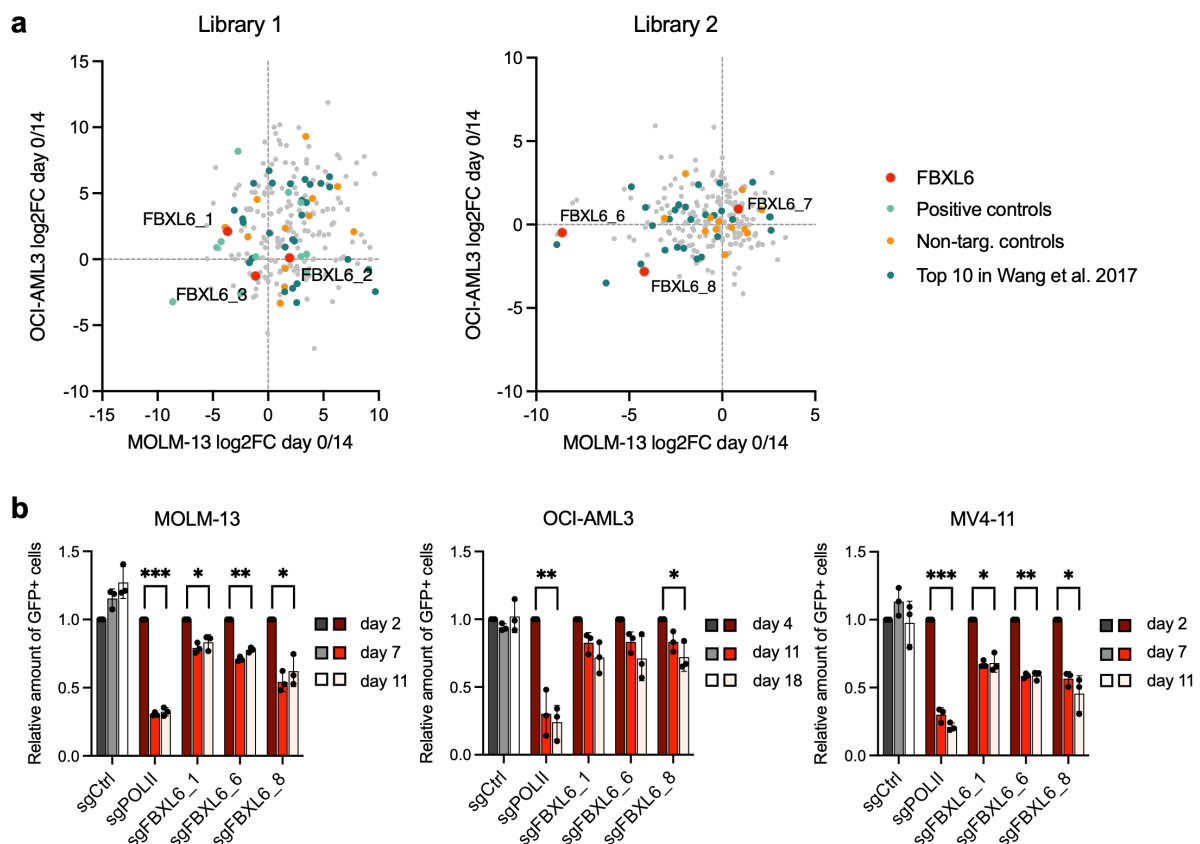
Figure 4 CRISPR/Cas9 screening identifies FBXL6 as novel dependency in AML cell lines. (a) CRISPR/Cas9 screen results from two independent, custom-designed sgRNA libraries targeting all 72 human F-box proteins with six sgRNA sequences per gene (three sgRNAs per library). Non-targeting sgRNAs were included as negative controls, positive controls targeted core essential genes like polymerases. Additional positive controls were the top 10 F-box genes from a whole-genome CRISPR screen published by T. Wang et al. performed in 14 AML cell lines (T. Wang et al., 2017). Cas9-expressing OCI-AML3 and MOLM-13 cells were lentivirally transduced with the pooled libraries and sorted for GFP (green fluorescent protein) positive cells. Samples taken on day 0, and day 14 were subjected to next-generation sequencing (NGS) analysis. Fold changes between day 0 and day 14 for each sgRNA were calculated from normalized log2 transformed read counts. sgRNAs showing a dropout in both cell lines are found in the lower left quadrant of each plot. **(b)** Competitive growth assay for CRISPR/Cas9 screen validation. Cas9-expressing AML cell lines were transduced with the individual sgRNAs targeting FBXL6 (sgFBXL6) or POLII (sgPOLII), or non-targeting control (sgCtrl) at 30-50% efficiency. The ratio of sgRNA expressing/GFP positive to non-transduced cells was measured by flow cytometry at the indicated time points after infection and normalized to day 2 or day 4, respectively. A dropout below 80% on the last day of measurement compared to the initial day is marked by red bars. ***; $P < 0.001$; **, $P < 0.01$; *, $P < 0.05$, by One sample t-test. [Data for a provided by R. Öllinger and T. Engleitner; Data in b provided by D. Brockelt]

libraries targeting all 72 human F-box proteins with three sgRNA sequences per gene in each library. The sgRNA sequences were extracted from the GeCKO v2 library (Sanjana et al., 2014) and cloned for library assembly by former lab member Dr. Oleksandra Karpiuk. Non-targeting sgRNAs were included as negative controls, while sgRNAs targeting core essential genes like polymerases, and hits from a whole-genome CRISPR screen published by T. Wang et al. performed in 14 AML cell lines (T. Wang et al., 2017) served as positive controls for dependencies. To exclude cell line-specific effects, two Cas9-expressing AML cell lines with different genetic aberrations were lentivirally transduced with the pooled libraries and cultured for 14 days. Comparative next-generation sequencing (NGS) of samples taken on day 0, which reflected the library composition, and day 14 revealed FBXL6 as one of the most essential hits in both OCI-AML3, harboring mutations in NPM1 and DNMT3A, and MOLM-13, an FLT3-ITD positive cell line (Fig. 4a). For validation of the screen results, AML cells were transduced with the individual sgRNAs targeting FBXL6 at 30-50% efficiency. Competitive growth assays of transduced (GFP+) versus non-transduced (GFP-) cells visualized by flow cytometry confirmed the dropout of FBXL6-depleted cells from the mixed population found in the screen (Fig. 4b). Being nearly uncharacterized at the time of performing the initial experiments of the project, FBXL6 was considered a highly interesting novel dependency in AML and was chosen for further investigations.

2.3.2 FBXL6 was found in nuclear fractions of AML cell lines

To functionally characterize FBXL6, first experiments regarding the subcellular localization of FBXL6 and its potential ubiquitylation substrates as an E3 ubiquitin ligase were conducted.

Investigating the location of FBXL6 within AML cells, subcellular fractions were prepared from three different cell lines and subjected to immunoblot analysis. For all cell lines tested, FBXL6 was found in the nuclear fractions and not in lysates from the cytoplasm (Fig. 5). While OCI-AML3 and MV4-11 showed FBXL6 in the insoluble nuclear fraction, which comprises chromatin and nuclear membranes, FBXL6 from HL-60 cell was detected in the soluble nuclear fraction, providing a first hint that FBXL6 resides in the nucleus of AML cells.
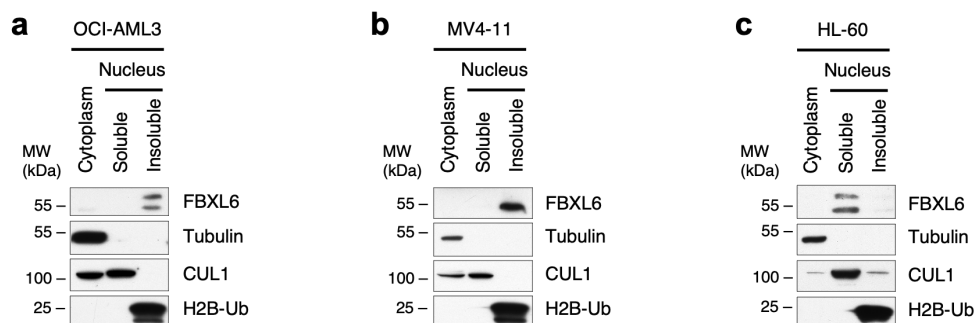
Figure 5 FBXL6 is found in nuclear fractions of AML cell lysates. (a-c) Immunoblot analysis of cytoplasmic and nuclear fractions prepared from OCI-AML3 (a), MV4-11 (b), and HL-60 (c) cell lines. Tubulin, Cullin-1 (CUL1), and H2B-Ub (ubiquitylated Histone H2B) served as controls for pure cellular fractions. [Data in a-c provided by D. Brockelt]

2.3.3 Mass spectrometry-based screening for FBXL6 ubiquitylation substrates

F-box proteins typically act as substrate recognition adaptors for SCF-type ubiquitin ligases. For the identification of ubiquitylation substrates of FBXL6, a combination of i) interactome screening for physical interaction partners, and ii) functional screening for ubiquitylation targets was employed.

To search for physical interaction partners of FBXL6, affinity purification of overexpressed FBXL6 with subsequent mass spectrometric analysis was performed. In the first experiment, Strep-FLAG-FBXL6 (SF-FBXL6) or empty vector control (EV) were transiently overexpressed in HEK293T cells, a cell line derived from human embryonic kidney cells widely used as a protein production machinery. The applied dual tag allowed for a tandem-affinity purification (TAP) using Strep-Tactin and anti-FLAG coupled beads to improve the signal to noise ratio. In a second experiment, the AML cell line HL-60 was transduced with FLAG-tagged FBXL6 (FL-FBXL6), or EV for stable overexpression. Cells were harvested in triplicates to perform single-FLAG immunoprecipitation (FLAG-IP). For both experiments, successful overexpression, and purification of FBXL6 were confirmed using immunoblot analysis and silver staining of inputs and eluted proteins (Fig. 6a, b, d, f). Subsequent mass spectrometric analysis yielded 405 proteins for the TAP experiment, and 328 proteins for the FLAG-IP which were specifically enriched (log2FC > 2) in the FBXL6 sample versus empty vector control (Fig. 6c, e). Among the interacting proteins, the SCF-complex components SKP1 and CUL1 were found, suggesting FBXL6 indeed acts as the substrate recognition adaptor of an E3 ubiquitin ligase.

To cross-validate the lists of interacting proteins with ubiquitylation-specific functional data, another mass spectrometry-based screen was set up, in which all ubiquitylated proteins were purified from cells with and without FBXL6 knockdown. For this purpose, MOLM-13 cells were grown in SILAC (stable isotope labeling with amino acids in cell culture) medium until fully labeled and transduced with shRNA constructs targeting FBXL6 versus non-targeting control. Depletion of FBXL6 was validated using qPCR on the third day after transduction before harvesting the cells on the next day (Fig. 6g). Following cell lysis and trypsin-digest of all proteins, ubiquitin-remnant peptides characterized by the Lysine-ϵ-Glycine-Glycine (K-GG or DiGly) motif were purified using immunoprecipitation (IP) and analyzed by mass spectrometry (Fig. 6h). Quantification of peptides not bound to the beads during immunoprecipitation (flow through) was used to identify proteins regulated by FBXL6 depletion and to normalize values from the DiGly-IP to total protein abundance, yielding 191 proteins to be less ubiquitylated in the shFBXL6 sample compared to control (cut-off 30% less ubiquitylation in at least one ubiquitin-remnant peptide).

The substrate screens described above were performed by Dr. David Brockelt during the final weeks of his affiliation with the group of Prof. Dr. Florian Bassermann. The project was handed over during the bioinformatic workup of the mass spectrometric data done by the collaboration partners at the chair of Proteomics at TUM headed by Prof. Dr. Bernhard Küster. The integrative data analysis and cross-validation of potential ubiquitylation substrates are therefore included in the main part of this thesis.
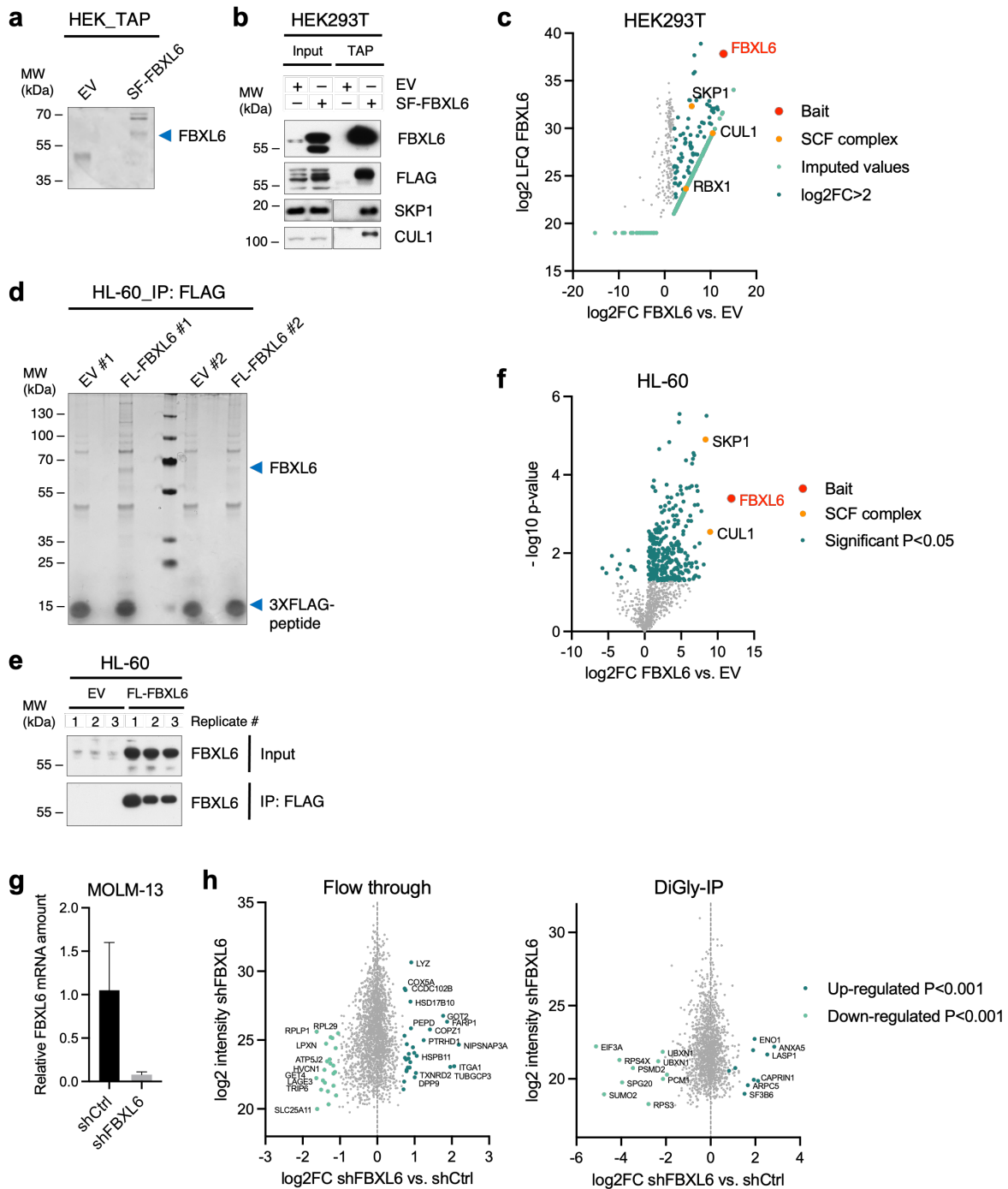
Figure 6 Mass spectrometry-based screening for FBXL6 ubiquitylation substrates. (a) Silver staining, **(b)** immunoblot, and **(c)** mass spectrometric (MS) analysis of tandem affinity purification (TAP) of Strep-FLAG-tagged FBXL6 (SF-FBXL6) from transfected HEK293T cells. After immobilization on Strep-Tactin beads and elution with desthiobiotin in the first step, FBXL6 was immunoprecipitated with anti-FLAG resin and eluted with 3XFLAG octapeptide in the second step. Empty vector (EV) served as control for background signal. 2.5% of the final elution was separated by SDS-PAGE and visualized by silver staining (a) and immunoblot analysis (b). **(d)** Silver staining, **(e)** immunoblot, and **(f)** MS analysis of FLAG immunoprecipitation (FLAG-IP) of FLAG-tagged FBXL6 (FL-FBXL6) versus EV control from HL-60 cells transduced for stable overexpression. After FLAG-IP an elution with 3XFLAG peptide, 2.5% of the eluates were separated by SDS-PAGE and visualized by silver staining (d) and immunoblot analysis (f). **(g)** Relative quantification of FBXL6 mRNA levels from MOLM-13 cells transduced with shRNA constructs for FBXL6 or non-targeting control on day 3 after infection. **(h)** MS analysis of immunoprecipitated ubiquitin-remnant peptides (DiGly-IP, right panel) and peptides from the flow through (left panel) from MOLM-13 cells in (g) on day 4 after infection. FC, fold change; LFQ, label-free quantification intensity; SCF, SKP1-CUL1-F-box protein complex. MS data represents either single peptides (h) or proteins (c, f) by the mean of corresponding peptides. [Data for a, b, d, f, g provided by D. Brockelt; Data for c, e, h provided by Prof. B. Küster, J. Zecha and J. Krumm.]

13

2.4   Aim of this study

Acute myeloid leukemia (AML) is a particularly aggressive form of leukemia, accounting for the majority of leukemic deaths (Park et al., 2020). Substantial genetic characterization of this disease has led to risk stratification strategies and decision-making algorithms as to whether to include allogeneic transplantation on top of classical chemotherapeutic regimens. However, true vulnerabilities and novel targeted treatment approaches based on genetic information have largely failed to evolve (Burnett & Stone, 2020). Therefore, investigating post-translational mechanisms such as ubiquitylation holds great promise to identify new actionable vulnerabilities in AML. Given that the NEDD8 inhibitor pevonedistat demonstrated promising results in clinical trials when combined with azacytidine in AML patients (Adès et al., 2022), searching for vulnerabilities among ubiquitin ligases of the SCF-type seems to hold great potential. To kick off this project, Dr. David Brockelt conducted a CRISPR/Cas9 dropout screen in AML cell lines, which identified the barely studied F-box protein FBXL6 as one of the most significant hits. Preliminary characterization of FBXL6 in AML pointed toward a nuclear localization and a functional SCF complex assembly due to the interaction with SKP1 and CUL1. Since E3 ubiquitin ligases exert their biological function through post-translational modification of their respective substrates, identification thereof was initiated by performing mass spectrometry-based screens that were still analyzed by collaboration partners when the project was handed over.

The aims of this study were therefore, i) to characterize the role of FBXL6 as a novel vulnerability in AML by analysis of primary patient samples, tissue culture models, and *in-vivo* model-based experiments, ii) to identify ubiquitylation substrates of FBXL6 by systematic integration of mass spectrometry-based interaction and functional screens with validation of the newly identified ligase-substrate pair(s), and iii) to delineate up-stream regulatory mechanisms of FBXL6 which contribute to its function in AML.

3   Material and methods

3.1   Material

3.1.1   Devices and Instruments

Agilent 1100 HPLC column	Agilent Technologies
Aqualine water bath	Lauda-Brinkmann
Axiovert 40 CFL with HBO50	Carl Zeiss
Mini-Sub® Cell GT system for agarose electrophoresis	Bio-Rad Laboratories
BioSAFE SC-smart CHRONOS 220	Cryotherm
BransonSonifier 250	Heinemann
Centrifuge 5417R with rotor F453011	Eppendorf
Centrifuge 5424 with rotor FA452411	Eppendorf
Concentrator plus	Eppendorf
Curix 60	Agfa
Dionex Ultimate 3000 RSLCnano	Thermo Fisher Scientific
ENVAIReco safe Comfort Sterilwerkbänke	ENVAIR
Exploris 480 mass spectrometer	Thermo Fisher Scientific
FACS Accuri C6 plus	BD Biosciences
FACS Calibur	BD Biosciences
FACS Aria Fusion	BD Biosciences
Fridges and lab freezers	Liebherr
GEL IX IMAGER 20	INTAS
GloMax Explorer Multimode Microplate Reader	Promega
HERAcell™ 150i CO2 incubator	Thermo Fisher Scientific
HERAfreeze™	Thermo Fisher Scientific
HERASafe™ KS safety cabinet	Thermo Fisher Scientific
Hypercassette™	Amersham Biosciences
Innova® 40 shaker for bacteria	New Brunswick Scientific
Invitrogen Chamber for Ready Gels	Invitrogen
Magnetic thermo stirrer RCT basic	IKA Laboratory Equipment
Mastercycler nexus	Eppendorf
microTOF mass spectrometer	Bruker Daltonics
Mini-PROTEAN Tetra cell SDS electrophoresis system	Bio-Rad Laboratories
Mithras LB 940 Multimode Microplate Reader	Berthold Technologies
Multifuge 3SR+	Thermo Fisher Scientific
NanoPhotometer	Implen
Neubauer chamber	Marienfeld
Novex Mini cell system for precast NuPAGE gels	Thermo Fisher Scientific
Orbitrap Eclipse mass spectrometer	Thermo Fisher Scientific
peqSTAR Thermocycler	Peqlab Biotechnology
Pipetman neo	Gilson
Polymax 1040 platform shaker	Heidolph Instruments
PowerPac Basic power supply	Bio-Rad Laboratories
PowerPac HC power supply	Bio-Rad Laboratories

Precision balance 572-37	Kern & Son
QuantStudio™ 5 Real-Time-PCR machine	Thermo Fisher Scientific
Quintix® Analytical Balance	Sartorius
Scanner V850 Pro	Epson
SevenCompact pH/Ion pH-meter	Mettler-Toledo
SP8 confocal microscope	Leica Microsystems
Thermo block MBT250	Kleinfeld Labortechnik
Thermomixer compact	Eppendorf
Tube rotator	Fröbel Labortechnik
Tumbling roller mixer RM5	Neolab
Vi-Cell Blu Cell Counter	Beckman Coulter

3.1.2 Consumables

3mm CHR paper (Whatman)	GE Healthcare
Amicon® Ultra-15 Centrifugal Filters	Merck Millipore
Cell culture flasks	Greiner Bio-One
Cell culture plates	Biochrom/Falcon/Techno
Cell scraper	Sarstedt
CL-XPosure™ Films	Thermo Fisher Scientific
Glass Cover slips for microscope slides	Sarstedt
Hypodermic needles	Braun
Immobilon-P PVDF transfer membrane	Merck Millipore
Insulin syringes Microfine Plus 29G	BD Biosciences
MicroAmp Fast 96-Well Reaction Plate	Applied Biosystems
MicroAmp Optical Adhesive Film	Applied Biosystems
NuPAGE™ 4-12% BIS-TRIS gel	Thermo Fisher Scientific
Pierce™ Protein Concentrators PES 10K MWCO	Thermo Fisher Scientific
Pipette tips	Sarstedt
SafeSeal tubes	Sarstedt
Serological pipettes	Greiner Bio-One
Syringe filters	TPP/Biochrom
Syringes	Braun
UVette routine pack	Eppendorf
x-well chamber slides on PCA detachable	Sarstedt

3.1.3 Chemicals and Reagents

16% Formaldehyde, methanol free	Thermo Fisher Scientific
2-Propanol	Carl Roth
3XFLAG Peptide	Sigma-Aldrich
4-Methylmorpholine	Sigma-Aldrich
5-Bromo-2′-deoxyuridine (BrdU)	Sigma-Aldrich
ß-Mercaptoethanol	Sigma-Aldrich
ß-Glycerolphosphate disodium salt hydrate (G-2-P)	Sigma-Aldrich
Acetic acid glacial	Carl Roth
Acetone	Carl Roth
AEBSF HCl serine protease inhibitor	Selleckchem

Agarose NEEO	Carl Roth
Albumin Fraction V (BSA)	Carl Roth
Ammonium persulfate (APS)	Sigma-Aldrich
Ampicillin sodium salt	Sigma-Aldrich
Anti-FLAG M2 Affinity Gel	Sigma-Aldrich
Aprotinin from bovine lung	Sigma-Aldrich
Aqua ad injectable, sterile	B. Braun Melsungen
Bacto Agar	BD Diagnostics
Bacto Tryptone	BD Diagnostics
Bacto Yeast Extract	BD Diagnostics
BES buffered saline	Sigma-Aldrich
Bestatin (Ubenimex, NK421)	Selleckchem
Blasticidin S HCl	Thermo Fisher Scientific
Boric acid	Sigma-Aldrich
Bortezomib	Janssen-Cilag
Bromphenol Blue	Sigma-Aldrich
C&L fixer solution type F	Christiansen and Linhardt
C&L developer solution type E	Christiansen and Linhardt
Cathepsin G inhibitor I	Calbiochem
Calcium chloride dihydrate	Sigma-Aldrich
CellTiter 96® Aqueous One Solution	Promega
CHAPS detergent	Merck Millipore
Coomassie Brilliant Blue R-250	Carl Roth
Cycloheximide (CHX)	Sigma-Aldrich
Deoxycholic acid sodium salt	Sigma-Aldrich
Di-sodium hydrogene phosphate dihydrate	Merck Millipore
Dimethylsulfoxid (DMSO)	Carl Roth
Disodium Phosphate	Carl-Roth
DL-Dithiothreitol	Sigma-Aldrich
DNA Loading Dye (6x)	Thermo Fisher Scientific
dNTP Mix, 10 mM each	Thermo Fisher Scientific
Dodecylsulfate-Na-salt (in pellets, SDS)	SERVA
Doxycyline Monohydrat	Sigma-Aldrich
E-64 cysteine protease inhibitor	Selleckchem
Ethanol	Merck Millipore
Ethylenediaminetetraacetic acid (EDTA)	Sigma-Aldrich
FACS Clean	BD Biosciences
FACS Flow	BD Biosciences
FACS Rinse	BD Biosciences
Fc block	BD Biosciences
Formaldehyde, 16% (PFA)	Thermo Fisher Scientific
Fluoride ion solution (NaF)	Sigma-Aldrich
Gelatin from cold water fish skin	Sigma-Aldrich
GelRed Nucleic Acid Gel Stain	Biotium
Gibco™ Trypan Blue Solution, 0.4%	Thermo Fisher Scientific
Glucose	Sigma-Aldrich
Glycine	Carl Roth

Glycerol	Sigma-Aldrich
Hexadimethrine bromide (polybrene)	Sigma-Aldrich
Hexanucleotide Mix, 10x conc.	Roche
Hoechst33258	Sigma-Aldrich
Hydrochloric acid 32%	Carl Roth
Hydrochloric acid fuming 37%	Carl Roth
Leupeptin	Sigma-Aldrich
Lipofectamine 2000 Reagent	Thermo Fischer Scientific
Live/dead Fixable Dead Cell Stain APC-coupled	Thermo Fischer Scientific
Magnesium chloride anhydrous	Sigma-Aldrich
Magnesium sulfate anhydrous	Sigma-Aldrich
Methanol	J. T. Baker
MG132	Biotechne/Tocris Bioscience
N-p-Tosyl-L-phenylalanine chloromethyl ketone (TPCK)	Sigma-Aldrich
N,N,N`,N``-tetramethyl-ethylenediamine (TEMED)	Sigma-Aldrich
Neutrophil elastase inhibitor IV (ONO-5046)	Calbiochem
Nonidet P-40 substitute (10%)	Roche
NuPAGE™ LDS buffer	Thermo Fisher Scientific
NuPAGE™ MES SDS Running buffer (20x)	Thermo Fisher Scientific
Nα-Tosyl-L-lysine chloromethyl ketone hydrochloride (TLCK)	Sigma-Aldrich
PBS Dulbecco, powder	Merck Millipore/Biochrome
Pepstatin A	Selleckchem
Phenylmethanesulfonylfluoride solution (PMSF)	Sigma-Aldrich
PI/RNase staining buffer	BD Pharmingen
Ponceau S solution	Sigma-Aldrich
Potassium chloride	Sigma-Aldrich
PowerUP™ SYBR™ Green Master Mix	Thermo Fisher Scientific
ProLong™ Diamond Antifade Mountant	Thermo Fisher Scientific
Protein G Agarose, Fast Flow	Sigma-Aldrich
Puromycin	Thermo Fisher Scientific
RNaseOUT Recombinant Ribonuclease Inhibitor	Thermo Fisher Scientific
Rotiphorese NF-Acrylamide/Bis-solution 40% (29:1)	Carl Roth
Saponin	Sigma-Aldrich
DNA Stain Clear G	SERVA Electrophoresis
Skim Milk Power	Sigma-Aldrich
Sodium acetate	Merck
Sodium azide	Merck
Sodium carbonate	Merck
Sodium chloride	Carl Roth
Sodium dihydrogen phosphate monohydrate	Merck
Sodium fluoride	Sigma-Aldrich
Sodium hydroxide solution 45%	Carl Roth
Sodium orthovanadate	Sigma-Aldrich
Sodium phosphate dibasic	Sigma-Aldrich
Sodium tetraborate	Sigma-Aldrich
Sodium thiosulfate pentahydrate	Sigma-Aldrich
Strep-Tactin Superflow	IBA Lifesciences

SuperSignal West Femto Max. Sensitivity Substrate	Thermo Fisher Scientific
SuperSignal West Pico Chemiluminescent Substrate	Thermo Fisher Scientific
TRIS-acetat-EDTA (TAE) buffer (50x)	Thermo Fisher Scientific
Trichloroacetic acid solution (TCA)	Sigma-Aldrich
Trifluoroacetic acid solution (TFA)	Sigma-Aldrich
TRIS	Carl Roth
Tris-Buffered Saline (TBS)	Sigma-Aldrich
Triton X-100	Sigma-Aldrich
Trypsin inhibitor from soybean	Sigma-Aldrich
Tween 20	Sigma-Aldrich
Water	Sigma-Aldrich

3.1.4 Commercial Kits

AQueous One Solution Cell Proliferation Assay	Promega
DC Protein Assay	Bio-Rad Laboratories
GeneJET Gel Extraction Kit	Thermo Fisher Scientific
NucleoBond Xtra Midi	MACHEREY-NAGEL
peqGOLD Plasmid Miniprep Kit	Peqlab
Pierce™ Silver staining kit	Thermo Fisher Scientific
QIAquick PCR Purification Kit	Qiagen
QIAshredder	Qiagen
Rapid DNA Dephos & Ligation Kit	Roche
RNeasy Mini Kit	Qiagen

3.1.5 Enzymes

AgeI (BshTI)	Thermo Fisher Scientific
BamHI	Thermo Fisher Scientific
EcoRI	Thermo Fisher Scientific
KspAI (HpaI)	Thermo Fisher Scientific
MluI	Thermo Fisher Scientific
SuperScript III Reverse Transcriptase	Thermo Fisher Scientific
Q5 DNA-polymerase	New England Biolabs

3.1.6 Oligonucleotides

All oligonucleotides were purchased from Eurofins Genomics, Ebersberg, Germany. Nucleotide sequences are written in 5' to 3' direction.

3.1.6.1 Cloning oligonucleotides

FBXL6_AgeI_Kozak_fw	CCCACCGGTGCCACCATGGCTGCCCC
FBXL6-FLAG_MluI_noStop_rv	CCCACGCGTCTTATCGTCGTCATCCTTGTAATCGCTGG
FBXL6-V48_AgeI_Kozak_fw	CCCACCGGTGCCACCATGGTGCTGTCCGAAC
FBXL6-FLAG_MluI_noStop_rv	CCCACGCGTCTTATCGTCGTCATCCT
FBXL6-FLAG_HpaI_Kozak_fw	CCCGTTAACGCCACCATGGATTACAAGGATGACGACG
	ATAAGGCTGCCCCAGCCTCC
FBXL6_BamHI_Stop_rv	CCCGGATCCCTAGCTGGGTGAGGGGC

| FBXL6_HpaI_Kozak _fw | CCCGTTAACGCCACCATGGCTGCCCCAGCCTCC |
| FBXL6-FLAG_BamHI_Stop_rv | CCCGGATCCCTACTTATCGTCGTCATCCTTGTAATCGC TGGGTGAGGGGC |

3.1.6.2 sgRNA sequences

non-targeting gRNA	ACGGAGGCTAAGCGTCGCAA
POLII sgRNA	CAACAAGATCACGCACGAAG
FBXL6 sgRNA_1	GGCTTATGCCCAATCGGTGA
FBXL6 sgRNA_2	TCCCCTTCAGCTGCCTGTCG
FBXL6 sgRNA_3	GCTGAAGGGGAATGCTATTA
FBXL6 sgRNA_5	GAGCGTCAGCAGTCACACCG
FBXL6 sgRNA_6	CAAGAAGCTCACCACAGCTG
FBXL6 sgRNA_8	AGACCGGCTGACTCTAGCCA

3.1.6.3 shRNA sequences

non-targeting shRNA	CCTAAGGTTAAGTCGCCCTCG
FBXL6 shRNA_1	GCACCGGCATCAACCGTAATA
FBXL6 shRNA_2	AGACCGCATTCCCTTGGAAAT
FBXL6 shRNA_3	CACCGGCATCAACCGTAATAG

3.1.6.4 Sequencing primer

pHIV seq_fw	TGGAATTTGCCCTTTTTGAG
pHIV seq_rv	AGGAACTGCTTCCTTCACGA
pTRI2A seq_fw	GTGGGAGGCCTATATAAGCAG
pTRI2A seq_rv	GCGGGCCGCTGTCCTGAG

3.1.6.5 qPCR primer

FBXL6 qPCR_fw	CCGTGTTGAAGCTGGTAGGT
FBXL6 qPCR_rv	AGTGCTGTAGGTCCAGGCTA
CD11b qPCR_fw	GGGCTGGTGGAGTCTTTCTAT
CD11b qPCR_rv	TTCTGCCTGAACATCGCTA
CSF1R qPCR_fw	CCTGAAGGTGGCTGTGAAGATG
CSF1R qPCR_rv	GCTCCCAGAAGGTTGACGATG
RPLP0 qPCR_fw	GCACTGGAAGTCCAACTACTTC
RPLP0 qPCR_rv	TGAGGTCCTCCTTGGTGAACAC

3.1.7 Bacteria

| NEB 5-alpha competent *E. coli* | New England Biolabs |

3.1.8 Standards

| GeneRuler 1 kb DNA Ladder | Thermo Fisher Scientific |
| PageRuler Plus Prestained Protein Ladder | Thermo Fisher Scientific |

3.1.9 Plasmids

pCDH iScaffold-EF1-mTagBFP-P2A-Puro FBXL6 sgRNA_5	R. Ludwig, AHS
pCDH iScaffold-EF1-mTagBFP-P2A-Puro FBXL6 sgRNA_6	R. Ludwig, AHS
pCDH iScaffold-EF1-mTagBFP-P2A-Puro FBXL6 sgRNA_8	R. Ludwig, AHS
pCDH iScaffold-EF1-mTagBFP-P2A-Puro non-targeting control	R. Ludwig, AHS
pcDNA 3.1 C-MYC-FBXL6	D. Koch
pcDNA 3.1 FLAG-FBXL1	F. Bassermann
pcDNA 3.1 FLAG-FBXL16	D. Koch
pcDNA 3.1 FLAG-FBXL3	D. Brockelt
pcDNA 3.1 FLAG-FBXL7	D. Koch
pcDNA 3.1 FLAG-PPM1G	Genscript
pcDNA 3.1 HA-Ubiquitin K48 only	Addgene (#17605), T. Dawson
pcDNA 3.1 HA-Ubiquitin K63 only	Addgene (#17606), T. Dawson
pcDNA 3.1 HA-Ubiquitin wild type (WT)	Addgene (#17608), T. Dawson
pcDNA 3.1 MYC-FBXL1	D. Koch
pcDNA 3.1 MYC-FBXL16	D. Koch
pcDNA 3.1 MYC-FBXL3	D. Koch
pcDNA 3.1 MYC-FBXL5	D. Koch
pcDNA 3.1 N-MYC-FBXL6	D. Koch
pcDNA 3.1 N-Strep-FLAG-FBXL6	D. Brockelt
pcDNA 3.1(+) Zeo Empty vector	Thermo Fisher Scientific
pHIV DsRed C-FLAG-FBXL6	A. Sperk, this study
pHIV DsRed Empty vector	R. Eichner
pHIV DsRed N-FLAG-FBXL6	A. Sperk, this study
pLenti Cas9 Blast	Addgene (#52962), F. Zhang
pLenti CRISPR GFP FBXL6 sgRNA_1	A. Sperk, this study
pLenti CRISPR GFP FBXL6 sgRNA_2	O. Karpiuk
pLenti CRISPR GFP FBXL6 sgRNA_3	O. Karpiuk
pLenti CRISPR GFP FBXL6 sgRNA_5	O. Karpiuk
pLenti CRISPR GFP FBXL6 sgRNA_6	O. Karpiuk
pLenti CRISPR GFP non-targeting control	O. Karpiuk
pLenti CRISPR GFP POLII sgRNA	O. Karpiuk
pLKO.1 DsRed FBXL6 shRNA_1	D. Brockelt
pLKO.1 DsRed FBXL6 shRNA_2	D. Brockelt
pLKO.1 DsRed FBXL6 shRNA_3	D. Brockelt
pLKO.1 DsRed scrambled control	M. Heider
pMD2.G	Addgene (#12259), D. Trono
psPAX2	Addgene (#12260), D. Trono
pTRI2A C-FL-FBXL6	A. Sperk, this study
pTRI2A C-FLAG-FBXL6 Fragment starting at Val48	A. Sperk, this study
pTRI2A Empty vector	R. Spallek

3.1.10 Antibodies

Antibody (clone)	Dilution (application)	Supplier (catalog#)
Caspase-3 (clone 8G10)	1:1,000 (IB)	Cell Signaling (#9665S)
Cathepsin G (clone 12H15L69)	1:1,000 (IB)	Thermo Fisher Scientific (#703590)

CD11b APC-coupled	1:50 (FlCy)	eBiosciences (#17-0112-83)	
Cleaved caspase-3 (Asp175)	1:400 (IB)	Cell Signaling (#9664S)	
CUL1	1:1,000 (IB)	Abcam (#ab85152)	
Donkey anti-mouse IgG-AF488	1:1,000 (IF)	Invitrogen (#A21202)	
Donkey anti-rabbit IgG-AF594	1:1,000 (IF)	Invitrogen (#A21207)	
ECL anti-mouse IgG, HRP-linked	1:15,000 (IB)	GE Healthcare (#NA931)	
ECL anti-rabbit IgG, HRP-linked	1:15,000 (IB)	GE Healthcare (#NA934)	
Erk1/2 (clone C-9)	1:1,000 (IB)	Santa Cruz (#sc-514302)	
FBXL6	1:400 (IB), 1:50 (IF)	Thermo Fisher (#PA564927)	
FLAG	1:1,000 (IB)	Sigma (#F7425)	
FLAG-M2	1:1,000 (IB)	Sigma (#F3165-1MG)	
GAPDH	1:1,000 (IB)	Santa Cruz (#sc-47724)	
HA-tag (clone 16B12)	1:1,000 (IB)	Biolegend (#901501)	
IκB-α	1:1,000 (IB)	Cell Signaling (#4814S)	
IgG2b-APC isotype control	1:50 (FlCy)	BD Biosciences	
MYC-tag	1:1,000 (IB)	Millipore (#06-549)	
p-GSK-3β (Ser9)	1:1,000 (IB)	Cell Signaling (#9322S)	
p27	1:1,000 (IB)	BD Pharmingen (#554069)	
Phospho-Erk1/2 (Thr202/Tyr204)	1:1,000 (IB)	Cell Signaling (#9101S)	
PPM1G	1:1,000 (IB), 1:500 (IF)	Bethyl (#A300-880A)	
SKP1	1:500 (IB)	Santa Cruz (#sc-7163)	
α-Tubulin (clone DM1A)	1:500 (IF)	Sigma (#T9026)	
β-Actin	1:3,000 (IB)	Sigma (#A2228)	

3.1.11 Cell lines

Cell line	Type (human)	Supplier	Medium
MOLM-13	AML	DSMZ (ACC 554)	RPMI + 10% FBS (h.i.)
OCI-AML3	AML	DSMZ (ACC 582)	AlphaMEM + 20%FBS (h.i.)
MV4-11	AML	DSMZ (ACC 102)	IMDM + 10% FBS (h.i.)
THP-1	AML	DSMZ (ACC 16)	RPMI + 10% FBS (h.i.)
HL-60	AML	DSMZ (ACC 3)	RPMI + 10% FBS (h.i.)
Kasumi-1	AML	DSMZ (ACC 220)	RPMI + 10% FBS (h.i.)
NB-4	AML	DSMZ (ACC 207)	RPMI + 10% FBS (h.i.)
PLB-985	AML	kind gift of Prof. P. Jost	RPMI + 10% FBS (h.i.)
NOMO-1	AML	kind gift of Dr. R. Eichner	RPMI + 10% FBS (h.i.)
HEL	AML	kind gift of Dr. R. Eichner	RPMI + 10% FBS (h.i.)
KG1a	AML	kind gift of Dr. R. Eichner	RPMI + 10% FBS (h.i.)
K562	CML	kind gift of Dr. R. Eichner	RPMI + 10% FBS (h.i.)
KCL-22	CML	kind gift of Dr. R. Eichner	RPMI + 10% FBS (h.i.)
LAMA-84	CML	kind gift of Dr. R. Eichner	RPMI + 10% FBS (h.i.)
HEK293T	embryonic kidney	ATCC (CRL-3216)	DMEM + 10% NCS
U937	histiocytic lymphoma	DSMZ (ACC 5)	RPMI + 10% FBS (h.i.)
HeLa	cervical cancer	DSMZ (ACC 57)	DMEM + 10% FBS
U2OS	Osteosarcoma	ATCC (HTB-96)	McCoy's + 10% FBS (h.i.)
H1437	LuAD	ATCC (CRL-5872)	RPMI + 10% FBS (h.i.)

HCC44	LuAD	DSMZ (ACC 534)	RPMI + 10% FBS (h.i.)
MM1.S	MM	ATCC (CRL-2974)	RPMI + 10% FBS (h.i.)
L363	MM	DSMZ (ACC-49)	RPMI + 10% FBS (h.i.)
Amo1	MM	DSMZ (ACC-538)	RPMI + 10% FBS (h.i.)
Riva	DLBCL	DSMZ (ACC 585)	RPMI + 20% FBS (h.i.)
TMD8	DLBCL	kind gift of Prof. D. Krappmann	RPMI + 10% FBS (h.i.)

3.1.12 Animals

NOD scid gamma (NSG) mice (NOD.Cg-Prkdc^{scid} IL2rg^{tm1Wjl}/SzJ)   The Jackson Laboratory

3.1.13 Tissue culture media and supplements

AlphaMEM	Thermo Fisher Scientific
Dulbecco's Modified Eagle's Medium (DMEM)	Thermo Fisher Scientific
Fetal Bovine Serum (FBS) superior	Merck Millipore/Biochrom
Iscove's Modified Dulbecco's Media (IMDM)	Thermo Fisher Scientific
L-Glutamin (100X)	Gibco
GlutaMAX^{TM} (100X)	Gibco
McCoy's 5A Medium Modified	Thermo Fisher Scientific
Newborn Calf Serum (NCS)	Merck Millipore/Biochrom
Opti-MEM I, reduced serum media	Thermo Fisher Scientific
Phosphate buffered saline (PBS), 10X, sterile	Thermo Fisher Scientific
Penicillin/ Streptomycin (100X)	Thermo Fisher Scientific
RPMI 1640 GlutaMAX medium	Thermo Fisher Scientific
rhFLT3L	Peprotech
rhSCF	Peprotech
rhTPO	Peprotech
rhIL3	Peprotech
StemPro-34 Medium	Thermo Fisher Scientific
Trypsin-EDTA (10X) solution	Merck Millipore/Biochrome

3.1.14 Buffers and solutions

Coomassie destaining solution	45% methanol 10% acetic acid
Coomassie staining solution	45% methanol 10% acetic acid 0.25% Coomassie Brilliant Blue R-250
FACS buffer	PBS (1x) 3% FBS
Freezing medium	90% FBS (heat inactivated) 10% DMSO

IF blocking buffer	PBS (1x)
	0.25% gelatin from cold water fish skin
	0.01% Saponin
IF permeabilization buffer	PBS (1x)
	0.1% Triton-X
IF staining buffer	PBS (1x)
	0.5% BSA
	0.01% saponin
Inhibitors in lysis buffers	1 µg/ml aprotinin
	1 mM DTT
	10 mM G-2-P
	1 µg/ml leupeptin
	0.1 mM PMSF
	0.1 mM Na_3VO_4
	10 µg/ml soybean trypsin inhibitor
	5 µg/ml TLCK
	10 µg/ml TPCK
Inhibitor cocktail expansion	0.5 mM AEBSF
	10 µM E-64
	20 µM Bestatin
	20 µM Peptstatin
Laemmli buffer (5x)	300 mM TRIS (pH 6.8)
	10% SDS
	5% β-mercaptoethanol
	0.05% bromphenolblue
	50% glycerol
Luria-Bertani (LB) medium (1x)	1% Bacto Tryptone
	0.5% Bacto Yeast Extract
	170 mM NaCl
LB-agar plates	1.5% Bacto Agar
	LB medium
Lysis buffer (standard)	50 mM TRIS (pH 7.5)
	150 mM NaCl
	0.1% NP40
	5 mM EDTA
	5 mM $MgCl_2$
	5% Glycerol

Lysis buffer (250 mM NaCl)	50 mM TRIS (pH 7.5)
	250 mM NaCl
	0.1% Triton X-100
	1 mM EDTA
	50 mM NaF
Lysis buffer (SDS-containing)	10 mM TRIS (pH 8.5)
	2% SDS
SDS running buffer (10×)	250 mM TRIS (pH 7.5)
	1.92 M glycine
	1% SDS
Separating gel buffer	1.5 M TRIS (pH 8.8)
Stacking gel buffer	0.5 M TRIS (pH 6.8)
Stripping buffer	62.5 mM TRIS (pH 6.8)
	2% SDS
	0.867% β-mercaptoethanol
Transfer buffer (10x)	48 mM TRIS (pH 7.5)
	20% methanol
	39 mM glycine
Washing buffer	PBS (1x)
	0.1% Tween20

3.1.15 Software and Databases

Alphafold	DeepMind and EMBL-EBI
BioVenn	Tim Hulsen
cBioPortal	Memorial Sloan Kettering Cancer Center
Compass™ Data Analysis	Bruker Daltonics
CRAPome	University of Michigan and Samuel Lunenfeld Research Institute Toronto
DAVID	Laboratory of Human Retrovirology and Immunoinformatics
DepMap	Broad Institute
Firebrowse	Broad Institute
FlowJo v10	Tree Star
GeneCards	Weizmann Institute of Science
GPP Web Portal	Broad Institute
IMARIS Viewer	Oxford Instruments
Maximum Entropy software	Bruker Daltonics
MaxQuant	Max Planck institute of biochemistry
MEROPS	EMBL-EBI
Prism 9	Graph Pad Software

Primer-BLAST	NCBI
ProteomicsDB	Technische Universität München and Cellzome GmbH
SnapGene	GSL Biotech LLC
The human protein atlas	The human protein atlas Consortium
UniProt	UniProt Consortium
Vizome	Oregon Health & Science University

3.2   Methods

3.2.1 Molecular biology

3.2.1.1 Molecular cloning

Expression vectors are commonly utilized to alter the expression of specific genes within target cells. These vectors consist of circular dsDNA strands that can be engineered through molecular cloning. In this process, a segment known as the insert, which may contain cDNA for overexpression or a shRNA-stretch for expression reduction, can be either synthetically synthesized or amplified by PCR from template DNA. The insert is then stably integrated into a DNA-vector, termed plasmid. To achieve this, both the insert and plasmid are cleaved using restriction enzymes derived from bacteria. Subsequently, they are combined through an enzymatic reaction called ligation, forming a circular DNA construct, which can be amplified in bacteria.

3.2.1.2 Polymerase chain reaction

Polymerase chain reaction (PCR) designates a molecular biology technique for the rapid *in-vitro* amplification of specific DNA sequences, based on repeated cycles of DNA-denaturation, annealing of specific primers and elongation by a thermo-resistant DNA polymerase (Mullis & Faloona, 1987).

To amplify a specific insert, PCR primers were designed with short overhanging ends encoding for palindromic restriction sites, which were equally present or compatible to restriction sites in the multiple cloning site (MCS) of the target plasmid. For each primer pair the annealing temperature was set 5-10°C below the respective melting temperature. The elongation time was adjusted to the length of the expected PCR product and the elongation rate of the NEB Q5-polymerase (20-30 sec/kb) stated by the manufacturer. The general composition and setup of the PCRs are outlined below. Of note, the addition of the Q5 High GC Enhancer largely increased the PCR efficiency to amplify the GC-rich FBXL6 coding sequence.

Reagent/compound	Amount
DNA-Template	20-100 ng
Forward primer (10 μM)	2.5 μl
Reverse primer (10 μM)	2.5 μl
dNTPs (10 mM)	1 μl
Q5-Reaction Buffer (5x)	10 μl
Q5 High GC Enhancer (5x)	10 μl
Q5-High-Fidelity Polymerase	0.5 μl
Nuclease free dH$_2$O	To 50 μl

Program step	Temperature	Time	Repetitions
Initial Denaturation	98°C	3 min	
Denaturation	98°C	20 sec	30 Cycles
Annealing	X	30 sec	
Elongation	72°C	X	
Final Elongation	72°C	3 min	
Storage	8°C	∞	

PCR fragments were subjected to agarose gel electrophoresis and gel purification (see section 3.2.1.3) to confirm the proper size of the PCR product.

3.2.1.3 Agarose gel electrophoresis and gel purification

Agarose gels are used to separate DNA in an electric field according to its size, thus exploiting the electrostatic properties of DNA molecules due to their negatively charged phosphate backbones. Visualization can be achieved by addition of a fluorescent DNA-intercalating agent. In this study, 1% agarose gels were produced by dissolving agarose in the appropriate volume of TAE buffer by heating. The liquid agarose was cooled down for a couple of minutes and supplemented with DNA Stain Clear G according to the manufacturer's instructions and poured into a gel chamber to solidify. The resulting gel was transferred to a gel running chamber and covered in TAE buffer. DNA samples were mixed with 6x DNA loading dye and run next to a 1kb DNA ladder at 100V for 30-45 min. The DNA was visualized using UV-light and analyzed for size. If desired, DNA fragments were excised and extracted using the GeneJet Gel Extraction Kit according to the manufacturer's protocol.

3.2.1.4 Restriction digest and ligation of DNA

Restriction enzymes recognize and cleave DNA at defined palindromic sequences producing sticky- or blunt-end DNA fragments. Two or more DNA fragments with compatible ends can later be fused by an enzymatic reaction called ligation.

All digests conducted in this study resulted in single-stranded DNA overhangs (sticky ends) facilitating specific annealing of two particular fragments and ligation. For cloning distinct DNA constructs, 0.5-3 µg DNA (plasmids and/or inserts) were digested using 0.5-1 µl of restriction enzyme in the respective buffer for up to 1 h at 37°C. For simultaneous digestion with multiple enzymes, buffer conditions were chosen as recommended by the manufacturer. After the digest, plasmids were analyzed by gel electrophoreses and gel purified (see section 3.2.1.3), whereas smaller PCR products or inserts were separated from the digestion mixture by GeneJet Gel Extraction Kit according to the manufacturer's protocol. Subsequently, the Rapid DNA Dephos & Ligation Kit was used to ligate insert and plasmid DNA in a molar ratio of 4:1, using 40 ng of digested plasmid DNA, according to the manufacturer's protocol.

3.2.1.5 Annealing and ligation of short hairpin RNA-oligonucleotides

Oligonucleotides for cloning short hairpin RNA (shRNA) expression constructs were designed using the GPP-Web Portal (Broad Institute) and ordered from Eurofins Genomics (Ebersberg, Germany). Diluted and mixed oligos were annealed and subsequently ligated into the pLKO.1 TRC cloning vector. The annealing mixture was composed of 1 µL of forward and reverse oligonucleotide each (100 µM) and Buffer G in a total volume of 50 µL. This mixture was incubated in a beaker of boiling water and set to cool down overnight. 2 µl of the annealed

oligos were ligated with 50 ng of the pLKO.1 TRC cloning vector cut with AgeI and EcoRI and transformed into chemically competent NEB 5-alpha *E. coli* (see section 3.2.1.6).

3.2.1.6 Transformation of plasmids into bacteria

After ligation, the resulting DNA constructs were transformed into bacteria for amplification and/or insert screening. For this purpose, 1.5-2 µl ligation or 100 ng DNA were added to 15-20 µl of chemically competent NEB 5-alpha *E. coli* and incubated on ice for 20 min, followed by a 45 sec heat shock at 42°C and a 2 min incubation on ice. To select for plasmid-carrying bacterial colonies versus non-transformed clones, bacteria were plated on LB agar plates containing antibiotics, matching the plasmid-encoded antibiotic resistance, usually ampicillin. Agar plates were then incubated at 37°C overnight. Single colonies were picked and inoculated in LB medium containing the respective antibiotic and incubated at 37°C and 250 rpm shaking overnight.

3.2.1.7 Plasmid DNA extraction from bacteria

Amplified plasmid DNA from bacteria was purified using commercially available plasmid purification kits. Depending on the amount of bacterial culture, either the peqGOLD Plasmid Miniprep Kit or the QIAGEN Plasmid Maxi Kit was used according to the manufacturer's instructions. This method uses alkaloid lysis to break down the bacterial cell wall and subsequent immobilization of DNA on an anionic column. Contaminants such as RNA and protein are removed by raising salt concentrations. Finally, DNA is eluted with high salt buffer and precipitated using isopropanol. Pelleted DNA is cleared from salt with 70% ethanol and resuspended in a suitable storage buffer. After cloning, test digests using suitable restrictions enzymes were performed, and positive clones were sent for sequencing. For long-term storage of positive clones, an aliquot of the bacterial culture was mixed 1:1 with glycerol and frozen at -80°C. In case the sequence identity of a plasmid was not clear, for example after molecular cloning, the resulting plasmids were analyzed by test digest and/or sequencing at Eurofins Genomics (Ebersberg, Germany), using promoter- or gene-specific primers.

3.2.1.8 RNA extraction from eukaryotic cells

For the analysis of gene expression on the transcriptional level, mRNA needs to be extracted from cells. Due to the low stability of RNA and the omnipresence of RNA-degrading enzymes, called RNases, the extraction has to be performed on ice and by using RNase-free solutions. In this study, total RNA from AML and other cell lines was extracted using the RNeasy Mini Kit (Qiagen), which exploits the reversible binding of RNA to silica-membrane spin columns, according to the manufacturer's instructions. RNA concentration in the final eluates was determined spectrophotometrically. For maintaining stability, RNA was stored in RNase-free water at -80°C.

3.2.1.9 Reverse transcription

Reverse transcriptases are enzymes of viral origin, synthesizing complementary DNA (cDNA) based on an RNA template in a process called reverse transcription. The resulting cDNA is the basis of different gene expression analyses such as quantitative PCR. To obtain cDNA, 1 µg of extracted RNA (see section 3.2.1.8) was reversed transcribed using oligo-dT primers, which allow specific transcription of mRNA via annealing to polyA-tails, dNTPs and

the SuperScript III Reverse Transcriptase according to the manufacturer's protocol: after primer annealing at 42°C for 5 min, cDNA was synthesized at 72°C for 60 min.

3.2.1.10   Quantitative PCR

Quantitative PCR (qPCR), or real-time qPCR, is a PCR-based method that employs fluorochromes to monitor the amount of amplified DNA in real time after each PCR cycle. SYBR Green, a commonly used qPCR dye, binds to double-stranded DNA non-specifically, forming a DNA-SYBR Green complex that absorbs blue light and emits green light. The intensity of fluorescence is directly proportional to the amount of DNA present, enabling the quantification of gene expression relative to reference genes.

In this study, qPCR was performed on a QuantStudio™ 5 Real-Time-PCR instrument using the PowerUP™ SYBR™ Green Master Mix (both Thermo Fisher), according to the manufacturer's instructions, with reverse transcribed cDNA from AML/other cell lines (see section 3.2.1.9) as a template. Specific qPCR primers were designed with the primer-BLAST platform (NCBI) to amplify short sequences (around 100 bp) of FBXL6, CD11b, and CSF1R. For normalization, the expression of the housekeeping gene RPLP0 was determined.

3.2.2   Cell culture and cell-based assays

3.2.2.1 Culture of eukaryotic cells

Mammalian cell cultures were grown in a humidified incubator (HERAcell™ 150i CO2 incubator, Thermo Fisher Scientific) at 37°C with 5% CO2 and handled in biological safety cabinets (HERAsafe™, Thermo Fisher Scientific). All cell lines were grown in media containing 1% penicillin/streptomycin and GlutaMax supplement (containing L-alanyl-L-glutamine, a stabilized form of L-glutamine), if not indicated otherwise. The respective media composition for each cell line can be found in the material section, where the cell lines used are listed. Heat inactivation (h.i.) of serum (FBS) was achieved by incubation for 60 min at 65°C. Adherent cells were kept on dishes and sub-cultured at 70-80% confluency. After a PBS wash, cells were detached by incubation with trypsin at 37°C for 3-10 min. Trypsin was quenched by the addition of culture medium, the resulting single-cell suspension was pelleted by centrifugation at 1200 rpm for 4 min and a proportion of cells were transferred to a new plate in fresh medium. Suspension cells were grown in appropriately sized cell culture flasks at maximum densities between 1-10 x10^5 cells/ml and split every 2-3 days at a ratio of 1:4-1:10. To determine the number of cells in culture, an aliquot of the cell solution was mixed in a 1:1 ratio with trypan blue, a dye only penetrating and thus coloring dead cells, and viable cells were counted in a Neubauer chamber.

3.2.2.2 Freezing and thawing of cells

Cryopreservation of mammalian cells was achieved by resuspending 1-10x10^6 exponentially growing cells in 1 ml of FBS supplemented with 10% DMSO, an agent which prevents crystallization and thus cell damage at low temperatures. To reduce the cell damage further, cells aliquoted in cryotubes were transferred to a -80°C freezer inside of an isopropanol-containing freezing device, assuring a cooling rate of 1°C per min. After at least 24 hrs at -80°C, frozen cells were transferred to liquid nitrogen for long-term storage.

While unfreezing, it is important to rapidly wash out DMSO, which can be toxic at prolonged exposures. Therefore, cells were rapidly thawed at 37°C, diluted in the respective growth medium, centrifuged, and plated in fresh growth medium.

3.2.2.3 Harvesting of cells

For subsequent protein or RNA extraction, supernatants of adherent cultured cells were removed, and cells were detached from culture plates by scraping in PBS. The obtained suspensions or collected non-adherent cells were pelleted by centrifugation at 1200 rpm for 4 min and washed once in PBS. Cell pellets were either used immediately for cell lysis (e.g. for *in-vivo*-ubiquitylation assays or denaturing lysis with SDS-containing buffers) or frozen at -80°C.

3.2.2.4 MTS cell viability assay

To estimate the number of viable, metabolically active cells in a given population, the MTS cell viability assay utilizes a colorimetric tetrazolium reagent ((3-(4,5-dimethylthiazol-2-yl)-5-(3-carboxymethoxyphenyl)-2-(4-sulfophenyl)-2H-tetrazolium), MTS). The tetrazolium compound is metabolized by viable cells into a colored formazan product. For measuring the resulting absorbance at 490 nm, a multi-well plate reader is commonly used. Since dead cells lack the ability to metabolize tetrazolium reagents, the resulting absorbance is considered to be proportional to the number of viable cells.

In this study, AML cells were subjected to MTS assay by plating 100 µl of homogenous cell suspension into flat-bottom 96-well plates and adding 20 µl of CellTiter 96® Aqueous One Solution (Promega) using a multi-channel pipet without producing air bubbles. Cell culture medium plus MTS solution served as a control for background signal. Cells were incubated for 1-2 hrs at 37°C before measuring the absorbance at 490 nm on a GloMax Explorer Multimode Microplate Reader (Promega). Absorbance values were reduced by the background signal determined from medium controls and depicted in relation to an internal control such as non-targeting sgRNA in knockout experiments.

3.2.2.5 Transient transfection of cells with DNA

Transient transfection of HEK293T cells with plasmid DNA was carried out using the calcium phosphate method described previously (Kingston et al., 1999). In brief, for a 10 cm cell culture dish at 50-70% confluency, 10 µg of DNA were dissolved in 450 µl sterile dH$_2$O and 50 µl of 2.5 M CaCl$_2$ was added. After mixing thoroughly and incubation at room temperature (RT) for 5 min, 500 µl BES buffer was added dropwise while constantly vortexing. After additional 20 min at RT, the DNA calcium phosphate solution was carefully dripped onto the cells. Cells were incubated with the formed DNA-Calcium complexes for 4-24 hrs and subsequently analyzed or processed further.

To achieve equal amounts of more than two different plasmids transfected simultaneously (e.g. for *in-vivo*-ubiquitylation assays), Lipofectamine 2000 was used a transfection reagent according to the manufacturer`s protocol. In brief, equal amounts of serum-free Opti-MEM were mixed with DNA and Lipofectamine 2000 reagent in separate reactions and incubated for 5 min at RT. The DNA-containing solution was then added to the Lipofectamine 2000 dilution and mixed by inverting the tube. After 20 min incubation at RT, the transfection mix was added to cells in P/S-free medium. The medium was renewed after

3-4 h. For maximizing the transfection efficiency while retaining low cytotoxicity, a DNA to Lipofectamine ratio of 1:3 was chosen. Cells were transfected at 50-70% confluency.

3.2.2.6 Production of lentiviral particles and viral transduction of cells

Lentiviral transduction of cells is a method that allows the stable expression of a desired DNA sequence by permanently integrating it into a cell's genome. Lentiviral particles were produced by transient transfection of HEK293T cells in a 10 cm dish using the calcium phosphate method, or alternatively, with Lipofectamine 2000 (if especially high viral titers were necessary) (see section 3.2.2.5) to deliver 15 µg packaging plasmid (psPAX2), 5 µg envelope plasmid (pMD2.G) and 20 µg of the plasmid of interest (e.g. an shRNA construct or a pHIV-based overexpression construct). 24 hrs after transfection, the medium was replaced with 6-10 ml Opti-MEM, which was harvested as viral supernatant after another 24 hrs. To clear the supernatant from cell debris, it was passed through a 0.45 µm filter and used either directly or stored at -80°C.

For lentiviral infection of non-adherent cells such as AML cell lines, $0.5-1x10^6$ cells were plated in 0.5 ml of growth medium per well of a 6-well plate. Next, 2 ml of viral supernatant and polybrene (at a final concentration of 8 µg/ml) were added. Polybrene is a cationic polymer facilitating the interaction of virions and the eukaryotic cell surface (Davis et al., 2002). For increased efficiency, the cells were subjected to spin-infection at 700xg for 30 min at 30°C and subsequently incubated with the viral supernatant for 24 hrs before exchanging the growth medium. Transduction efficiency was evaluated three days after infection using flow cytometry.

3.2.2.7 Doxycycline treatment for transgene expression

To induce the expression of a transgene at a specific time point after viral transduction, a doxycycline-inducible system can be applied. In this study, FBXL6 was expressed under the control of a doxycycline-inducible promotor in the pTRI2A backbone after stable integration into the genome of AML cell lines. After selection for transduced cells using puromycin, the transgene expression was induced by the addition of doxycycline at a final concentration of 1 µg/ml into the growth medium. For prolonged transgene expression, doxycycline was renewed every 48 h.

3.2.2.8 Protein stability assay with cycloheximide

Analysis of protein stability and turnover can be achieved by inhibiting the translation machinery of the cell for different periods of time with subsequent analysis of the protein abundance, for instance by immunoblot analysis (Dietachmayr et al., 2020; Fung et al., 2018). Cycloheximide (CHX) is a naturally occurring compound that inhibits eukaryotic ribosomes and thereby stalls *de novo* protein translation. In this study, CHX was dissolved in 100% ethanol to create a fresh stock solution of 100 mg/ml before each experiment. Cells were treated with 200 µg/ml for different time points of up to 8 h. To investigate whether the destabilization was proteasome-dependent or not, the proteasome inhibitor MG132 was added together with CHX for the indicated time points at a concentration of 10 µM.

3.2.3 Flow cytometry

Flow cytometry is a laser-based technique for the characterization of cells at single-cell resolution, which is broadly used for analysis and cell sorting. In a stream of fluid, single cells pass lasers and detectors that measure the physical properties such as size and granularity next to fluorescent signals from e.g. fluorochrome-coupled antibodies or expressed fluorochromes.

Data presented in this study were either obtained at a FACS Calibur or a FACS Accuri C6 plus (both BD Biosciences) and analyzed using the software FlowJo v10. To determine the transduction efficiency of AML cell lines infected with a viral vector containing GFP as a fluorescent marker, cells from the growing culture were collected at the indicated time points. These were then washed with 2 ml PBS, resuspended in PBS, and analyzed using one of the mentioned flow cytometers.

3.2.3.1 Fluorescence activated cell sorting

FACS (fluorescence activated cell sorting) describes the sorting of cells based on their flow cytometric properties and fluorescent markers. In this study, FACS was used in case of insufficient transduction rates to purify infected cells, that expressed GFP or DsRed-Express2 as a selection marker to obtain a homogenous cell population. FACS was performed on a FACS Aria Fusion cell sorter in the Core Facility Cell Analysis at TranslaTUM, Klinikum rechts der Isar. For sorting, the cells were washed, resuspended in FACS buffer at a concentration of $1-10\times10^6$ cells/ml, filtered to obtain a single-cell solution, and stored on ice until sorting. Sorted cells were recovered in FBS h.i. and cultured in the usual growth medium.

3.2.3.2 Live/dead staining

To determine the relative number of dead cells within a given population, live/dead staining was performed, utilizing an amine-binding dye that discriminates between viable cells and dead cells by signal intensity. The dye binds to amines on the cell surface of both viable and dead cells. Perforation of the membranes of dead cells additionally facilitates the binding of the dye to intracellular amines, resulting in an increase in signal intensity compared to living cells measured by flow cytometry.

For complementarity with GFP-expressing AML cells in knockout experiments, an APC-coupled live/dead stain (Thermo Fisher Scientific) was used in this study. The lyophilized dye was dissolved in DMSO for generating a stock solution according to the manufacturer's instructions. For the staining, cells were washed once with PBS and subsequently incubated with the live/dead stain at a 1:2,000 dilution in PBS for 15 min at RT on an overhead rotator to assure even staining. After washing with PBS, cells were resuspended in an appropriate volume of PBS for flow cytometric analysis.

3.2.3.3 Cell cycle analysis

To analyze the cell cycle stage of a cell, one commonly used method is to monitor its DNA content. For this purpose, a DNA-intercalating fluorescent dye called propidium iodide (PI) is utilized. This dye allows for discriminating between cells in the G0/G1 phase and those in the G2/M phase. Cells in the G2/M phase have a DNA content of 4N, which is twice the amount found in G0/G1 phase cells (2N). Consequently, G2/M phase cells exhibit significantly

higher fluorescence when labeled with PI and measured by flow cytometry, typically at around 617 nm emission. During the S- or Synthesis phase of the cell cycle, cells undergo DNA duplication in preparation for division. As a result, they possess an intermediate amount of DNA and PI signal.

In this study, PI/RNase staining buffer (BD Pharmingen) was used for PI staining, following the manufacturer's protocol. After fixation of the cells in 70% ice-cold ethanol, the derivate was stained with PI/RNase staining buffer for 15 min at RT and analyzed by flow cytometry. The relative amount of cells in the respective cell cycle phase was determined in the FlowJo software using the Watson (Pragmatic) model.

3.2.3.4 CD11b surface staining

The integrin CD11b is specifically expressed on the cell surface of cells at late stages during myeloid differentiation, such as granulocytes, monocytes, and macrophages (Kansas et al., 1990). Surface staining of CD11b with subsequent flow cytometric analysis is commonly used to assess the differentiation status within the myeloid lineage of AML cells (Bestilny & Riabowol, 2000; Jing et al., 2018).

To this end, AML cells were washed once with PBS before blocking Fc receptors by incubating with Fc block (BD Biosciences) at a 1:20 dilution in PBS for 10 min at RT. Fc receptors are expressed on various immune cells including myeloid cells and might bind non-specifically to detection antibodies used in the staining process, thus causing a false positive signal. After removing the Fc block, cells were stained with fluorochrome-coupled anti-CD11b antibody or isotype control in a 1:50 dilution in PBS for 30 min at 4°C on an overhead rotator to assure even staining. The staining solution was washed off with PBS and cells were resuspended in PBS for flow cytometric analysis.

3.2.4 Immunofluorescence of non-adherent cells

Immunofluorescence (IF) is a method to visualize proteins and their subcellular localization using fluorescent markers such as fluorochrome-coupled antibodies and a fluorescence microscope for detection. Immunofluorescence microscopy of non-adherent cells, especially AML cells, harbors a few challenges since attachment of the cells to a microscopic slide without the induction of myeloid differentiation needs to be achieved for the staining of intracellular proteins. In this study, a protocol was established which utilizes the attachment of AML cells under serum-free conditions to plastic multi-well chamber slides without prior coating. An analogous procedure has been described for lymphocytes (Tsang et al., 2017).

To prepare AML cell lines for the IF staining, cells were counted in a Neubauer chamber. Subsequently, 120,000 cells were washed once with PBS and resuspended in 500 µl PBS to be transferred to one well of a detachable, 8-well chamber slide for microscopy (plastic, Sarstedt). The slide was briefly centrifuged (max. 1500 rpm) to accelerate the sedimentation to the well bottom. Cells were allowed to attach to the surface for exactly 5 min at RT. Importantly, a longer incubation time was observed to induce a certain degree of myeloid differentiation, as the cells changed their morphology from blast-like, round cells to a more spread-out form resembling macrophages. Following attachment, the PBS was removed and replaced by 4% PFA in PBS for fixation of the cells for 10 min at RT. Cells were

washed once with PBS and then permeabilized using IF permeabilization buffer for 10 min. After another PBS washing step, unspecific antibody binding sites were blocked with IF blocking buffer for 30 min. To stain the proteins of interest, primary antibodies were incubated over night without agitation at 4°C. Fluorochrome-coupled secondary antibodies were incubated for 1 h at RT. Nuclei were stained with Hoechst33258 for 15 min at RT. Between each staining step, cells were washed three times with PBS. After the staining, the chamber was removed from the slide and washed once with water. Finally, mounting medium was dripped on the slide, covered with a glass coverslip, and let cure for 24 hrs before imaging on a confocal microscope.

3.2.5 Protein Biochemistry

3.2.5.1 Standard cell lysis

To analyze the protein content of a cell population or to perform protein-protein interaction studies, cells need to be lysed by disruption of their membranes and organelles while keeping proteins in solution and preventing their degradation.

For standard cell lysis, harvested cell pellets were resuspended in suitable buffers containing high amounts of salts and/or detergents. To prevent the degradation of proteins or changes in post-translational modifications, specific protease and phosphatase inhibitors were added. If not specified otherwise, ice-cold 150 mM NaCl lysis buffer (standard for cell lysis) supplemented with DTT, protease (PMSF, TLCK, TPCK, PIN) and phosphatase inhibitors (Nava, Glycerol-2-Phospate) was used. Additionally, benzonase was added to lysis buffers at a 1:3,000 dilution to assure complete lysis of chromatin and thus solubilization of nuclear proteins such as FBXL6. Cell pellets were resuspended in lysis buffer and incubated for 20 min on ice. After 10 min of incubation, lysates were pressed four times through an Insulin syringe to increase the efficiency of breaking up all organelles and chromatin. Lysates were cleared of DNA and membrane debris by centrifugation at 14,000 rpm at 4°C for 15 min. Subsequently, protein concentrations of the cleared supernatants were measured by a modified Lowry assay (Lowry et al. 1951) using the Bio-Rad DC protein assay according to the manufacturer's instructions. Protein-containing supernatants were either denatured by the addition of Laemmli buffer and heating to 95°C for 5 min or used in immunoprecipitations or *in-vitro*-cleavage assays.

3.2.5.2 Denaturing cell lysis

To obtain an immediate snapshot of cellular proteins, thus excluding any artificial processes caused by cellular enzymes such as excessive protease cleavage happening during standard cell lysis, cell pellets were lysed under denaturing conditions.

For denaturing lysis, fresh cell pellets were resuspended in 2% SDS-containing lysis buffer without prior freezing. Using a cut pipet tip allowed for easier handling of the sticky lysates, which were subsequently boiled for 5 min at 95°C and before placing on ice for 5 min. To reduce the viscosity of the lysate, samples were subjected to one freeze-thaw cycle (-80°C, followed by boiling for 5 min 95°C) and acidified with 10% TFA (Trifluoroacetic acid, final concentration 1-2% depending on viscosity). Samples were immediately vortexed after TFA addition and subsequently quenched with 20% NMM (4-Methylmorpholine, final concentration 2-4%, proportional to TFA concentration: e.g. 1% TFA and 2% NMM) and

mixed by vortexing. Samples were put on ice and tested for a pH of 7.5 – 8.5. If necessary, the pH was adjusted using NaOH or NH_4OH. Finally, lysates were cleared by centrifugation at 21,000xg, 4°C for 5 min and the supernatant was transferred to a fresh tube.

3.2.5.3 SDS polyacrylamide gel electrophoresis

SDS polyacrylamide gel electrophoresis (SDS-PAGE) is a method that allows for the separation of proteins in a complex mixture based on their protein mass. By the addition of SDS, denatured proteins are coated in negatively charged detergent molecules, which allows them to move through a polyacrylamide gel at a mass-specific speed that is independent of their inherent charge, as soon as an electric field is applied. SDS-acrylamide gels were cast using Mini-PROTEAN Tetra Electrophoresis System. A standard gel consisted of a short upper part, the so-called stacking gel containing 3.9% acrylamide, and a lower separating gel containing 6-14% acrylamide, depending on the size of the proteins of interest.

Reagent per gel in ml	Separating Gel (10 ml)				Stacking Gel (5 ml)
	5%	8%	10%	12%	
Acrylamide 40% (29:1)	1.25	2.0	2.5	3.0	1.25
H_2O	to 10 ml				to 5 ml
Separating Buffer	2.5				-
Stacking Buffer	-				1.25
SDS (10%)	0.1				0.05
APS (10%)	0.1				0.05
TEMED	0.004				0.005

After polymerization, 10-25 μg of denatured protein sample were loaded into the pockets of a gel assembled in a running buffer-filled chamber next to a protein ladder and resolved at 80-120 V. After electrophoresis, gels were incubated in Coomassie or silver stain (section 3.2.5.4) to visualize proteins within the gel or transferred to a membrane for immunoblot analysis (section 3.2.5.5).

3.2.5.4 Coomassie- and silver-staining

Proteins can be visualized directly within an acrylamide gel using Coomassie- or silver-staining. Both methods stain proteins based on charges present in the amino acid chains. Coomassie-staining is less sensitive compared to silver-staining, as Coomassie interacts with the positive amine groups through van der Waals interactions and visualizes ≥50 ng protein, while the reduction of silver ions to elementary silver by negatively charged residues detects a minimum of 1 ng of protein.

For a Coomassie staining, gels were incubated in Coomassie staining solution for at least 1 h or overnight while shaking. Excess dye was removed by repeated washes with Coomassie destaining solution. Silver stains were carried out using the Thermo Scientific Pierce Silver Stain Kit according to the manufacturer's instructions.

3.2.5.5 Immunoblot analysis

Immunoblot analysis (Western blot) is a method used to detect proteins bound to a membrane using specific antibodies.

Proteins separated by SDS-PAGE were transferred to polyvinylidene difluoride (PVDF) membranes, which bind proteins via hydrophobic and polar interactions. PVDF membranes were activated in methanol for 1 min before the transfer of proteins from the SDS-gel to the membrane by electroblotting at either 100 V for 80 min or at 30 V overnight. For quality control, membranes were colored with Ponceau solution that reversibly stains all proteins bound to a membrane. After destaining in washing buffer (WB) and blocking in 5% milk in WB for 30 min, the membranes were incubated with primary antibodies diluted in 5% milk or 5% BSA in WB on a roller mixer at 4°C overnight. If not further specified, β-Actin served as an internal loading control. After washing (three times 10 min) in WB, membranes were incubated with the respective HRP (horse raddish peroxidase)-coupled secondary antibody at a dilution of 1:15,000 in 5% milk for 45 min at RT. After washing again (three times 10 min), blots were incubated with enhanced chemiluminescent (ECL) solution (Pierce™ ECL Western Blotting Substrate, Thermo Fisher Scientific) and exposed to photosensitive films (Amersham Hyperfilm™ ECL). An automatic film developer machine (Curix 60, Agfa) was used to visualize protein bands.

3.2.5.6 Stripping of membranes

To re-probe a PVDF membrane with another antibody, the previously bound primary and secondary antibodies can be removed via incubation with a denaturing buffer containing SDS and β-mercaptoethanol in a process called stripping. To this end, membranes were incubated with stripping buffer for 45 min at RT, followed by four washes with PBS for 15 min each. Subsequently, membranes were blocked in 5% milk in WB and incubated with a new primary antibody.

3.2.5.7 *In-vivo*-ubiquitylation assay

An established method to analyze the ubiquitylation status of a protein in a specific cellular context is the so-called *in-vivo*-ubiquitylation assay. For this purpose, cells plated on 6 cm dishes were transfected with plasmids encoding 0.3-1 µg HA-tagged ubiquitin or one of its variants, 1-3 µg FLAG-tagged substrate-candidate and 1-2.5 µg E3-ligase of interest or respective controls using Lipofectamine 2000 (section 3.2.2.5). 24 hrs after transfection cells were treated with 10 µM MG132 for 3 hrs to enrich for proteins which might otherwise be degraded by the proteasome. Harvested cells were lysed freshly, without prior freezing, in 110 µl ice-cold 250 mM NaCl lysis buffer supplemented with protease and phosphatase inhibitors. After 15 min of incubation on ice, lysates were cleared by centrifugation, and supernatants were denatured by the addition of 1% SDS, 5 mM EDTA and heating to 95°C for 5 min. Samples were allowed to reach room temperature and diluted with 900 µl 250 mM NaCl lysis buffer supplemented with 1% Triton X-100 and incubated on ice for 15 min. Finally, a FLAG-IP was performed as described in section 3.2.5.8.

3.2.5.8 Immunoprecipitation

Immunoprecipitation (IP) is a technique used to purify proteins form cell lysates using specific antibodies raised against a protein or protein-tag of interest. These antibodies are commonly coupled to agarose beads by a covalent bond and allow for sedimentation of bound proteins by centrifugation. In this study, IPs were performed from whole-cell extracts (WCE) using standard lysis buffers (see section 3.2.5.1).

For IPs of Flag-tagged proteins, lysates were incubated with FLAG-M2 agarose beads. Before use, the beads were washed three times in lysis buffer and diluted 1:1 with the buffer to produce a slurry suspension. Per 4×10^7 cells used for lysis, 32 µl of slurry beads (or a minimum of 20 µl slurry beads per reaction if smaller amounts of cells were lysed) were added and incubated for 1-1.5 hrs at 4°C on a rotating wheel. Beads were then sedimented at low centrifugation speed and washed three times with lysis buffer to reduce unspecific binding. If unspecific binding was causing problems in further analyses, a pre-clear was done using plain agarose beads. These 'empty beads' were added to every lysate before the actual IP-beads for 30min at 4°C, removed from the lysates and discarded. If not further specified, beads were eluted by addition of 60 µl of 2x Laemmli buffer and cooked at 95°C for 10 min. Samples of WCE and IPs were analyzed by SDS-PAGE and immunoblot (see section 3.2.5.5).

3.2.6 Mass spectrometry

Mass spectrometry (MS) is a technique to measure the mass and charge of substances and has emerged as a powerful tool to analyze single proteins or entire proteomes. Two MS-based proteomics approaches can be distinguished according to the desired gain of information: bottom-up and top-down proteomics. In a bottom-up proteomics approach, complex protein mixtures are analyzed by measuring peptides resulting from enzymatic digestion (e.g. by trypsin) that are ionized and separated according to their mass-to-charge ratio in an electric or magnetic field. Based on the detected spectra, peptides are identified by correlation to the mass-to-charge ratio of known peptides (generated by the respective enzyme), enabling the identification and quantification of the protein of origin (Yates et al., 2009). In a top-down proteomics experiment, intact proteins are ionized to determine the total mass of a protein and its post-translational modifications (Catherman et al., 2014). For this, less complex protein samples such as immunoprecipitations of a protein of interest are needed.

3.2.6.1 Bottom-up proteomics

In this study, bottom-up proteomics was performed for the identification of FBXL6 interaction partners and to determine the cleavage site in the FBXL6 sequence. In both cases, FLAG-tagged FBXL6 was purified from AML cell lines according to the general protocol in section 3.2.5.8 with minor adjustments. Instead of a denaturing elution from the FLAG beads, bound proteins were eluted using 3XFLAG peptide at a concentration of 1 mg/ml in TBS (elution volume was 2.5x the bead slurry volume; 30 min at 4°C on an overhead rotator) for retaining anti-FLAG antibodies on the beads. The single elution step was followed by a TBS wash to increase the yield of the elution without further increasing the amount of FLAG peptide in the eluate.

For the cleavage site identification, eluates separated on an SDS-gel were stained with Coomassie, and bands corresponding to FBXL6 were cut out and sent to Dr. Barbara Steigenberger at the proteomics core facility of the Max Planck Institute (MPI) of Biochemistry in Martinsried, Germany for further processing and MS analysis.

For the interactome analysis, eluates were precipitated with 20% TCA, washed with Acetone, and dried in a vacuum concentrator. After reconstitution in LDS buffer (NuPAGE™), reduced with DTT and alkylated with chloroacetamide (CAA). Half of the sample was run on

a 4-12% BIS-TRIS NuPAGE gel and stained with Coomassie before handing over to Dr. Piero Giansanti of the BayBioMS@MRI core facility at TUM.

Further processing by the collaboration partners started with in-gel trypsin digestion of the proteins. Tryptic peptides were extracted, dried, and reconstituted in buffer containing 0.1% formic acid (FA) and analyzed by LC-MS/MS (liquid chromatography tandem mass spectrometry) either on a Dionex Ultimate 3000 RSLCnano system (Thermo Fisher Scientific) coupled to an Orbitrap Eclipse mass spectrometer (Thermo Fisher Scientific) for the interactome analysis, or on a 30-cm column (inner diameter: 75 microns; packed in-house at MPI with ReproSil-Pur C18-AQ 1.9-micron beads, Dr. Maisch GmbH) coupled to an Exploris 480 mass spectrometer (Thermo Fisher Scientific) for the cleavage site identification. Peptide and protein identification and quantification were performed using MaxQuant by searching the MS2 spectra against the human reference proteome supplemented with common contaminants.

3.2.6.2 Top-down proteomics

Top-down proteomics was performed to determine the protein mass of the lower-running form of FBXL6. For direct injection of the intact protein into the mass spectrometer, the detergent NP-40 had to be substituted in the lysis buffer by the more MS-friendly detergent CHAPS. To this end, AML cell lines were lysed with the 150 mM lysis buffer without NP-40 but with 0.5% CHAPS, and FLAG-FBXL6 was purified and eluted from the beads using 3XFLAG peptide as described in section 3.2.6.1. Eluates were concentrated 25X using Pierce™ Protein Concentrators with a molecular weight cut-off of 10 kDa, which allowed for excluding most of the 3XFLAG peptide used for the elution of the purified proteins. For quality control, equivalent amounts of the initial eluate, the concentrator flow through and the final eluate were separated by SDS-PAGE and subjected to silver staining. Concentrated eluates were denatured using 1% TFA and sent to Martinsried for analysis by Victoria Sanchez at MPI.

Subsequent work by Victoria Sanchez included LC-MS (liquid chromatography mass spectrometry) measurement of the samples on an Agilent 1100 HPLC column (Phenomenex Aeris™ 3.6 µm WIDEPORE C4 100 mm x 2.1 mm ID, 200 Å pore size) coupled to a microTOF mass spectrometer (Bruker Daltonics, mode: positive, mass range 800-3000 m/z). To elute the sample from the column, LC Buffer A (0.05% TFA in H_2O pH 2.0) and LC Buffer B (0.05% TFA in ACN pH 2.0) were used at a flow rate of 250 µl/min and increasing percentage of LC Buffer B. The resulting mass spectrometric data was processed using the Compass™ Data Analysis software and deconvoluted with the Maximum Entropy software (both Bruker Daltonics) applying 10,000 instrument resolving power.

3.2.7 Patient-derived xenograft mouse model

Mouse models are central preclinical models in cancer research, enabling the investigation of tumors *in vivo*. Xenografts in immunodeficient mice allow for performing functional studies on patient-derived cancer cells. All *in-vivo* experiments were carried out by Romina Ludwig and Jan Philipp Schmid from the research unit Apoptosis in Hematopoietic Stem Cells (AHS) at the Helmholtz Center in Munich headed by Prof. Dr. Irmela Jeremias.

In this study, a competition-based patient-derived xenograft (PDX) mouse model was chosen to evaluate the role of FBXL6 as a novel vulnerability in AML. In this setting, PDX cells expressing a control sgRNA are simultaneously injected into mice with PDX cells harboring the desired knockout (KO) in a 1:1 ratio for competition. Control and KO are distinguished by different fluorescent markers, which are analyzed by flow cytometry.

To this end, PDX cells were generated by injection of primary patient cells into immunocompromised NOD scid gamma (NSG) mice (NOD.Cg-Prkdc^{scid} IL2rg^{tm1Wjl}/SzJ) with subsequent re-isolation and serial transplantation into secondary recipient mice (Vick et al., 2015). For CRISPR/Cas9-based knockouts, PDX cells were lentivirally transduced to generate stable Cas9-overexpression cells, which were then amplified by serial transplantation into donor mice. Lentiviral particles encoding sgRNAs were concentrated using cellulose membrane concentrating columns (Amicon® Ultra-15 Centrifugal Filters, Millipore) according to the manufacturer's protocol. Virus titration was performed by transduction of NALM-6 cell lines with subsequent flow cytometric analysis of the transgene marker. PDX-Cas9 cells were transduced overnight with the lentiviral constructs and polybrene (8 µg/ml). After recovery of four days, cells were FACS-sorted for pure populations and mixed 1:1 (sgControl marked by T-Sapphire and sgFBXL6 marked by BFP) before injection into NSG mice. After two or three weeks, mice were sacrificed. Cells isolated from bone marrow (BM) and spleen were analyzed by flow cytometry to determine the ratio between sgFBXL6 and sgCtrl. BM cells from femur, tibia, sternum, and spine were filtered and washed with PBS. To isolate splenic cells, spleens were smashed and isolated using a Ficoll density gradient (centrifugation at 400xg for 30 min at RT) and washed with PBS.

3.2.8 Statistical Analysis

All quantified experiments were performed in triplicates, meaning three independent biological replicates. The non-quantified immunoblot data generally shows results representative of at least two independent experiments. Statistical analyses of the results were performed with the GraphPad Prism software. Depending on the type of data, significance was calculated using the Logrank test (Mantel-Cox), Student's t-test, one-sample t-test, or one-way ANOVA, according to assumptions of the test. Statistical analysis of relative ratios was performed using one-sample t-tests with hypothetical means of 1.0. The error bars shown in the figures represent the mean ± standard deviation (S.D.). The P values are denoted in the figure legends where a statistically significant difference was found: *, $P < 0.05$; **, $P < 0.01$; ***, $P < 0.001$; ****, $P < 0.0001$.

4 Results

This study was performed as a collaborative project in the research group of Prof. Dr. Florian Bassermann at Klinikum rechts der Isar der TUM with help from collaborators at other institutes and colleagues within the research group. To ensure a comprehensive understanding of the project, relevant data obtained by other researchers are also presented here. The respective contributions are indicated in text and figure legends.

4.1 Characterization of FBXL6 in AML

Despite intense research on the genomic level, AML remains a deadly disease in urgent need of new actionable vulnerabilities. Investigation of post-translational modifications such as ubiquitylation holds great promise to identify new targets in AML. FBXL6 is the substrate recognition adaptor of a ubiquitin ligase, which was identified as a new vulnerability in AML in a CRISPR/Cas9 dropout screen, performed by Dr. David Brockelt.

4.1.1 FBXL6 is overexpressed in AML patient samples

To evaluate the role of FBXL6 as a new vulnerability in AML, the expression of over 1,000 ubiquitin-related genes were analyzed in a large AML patient cohort encompassing over 700 cases (data provided by T. Haferlach and W. Walter from MLL Munich Leukemia Laboratory, Stengel et al. 2020).

Among the 72 F-box protein genes, only four genes (FBXO41, FBXL6, FBXL19, and FBXW9) showed significantly enriched mRNA expression in AML samples compared to healthy bone marrow controls (n=64), with FBXL6 being the second highest hit (Fig. 7a). Taking all analyzed genes into account, FBXL6 was among the top five upregulated genes. Strikingly, FBXL6 was overexpressed in 95% of all cases (Fig. 7b). High FBXL6 expression was observed in all AML subtypes according to the current WHO classification (Khoury et al., 2022), while patients harboring PML-RARA translocation showed the highest median expression (Fig. 7c). Survival analysis of all AML patients revealed that those with high levels of FBXL6 mRNA (n=223) had slightly decreased overall survival compared to those with low levels (n=192) (Fig. 7d). However, the difference was not statistically significant. To ensure high consistency, the MLL cohort comprised intensively treated patients only. In order to gain a broader view of FBXL6 in AML patient samples, publicly available datasets from The Cancer Genome Atlas (TCGA) (Weinstein et al., 2013) and BeatAML2.0 (Bottomly et al., 2022) projects were additionally analyzed, which include samples from different disease stages.

In line with the results from the MLL cohort, high FBXL6 mRNA levels correlated weakly with worse overall survival in the TCGA dataset comprising 200 AML patient samples (Fig. 8a). A similar analysis of the larger BeatAML2.0 study (n=671) demonstrated a marginal trend toward decreased survival in the FBXL6 high group only at late time points starting at 60 months (Fig. 8b). Interestingly, samples from the BeatAML2.0 cohort showed a correlation between FBXL6 expression and risk stratification according to the European LeukemiaNet (ELN) (Döhner et al., 2017) standards. Patients classified as adverse risk had significantly higher levels of FBXL6 compared to those categorized as favorable (Fig. 8c).
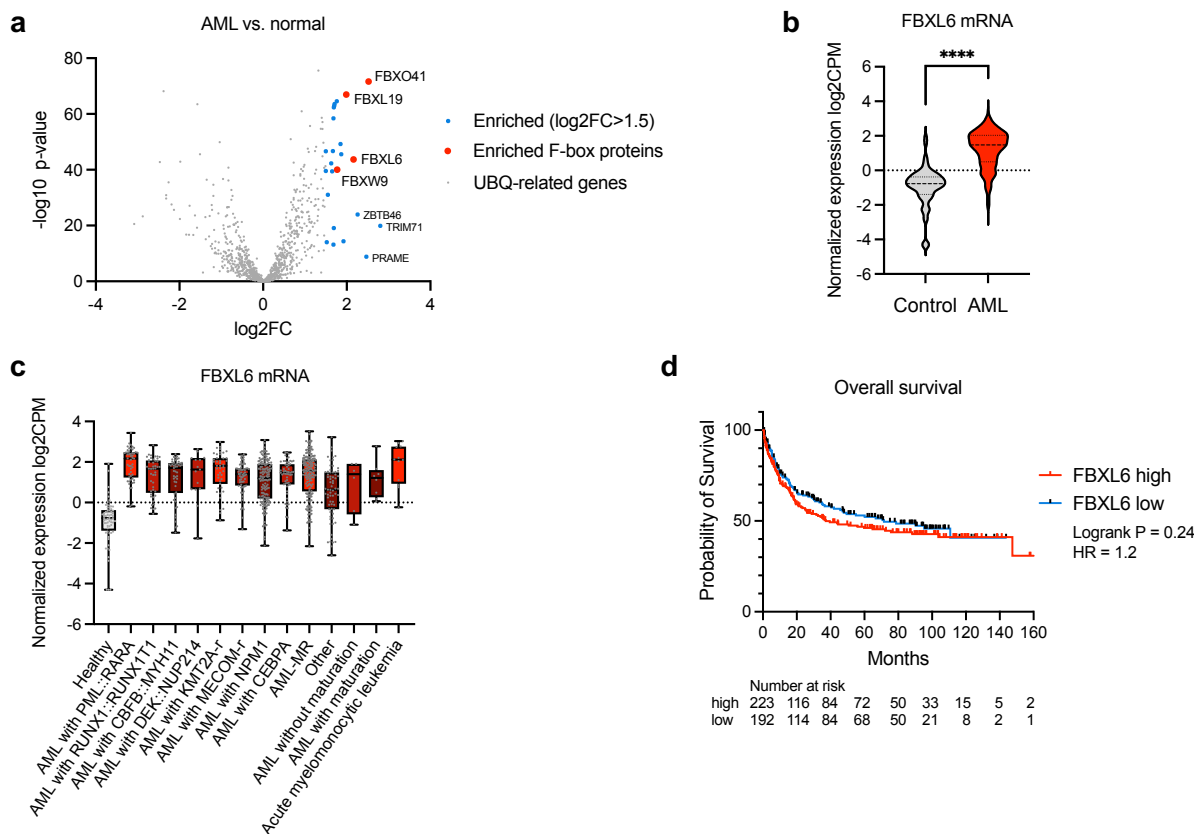
Figure 7 FBXL6 is significantly overexpressed in AML patient samples encompassed in the MLL cohort.
(a) Differential gene expression analysis of 1,041 Ubiquitin (UBQ)-related genes in the MLL AML patient cohort (n=762) compared to total bone marrow controls from healthy donors (n=64). Enriched in AML versus control: log2FC > 1.5, significant: P < 0.05 by Student's t-test. **(b)** Individual values from (a) for FBXL6 mRNA expression in AML patients and healthy controls. CPM, counts per million reads mapped. ****, P < 0.0001, by Student's t-test. **(c)** Individual values from (a) for FBXL6 mRNA expression grouped by specific AML subtype. Classification according to the current WHO guidelines, subtypes with min. 6 cases are shown. **(d)** Kaplan-Meier-Plot for overall survival comparison between the groups FBXL6 high (above the median that is marked in (a) with a dashed line, log2CPM range 1.48 - 3.43, n=223) and low (below the median, log2CPM range -1.82 - 1.48, n=192). Logrank P by Mantel-Cox test, Hazard ratio (HR) by Mantel-Haenszel test. [Data for a-d provided by collaborators from MLL Munich, T. Haferlach, and W. Walter (Stengel et al., 2020).]

Furthermore, the BeatAML2.0 dataset was explored regarding clinical attributes comparing patients with high versus low FBXL6 expression. Basic patient characteristics were similar in the two groups since no differences between FBXL6 high and low were observed for sex distribution, age, and blast count in the bone marrow and peripheral blood (data not shown). In contrast, differences were observed regarding mutation profiles and blast morphology. FLT3 mutations were slightly more frequent in FBXL6 high patients (110/335, 32.8%) compared to FBXL6 low (94/335, 28.1%), while NPM1 mutations occurred significantly more often in FBXL6 low (106/335, 31.6%) versus FBXL6 high patients (68/265, 20.4%) (Fig. 9a). Both increased FLT3 mutations and decreased NPM1 mutations in the FBXL6 high group point toward a correlation of high FBXL6 expression with a poorer prognosis (Fig. 9b), which is in line with the ELN-2017 stratification pattern described above (Fig. 8c). Differences in blast morphology were mainly found for patients categorized in the M3 class according to the French-American-British (FAB) classification (Bennett et al., 1976). Patients with FBXL6 high (13/166, 8%) were more than twice as likely to be classified as M3 compared to FBXL6 low (5/156, 3%), which is consistent with the finding from the MLL cohort, where FBXL6 expression was highest in PML-RARA translocated AML patients (Fig. 7c).

Taken together, FBXL6 was found to be highly overexpressed in AML patient samples on the transcriptional level, which is likely associated with poorer prognosis.
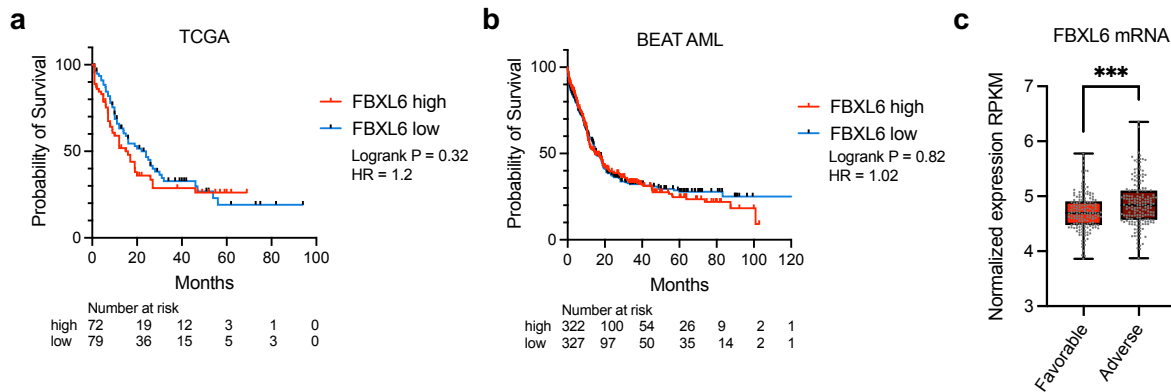
Figure 8 High FBXL6 levels are potentially associated with decreased survival and adverse risk in AML patients. (a) Kaplan-Meier-Plot from The Cancer Genome Atlas (TCGA) study (Weinstein et al., 2013) for overall survival comparison between the groups FBXL6 high (above median, log2RSEM range 8.73 – 11.02, n=72) and low (below median, log2RSEM range 6.88 – 8.72, n=79). RSEM, RNA-Seq by Expectaition-Maximization. **(b)** Kaplan-Meier-Plot from the BeatAML2.0 study (Bottomly et al., 2022) for overall survival comparison between the groups FBXL6 high (above median, RPKM range 4.79 – 6.35, n=322) and low (below median, RPKM range 3.66 – 4.78, n=327). (a-b) Logrank P by Mantel-Cox test, Hazard ratio (HR) by Mantel-Haenszel test. **(c)** Individual FBXL6 mRNA expression values from the BeatAML2.0 study for comparison of favorable and adverse risk patients classified according to the European LeukemiaNet (ELN-2017) guidelines. RPKM, reads per kilobase of transcript per million reads mapped. ***, $P < 0.001$, by Student's t-test.
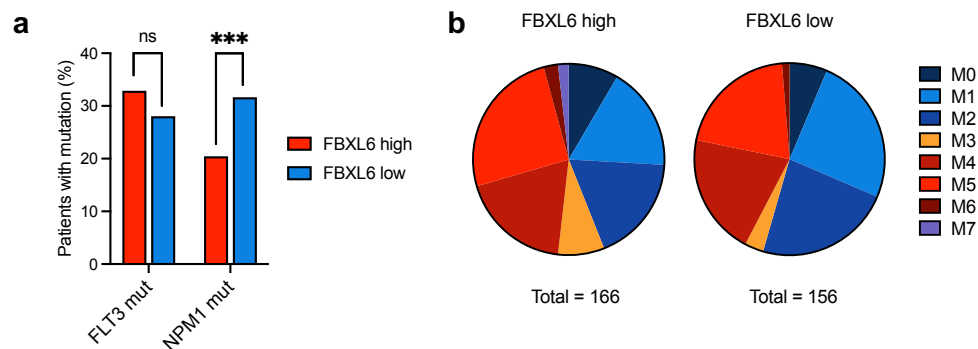
Figure 9 High FBXL6 mRNA expression is associated with genetic markers for a worse prognosis. (a) Relative number of patients from the BeatAML2.0 study (Bottomly et al., 2022) with FLT3 or NPM1 mutation, respectively. Variant allele frequency (VAF) > 5%. Comparison of FBXL6 high (above median, RPKM range 4.79 – 6.35, n=333) versus low (below median, RPKM range 3.66 – 4.78, n=335). ***, $P < 0.001$; ns, not significant by Student's t-test. **(b)** Relative distribution of patients from the BeatAML2.0 study categorized into M0-M7 AML subtypes according to French-American-British (FAB) classification (Bennett et al., 1976). Comparison of FBXL6 high (above median, RPKM range 4.79 – 6.35, n=166) versus low (below median, RPKM range 3.66 – 4.78, n=156).

4.1.2 FBXL6 is highly expressed in various cancer entities

To elucidate, whether FBXL6 overexpression was specific for AML or FBXL6 rather represents a more general oncogene across cancer entities, the large gene expression dataset of cancer cell lines deposited on the Dependency Map portal (DepMap Consortium, 2018) was analyzed. Cell lines from myeloid cancers, mainly comprising AML cell lines, showed the second-highest median FBXL6 mRNA expression (Fig. 10a). Notably, most cancer cell lines from various entities had much higher FBXL6 levels compared to non-

cancerous fibroblasts, hinting at a pro-tumorigenic role of FBXL6. On the protein level, FBXL6 expression was highest in cancer cell lines from the ovary and fallopian tube, while myeloid cell lines ranked at position five (Fig. 10b). Since the proteomics dataset lacked a non-cancer control, no conclusion on overexpression in cancer versus normal cells could be drawn on the protein level. In summary, FBXL6 is highly expressed in various cancer entities on transcriptional and translational levels, and cancer cell lines from the myeloid lineage were found among the highest-expressing lineages.
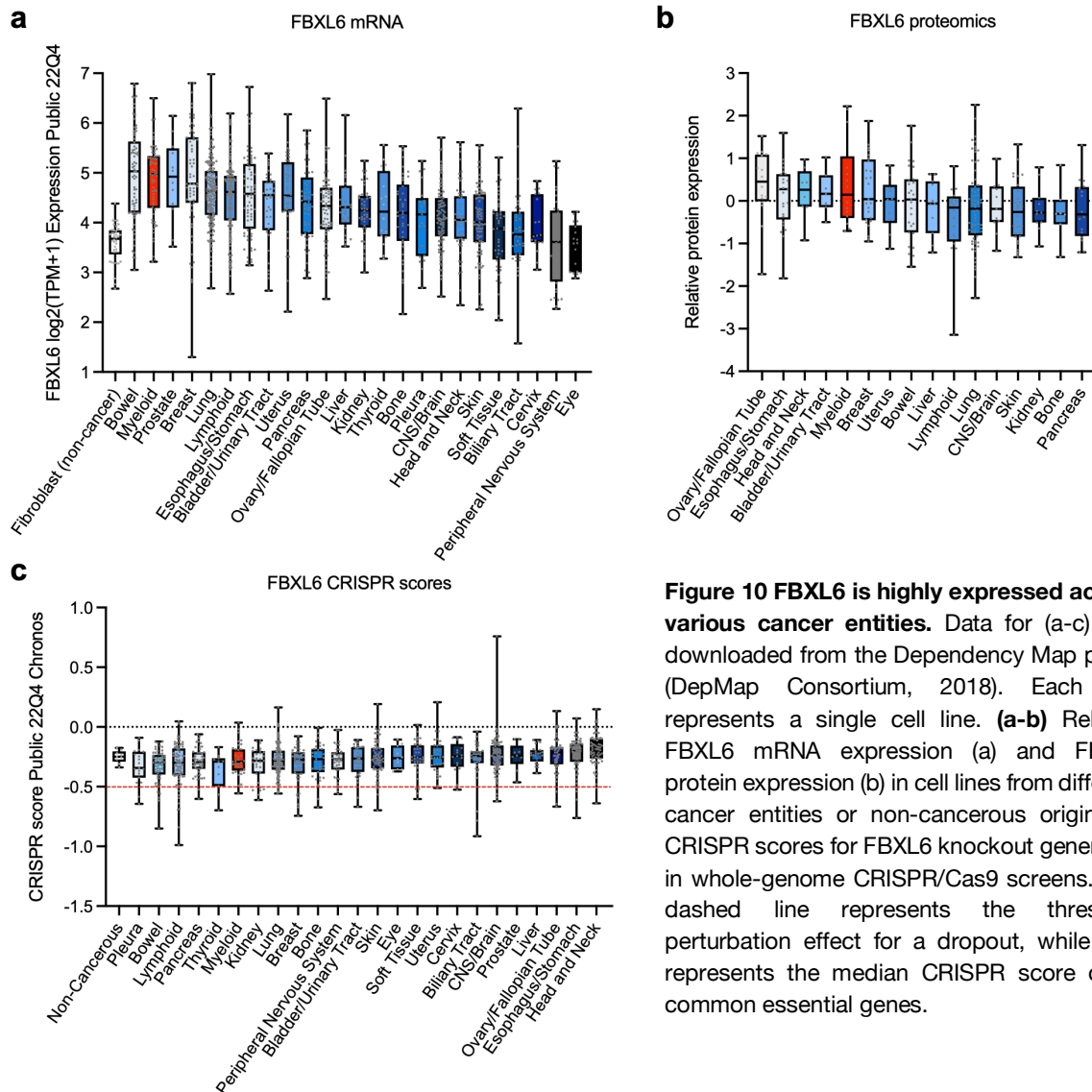
Figure 10 FBXL6 is highly expressed across various cancer entities. Data for (a-c) was downloaded from the Dependency Map portal (DepMap Consortium, 2018). Each dot represents a single cell line. **(a-b)** Relative FBXL6 mRNA expression (a) and FBXL6 protein expression (b) in cell lines from different cancer entities or non-cancerous origin. **(c)** CRISPR scores for FBXL6 knockout generated in whole-genome CRISPR/Cas9 screens. Red dashed line represents the threshold perturbation effect for a dropout, while -1.0 represents the median CRISPR score of all common essential genes.

Next, the functional genomics data deposited on DepMap was utilized to investigate whether FBXL6 serves as an AML-specific dependency or alternatively as a common vulnerability in various cancer types. The analyzed data comprised CRISPR scores from genome-wide CRISPR/Cas9 dropout screens performed in over 1,000 cell lines from 24 different cancer entities plus nine non-cancerous cell lines. For FBXL6 knockout, a perturbation effect below the threshold for a dropout of -0.5 was found for total 74 cell lines from 21 entities, while none of the non-cancerous cell lines scored below the threshold (Fig. 10c). Within the myeloid lineage, the AML cell line MOLM-13 showed the strongest dependency upon FBXL6 depletion, thus confirming the results from the CRISPR screen performed by Dr. D. Brockelt (Fig. 4). Overall, the 24 cancer entities showed modest

perturbation effects upon FBXL6 knockout, with median scores ranging from the biggest effect of -0.34 in pleural cancer cells to the smallest effect of -0.19 in cell lines from head and neck cancers. Cell lines from the myeloid lineage, including 24 AML cell lines, ranked at position six with a median score of -0.29. Taken together, FBXL6 likely serves as a moderate dependency in various cancer entities.

4.1.3 AML cell lines show two forms of FBXL6 in immunoblots

In order to validate the observations from the publicly available DepMap cell line data and to choose the most appropriate cell line systems to investigate FBXL6 in further experiments, a large cell line panel was analyzed regarding FBXL6 expression. First, whole-cell lysates were prepared from leukemic cell lines using the standard lysis buffer containing commonly used protease and phosphatase inhibitors. FBXL6 protein levels varied across the 14 different leukemia cell lines without showing a clear preference for any subtype (Fig. 11a). Interestingly, a prominent second band was detected with the FBXL6-specific antibody in AML cell lines of the FAB M4 and M5 subtypes. Relative quantification of FBXL6 mRNA levels of the leukemic cell lines did not strictly correlate with the respective protein levels, indicating post-transcriptional and/or post-translational regulation of FBXL6 expression (Fig. 11b). Next, a similar analysis of protein and mRNA levels was performed for cell lines from other lineages. In line with the data from the DepMap portal, FBXL6 expression was higher in AML cell lines compared to cell lines derived from the lung (lung adenocarcinoma, LuAD) or the lymphoid
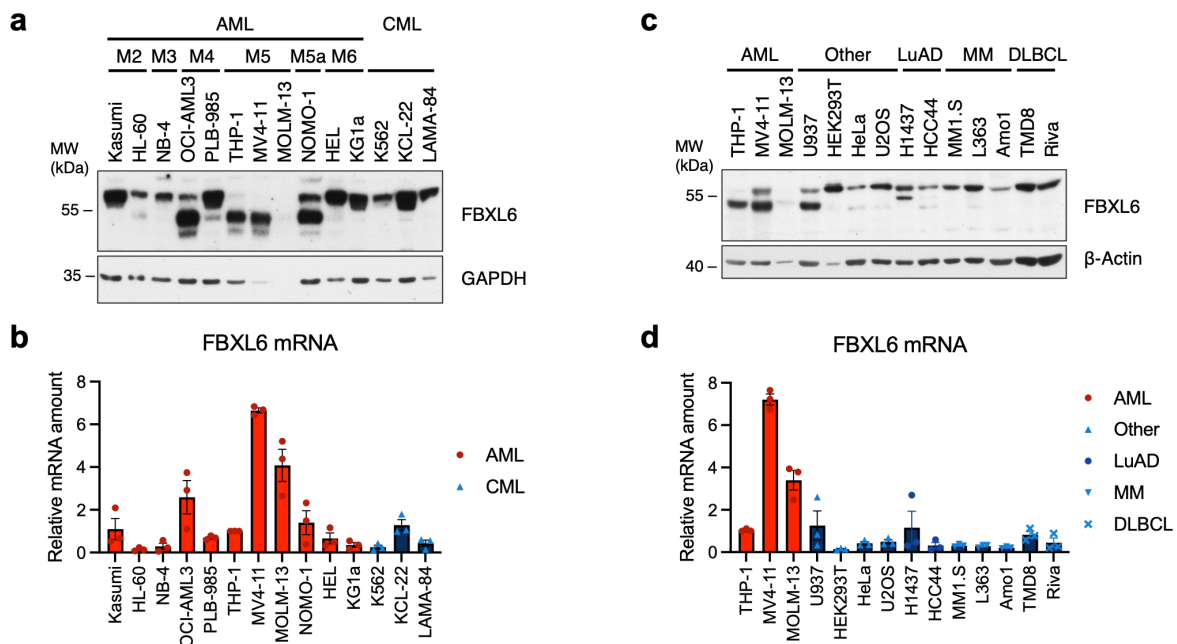
Figure 11 AML cell lines highly express FBXL6 mRNA and show a distinct band pattern for the FBXL6 protein. (a) Immunoblot analysis of whole-cell extracts prepared under standard lysis conditions derived from cell lines of different AML subtypes according to French-American-British (FAB) classification and selected CML (chronic myeloid leukemia) cell lines. Glyceraldehyde 3-phosphate dehydrogenase (GAPDH) served as a loading control. **(b)** Relative quantification of FBXL6 mRNA levels using qPCR for the cell lines in (a). Values are normalized to the expression of the housekeeping gene RPLP0 and are shown in relation to DMSO control. **(c)** Immunoblot analysis of whole-cell extracts from cell lines of different entities, including lung adenocarcinoma (LuAD), multiple myeloma (MM) and diffuse large B-cell lymphoma (DLBCL). β-Actin served as a loading control. **(d)** Relative quantification of FBXL6 mRNA levels using qPCR for cell lines in (c). Values are normalized to the expression of the housekeeping gene RPLP0 and are shown in relation to DMSO control.

lineage (multiple myeloma, MM, and diffuse large B-cell lymphoma, DLBCL), both in immunoblots and qPCR (Fig. 11c, d). Of note, the distinct band pattern of FBXL6 detected in AML cells was not found in cells from other cancer entities. Only U937, a cell line from histiocytic lymphoma, showed a second band for FBXL6 similar to AML cells. U937 cells are commonly used as a pro-monocytic model (Skopek et al., 2023), as their morphology resembles early myeloid progenitors, indicating a common regulatory mechanism with AML cells.

Aiming to confirm the identity of the bands detected in FBXL6 immunoblots of AML lysates, THP-1 cells were transduced with three different shRNAs for acute knockdown of FBXL6 versus non-targeting control and harvested four days after infection. Immunoblot analysis of whole-cell extracts showed efficient depletion of both upper and lower running bands by FBXL6 knockdown as compared to control cells (Fig. 12a). Thus, the prominent bands detected by the antibody represented two distinct forms of FBXL6 at approximately 59 kDa and 54 kDa, herein termed FBXL6-59kDa and FBXL6-54kDa, respectively.

Since 59 kDa represented the predicted molecular weight of FBXL6, the lower-running FBXL6-54kDa might be produced by a so far unknown shorter isoform or by a cleavage mechanism. To test this hypothesis, FBXL6 overexpression constructs were generated with a FLAG-tag on the C- or N-terminus of the canonical isoform of FBXL6 (isoform 1). THP-1 cells were transduced with C-FL-FBXL6 versus N-FL-FBXL6 or empty vector control (EV) and sorted by FACS for infected cells. After a few days of recovery, cells were harvested and subjected to cell lysis and immunoblot analysis. C-FL-FBXL6 gave rise to both forms in immunoblots stained with anti-FLAG antibody, therefore excluding that the bands represented different isoforms of FBXL6. Interestingly, N-FL-FBXL6 showed only the higher-running form of FBXL6 at approximately 59 kDa. After removing the anti-FLAG antibody using stripping buffer, membranes were analyzed with anti-FBXL6 antibody in the second step. Surprisingly, both forms were visible in the FBXL6 blot for either of the overexpression constructs (Fig. 12b). The discrepancy between anti-FLAG and anti-FBXL6 immunoblots strongly indicated a cleavage mechanism in the N-terminal part of FBXL6. The obvious difference in running height of the lower-running form between C- and N-terminally tagged FBXL6 strengthened this hypothesis since cleavage within the N-terminal part would also remove the FLAG-tag from N-FL-FBXL6 while the tag would still be present in C-FL-FBXL6.
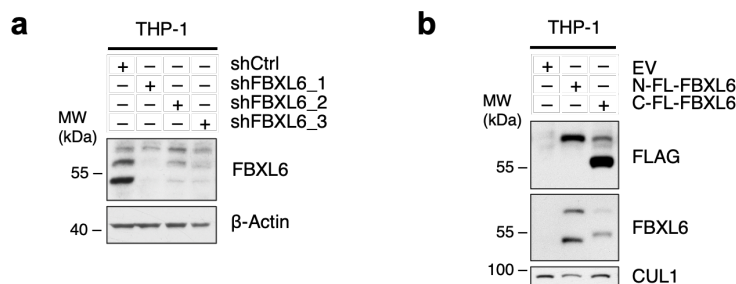
Figure 12 AML cells produce two forms of FBXL6 by cleavage. (a) Immunoblot analysis of THP-1 cells transduced with shRNA constructs targeting FBXL6 or non-targeting control (shCtrl). Cells were harvested 3 days after infection and subjected to standard cell lysis with subsequent SDS-PAGE and immunoblot analysis. β-Actin served as a loading control. **(b)** Immunoblot analysis of THP-1 cells lentivirally transduced to ectopically express FBXL6 with an N-terminal (N-FL-FBXL6) or C-terminal FLAG tag (C-FL-FBXL6), or empty vector (EV) control. Cells were FACS- sorted for infected cells subjected to standard cell lysis with subsequent SDS-PAGE and immunoblot analysis. CUL1 served as a loading control.

In summary, the analysis of selected model cell lines recapitulated high FBXL6 protein and mRNA expression in AML cells and revealed a so far undescribed AML-specific cleaved form of FBXL6. Based on the high expression, the presence of FBXL6-54kDa, and the results from the CRISPR screen performed by Dr. D. Brockelt, the four model cell lines OCI-AML3, THP-1, MV4-11, and MOLM-13 were chosen for further studies on the role of FBXL6 in AML.

4.1.4 FBXL6 is localized in the nucleus in AML cell lines

To provide a framework for the functional characterization of FBXL6 in AML, the subcellular localization of FBXL6 was determined. Therefore, immunofluorescence (IF) staining of AML cell lines coupled with confocal microscopy was performed. Using an FBXL6-specific antibody next to DNA (Hoechst33258) and cytoskeleton (α-Tubulin) staining, endogenous FBXL6 was predominantly detected in the nuclei of MV4-11 and MOLM-13 cells (Fig. 13a). Since the fluorescence signal for FBXL6 remained low despite experimental optimization and the spherical morphology of AML cells, an additional localization to the cytoplasm or other cellular compartments could not be excluded. Therefore, AML cell lines were transduced with an overexpression construct for FBXL6 (Fig. 13b). IF staining of overexpressed FBXL6 revealed a clear nuclear localization, validating the results obtained by endogenous IF staining, and the observations by Dr. D. Brockelt in chromatin fractionation
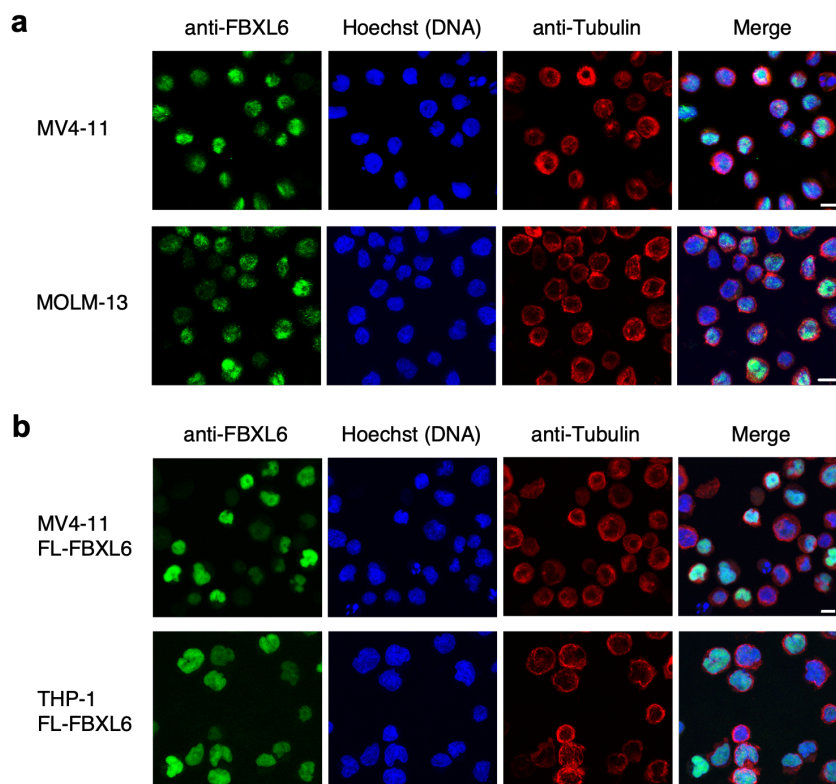
Figure 13 FBXL6 is localized in the nucleus of AML cells. (a) Representative maximum projection images of immunofluorescence staining (IF) with subsequent confocal microscopy. Wild type AML cell lines were allowed to attach to plastic 8-well chamber slides in PBS (120,000 cells per well), fixed with 4% PFA, permeabilized with IF permeabilization buffer. After blocking of unspecific binding sites using IF blocking buffer, cells were stained with the primary antibodies anti-FBXL6 (green), and anti-α-Tubulin (red) over night at 4°C, followed by washing and incubation with fluorochrome-coupled secondary antibodies. Nuclei were counterstained using Hoechst33258 (blue). **(b)** Representative maximum projection IF images of AML cell lines transduced with lentiviral FLAG-FBXL6 overexpression constructs. Staining procedure as in (a). Scale bars represent 10 µm.

experiments (Fig. 5). Thus, it was concluded that FBXL6 is localized in the nucleus in AML cells.

4.1.5 FBXL6 is regulated upon myeloid differentiation

AML is characterized by a differentiation block of immature cells in the bone marrow and blood, which causes uncontrolled proliferation of these cells. Thus, oncogenic drivers in AML often have differentiation-inhibiting and/or proliferation-promoting functions. In order to investigate a possible relationship between FBXL6 and myeloid differentiation, THP-1 and OCI-AML3, two commonly used model cell lines for myeloid differentiation studies, were treated with the differentiation-inducing agent ATRA (all-trans-retinoic acid) (Fig. 14a). Upon immunoblot analysis of treated THP-1 cells, the FBXL6 band pattern markedly shifted from a dominance of the cleaved form to the higher running form after 6 hrs of ATRA exposure. In
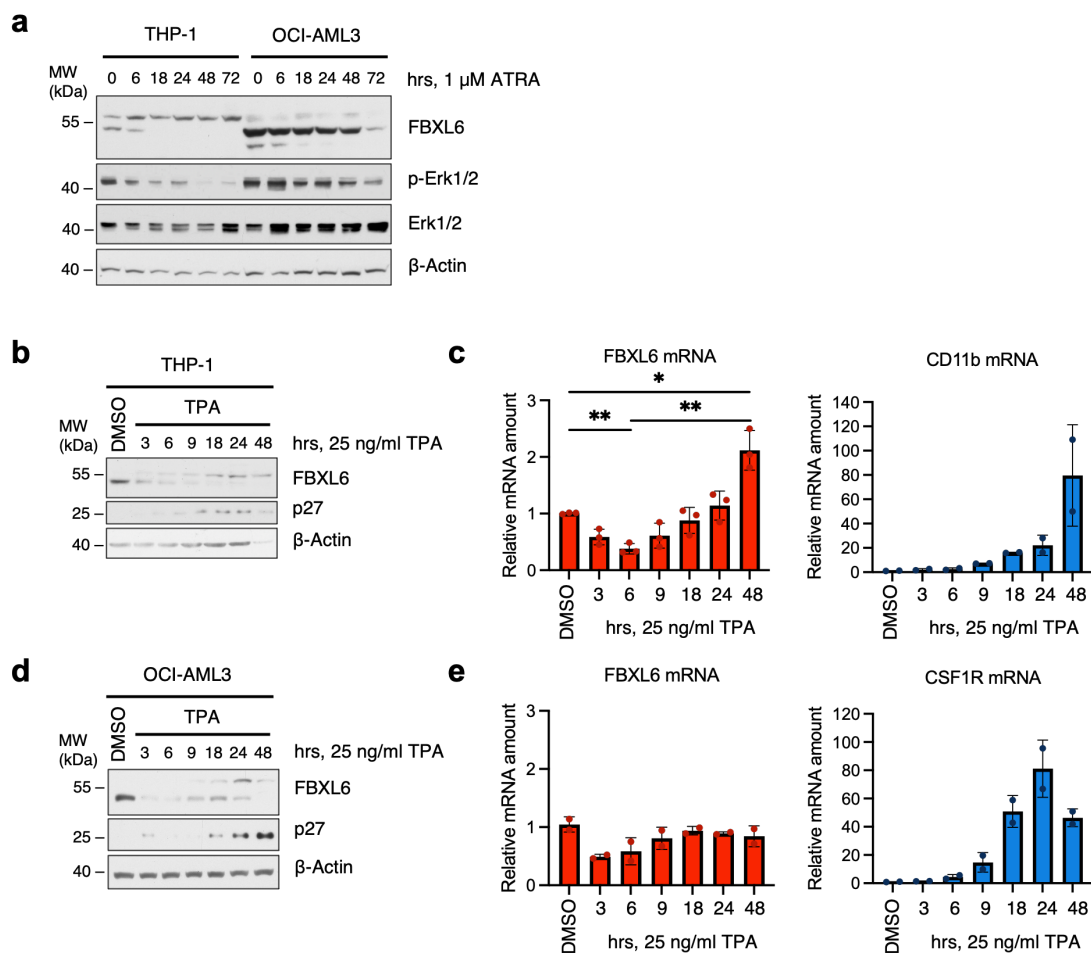
Figure 14 FBXL6 is regulated upon myeloid differentiation. (a-c) Immunoblot analysis of whole-cell extracts prepared under standard lysis conditions. β-Actin served as a loading control. **(a)** Immunoblot analysis of THP-1 and OCI-AML3 cells treated with all-trans-retinoic acid (ATRA), harvested after the indicated time points. **(b)** Immunoblot analysis of THP-1 cells treated with 12-O-Tetradecanoylphorbol-13-acetate (TPA) for the indicated timepoints or with DMSO as a control for 24 hrs. **(c)** Relative quantification of FBXL6 and CD11b mRNA levels from samples in (a) and two additional biological replicates. Values are normalized to the expression of the housekeeping gene RPLP0 and are shown in relation to DMSO control. **(d)** Immunoblot analysis of OCI-AML3 cells treated with TPA for the indicated timepoints or with DMSO as a control for 24 hrs. **(e)** Relative quantification of FBXL6 and CSF1R mRNA levels from samples in (d) and two additional biological replicates. Values are normalized to the expression of the housekeeping gene RPLP0 and are shown in relation to DMSO control. *, $P < 0.05$; **, $P < 0.01$, by Student's t-test.

OCI-AML3, where FBXL6-54kDa was much more pronounced in untreated cells than in THP-1 cells, the lower form was decreased without an increase of FBXL6-59kDa. Furthermore, the downregulation of FBXL6 happened much later in OCI-AML3 compared to THP-1, which correlated with a later onset of differentiation, indicated by decreased p-Erk1/2, a common marker for cell proliferation and differentiation (Shaul & Seger, 2007).

To rule out drug-specific effects, both cell lines were treated with another differentiation-inducing agent, TPA (12-O-Tetradecanoylphorbol-13-acetate / PMA, Phorbol 12-myristate 13-acetate). In line with ATRA treatment, exposure to TPA produced a clear shift from FBXL6-54kDa to the higher running form, for both TPH-1 and OCI-AML3, while inducing a cell cycle arrest in G1, marked by p27 upregulation (Fig. 14b, d). When FBXL6-59kDa was upregulated, the total FBXL6 protein levels were decreased when compared to untreated cells. To investigate, whether this was caused by transcriptional downregulation of FBXL6, a qPCR analysis was performed. Upregulation of CD11b or CSF1R confirmed myeloid differentiation upon TPA treatment in THP1 and OCI-AML3, respectively (Fig. 14c, e). In THP-1, FBXL6 mRNA was significantly downregulated after 6 hrs, followed by a significant upregulation after 48 hrs. Hypothesizing, that the cleaved form of FBXL6 was stemness promoting, the upregulation of FBXL6 mRNA could be interpreted as a potential compensatory mechanism. However, qPCR of TPA-treated OCI-AML3 cells did not replicate any changes in FBXL6 mRNA levels.

Taken together, forced myeloid differentiation of AML cells causes a specific shift from FBXL6-54kDa to the higher running FBXL6-59kDa, which hints at a functional link between FBXL6 cleavage and the stemness of AML cells.

4.2 FBXL6 depletion reduces the proliferation of AML cell lines

The observed dropout phenotype of FBXL6-depleted AML cells (Fig. 4) can be a result of different cellular mechanisms such as an increase in cell death, a defect in cell cycle progression, or failures in other pathways such as metabolism or releasing the differentiation block of myeloid blasts. To address this question, AML cell lines were transduced with sgRNAs targeting FBXL6 versus non-targeting control (sgCtrl) and sorted by FACS for pure populations three days after infection. For two weeks, sorted cells were followed up regarding their viability, proliferation, and differentiation status. The two FLT3-ITD positive cell lines MV4-11 and MOLM-13 were chosen for these experiments due to the significant dropout upon FBXL6 depletion in competition-based experiments by Dr. D. Brockelt and the highest dependency scores compared to other AML cell lines in CRISPR screens found in the DepMap database (Fig. 10).

Immunoblot analysis of whole-cell extracts confirmed the efficient depletion of FBXL6 (Fig. 15a). To determine the cell viability and basic metabolic activity, cells were counted using the trypan blue exclusion method and subjected to an MTS viability assay that measures mitochondrial activity via metabolization of the substrate tetrazolium into the colored product formazan. While the relative number of viable cells was moderately depleted to 80% upon FBXL6 knockout in MV4-11 cells, MOLM-13 cells were reduced to approximately 60% compared to sgCtrl (Fig. 15b). The cell viability measured by MTS metabolization was consistent with the cell counts, indicating the reduction in the MTS signal was due to reduced cell numbers rather than a metabolic defect with reduced mitochondrial activity (Fig. 15c).

Interestingly, the strongest reduction in cell viability was observed 7 days after infection and did not drop further at later time points. Instead, there was even a tendency of recovery, hinting at compensatory mechanisms.
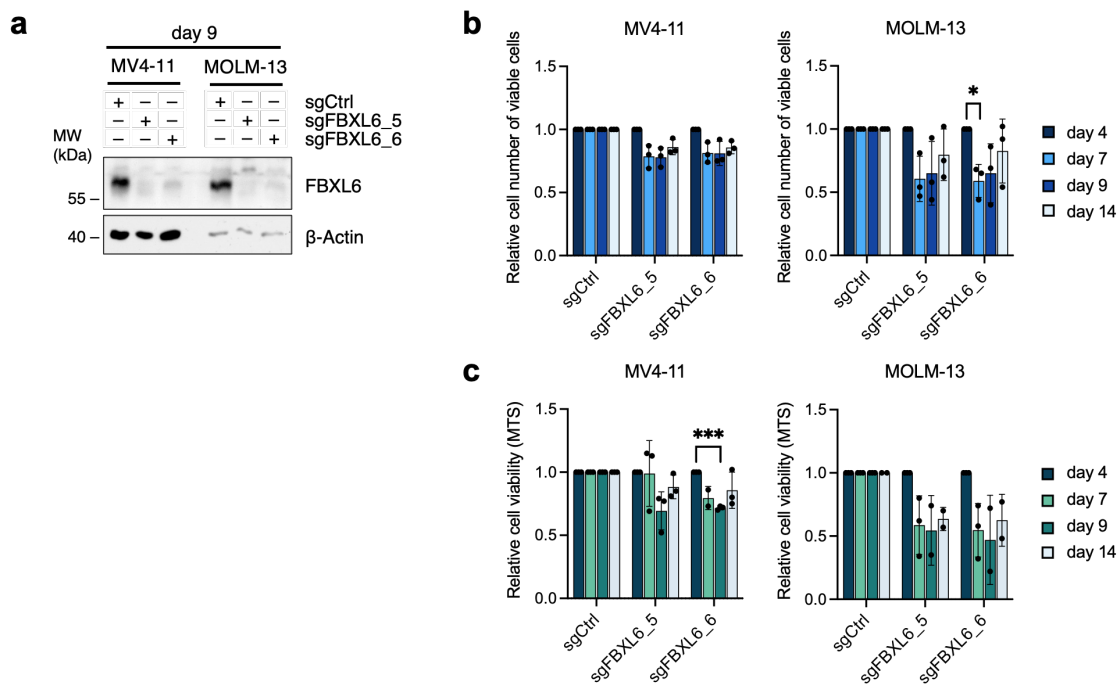
Figure 15 FBXL6 depletion reduces the proliferation of AML cell lines. (a) Immunoblot analysis of AML Cas9 cell lines that were transduced with GFP-expressing sgRNA constructs targeting FBXL6 or non-targeting control (sgCtrl) and FACS sorted for infected cells on day 3 post-infection. Cells were harvested 9 days post-infection and whole-cell extracts prepared under denaturing lysis conditions were subjected to SDS-PAGE and immunoblot analysis. β-Actin served as a loading control. **(b)** Cells from (a) and two additional biological replicates were counted using the trypan blue exclusion method on an automatic cell counter (Vi-Cell Blu, Beckman Coulter) to distinguish viable from dead cells at the indicated time points. **(c)** Cells from (a) and two additional biological replicates were subjected to MTS viability assay using the CellTiter 96® Aqueous One Solution by Promega at the indicated time points. The resulting absorbance at 490 nm was measured with a Promega 96-well plate reader. Results in (a) and (b) are normalized to day 4 and presented in relation to sgCtrl. ***; $P < 0.001$; *, $P < 0.05$, by One sample t-test.

To elucidate whether FBXL6 depletion causes cell death, cells were stained with a fluorescent stain that permeates only damaged membranes of dead cells and thereby distinguishes dead from living cells by signal intensity measured with flow cytometry. Neither of the tested cell lines showed an increase of dead cells upon FBXL6 knockout (Fig. 16a). Especially MV4-11 cells seemed to suffer from the sorting procedure but recovered during the experiment, indicated by a general decrease in dead cells. To test whether FBXL6-depleted cells show a defect in their cell cycle progression, cells were fixed and stained with propidium iodide (PI) for determining the number of cells in a certain cell cycle phase based on the DNA content. A slight enrichment of cells in the G1 phase was observed for MV4-11 cells transduced with sgFBXL6_6 (Fig. 16b). However, this effect was not reproduced with the second sgRNA used and was completely absent for MOLM-13 cells, indicating a generally slower proliferation rather than an arrest in a specific phase of the cell cycle. To investigate whether FBXL6 knockout causes a release of the differentiation block in AML cells, the surface expression of CD11b, a well established marker for myeloid differentiation, was analyzed by flow cytometry. Comparison of sgFBXL6 with sgCtrl revealed unchanged CD11b

surface levels (Fig. 16c), indicating that the differentiation status was not affected by FBXL6 depletion.

Taken together, FBXL6 depletion causes a marked reduction of AML cell numbers, which is not caused by cell death, cell cycle arrest in a specific phase, or induction of myeloid differentiation, but rather a slowed-down proliferation rate.
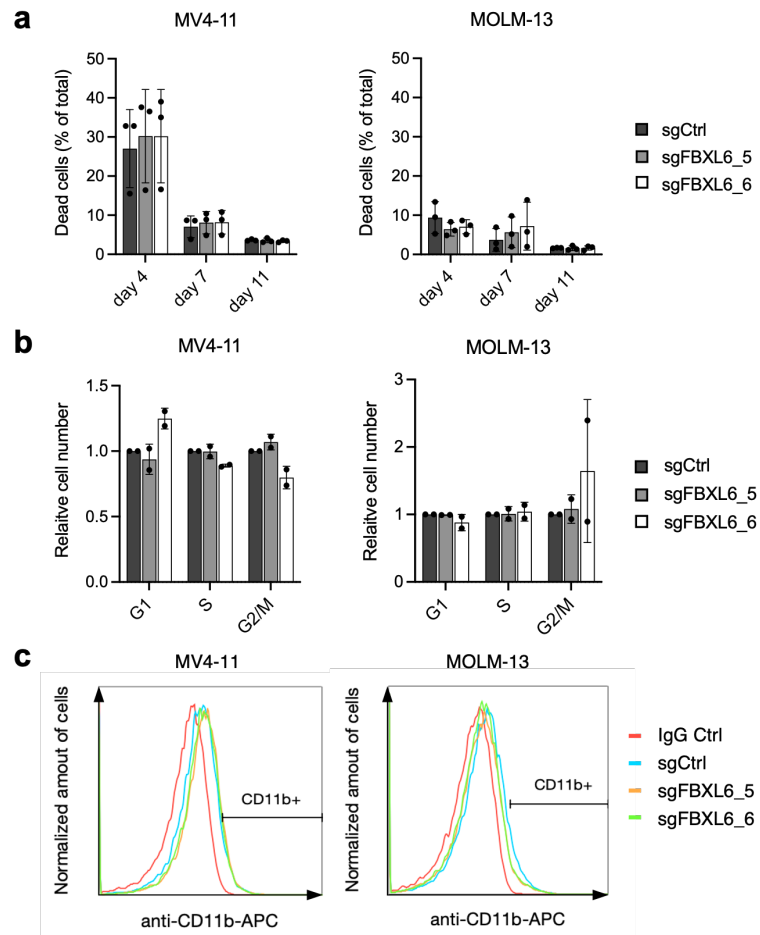
Figure 16 Reduced number of FBXL6-depleted cells does not result from cell death, cell cycle arrest in a specific phase, or myeloid differentiation. (a) Flow cytometric analysis of cells from Fig. 15, which were stained with a fluorescent viability dye (APC-coupled live/dead stain, Thermo Fisher Scientific) that permeated only damaged membranes of dead cells and analyzed by flow cytometry at the indicated timepoints. **(b)** Cell cycle analysis of cells from Fig. 15 fixed at the indicated time points, which were stained with propidium iodide (PI) for discriminating the cell cycle phases by DNA content. Results are presented in relation to sgCtrl. **(c)** Flow cytometric analysis of cells from Fig. 15 stained for CD11b-surface expression with fluorescently conjugated antibodies (anti-CD11b-APC). IgG-APC (IgG Ctrl) served as negative control for the CD11b-specific staining. [Flow cytometry for figures b and c was performed for two independent replicates. In c, results from replicate 3 are shown.]

4.3   FBXL6 might be essential for AML maintenance *in vivo*

Given that FBXL6 acts as a dependency in AML cell lines, it was investigated whether FBXL6 also exerts anti-proliferative effects *in vivo*. To this end, a patient-derived xenograft (PDX) mouse model was set up together with Romina Ludwig and Jan Philipp Schmid from the research unit Apoptosis in Hematopoietic Stem Cells (AHS) at the Helmholtz Center in Munich headed by Prof. Dr. Irmela Jeremias.

In preparation for the PDX model, first, an appropriate PDX sample had to be chosen from the PDX sample collection at the AHS. The group of Prof. Dr. Irmela Jeremias generated all PDX samples by injection of primary patient cells into immunocompromised NOD scid gamma (NSG) mice with subsequent re-isolation and serial transplantation into secondary recipient mice (Fig. 18a) (Vick et al., 2015). For CRISPR/Cas9-based knockouts, PDX cells were lentivirally transduced to generate stable Cas9-overexpression cells, which were then amplified by serial transplantation. To choose a PDX sample for this project, ideally with a high FBXL6 expression, whole-cell extracts of eight different PDX samples were subjected to immunoblot analysis. Most of the PDX samples showed FBXL6 protein levels comparable to MV4-11 cells (Fig. 17a). Interestingly, the cleaved form of FBXL6 at approximately 54 kDa observed in AML cell lines could also be detected in the PDX samples and, in some cases, was even more pronounced than in MV4-11 cells. Due to the highest FBXL6 expression, the PDX sample AML-388 was chosen for initial mouse experiments. This sample was derived from a 57-year-old male patient at initial diagnosis with an MLL-rearranged, KRAS mutated AML stratified as adverse prognosis and classified as FAB M4.
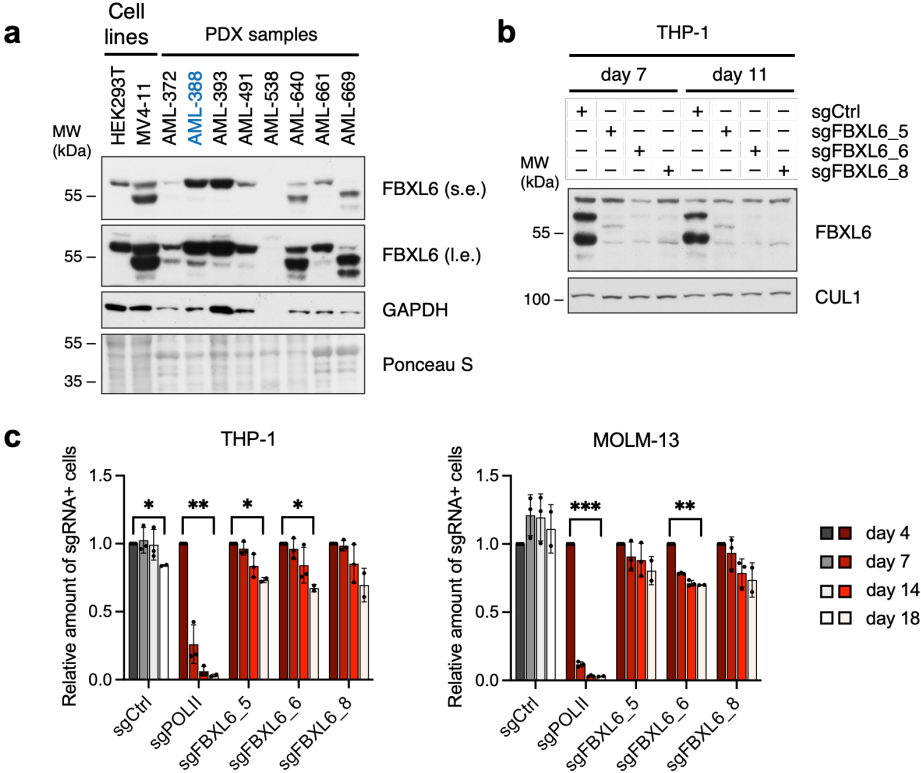
Figure 17 *In-vitro* **validation for setting up the PDX mouse model. (a)** Immunoblot analysis of whole-cell lysates prepared under standard conditions of PDX samples derived from different AML patients and two cell lines as a reference. Glyceraldehyde 3-phosphate dehydrogenase (GAPDH) and total protein staining with Ponceau S served as loading controls. S.e., short exposure; l.e., long exposure. **(b)** Immunoblot analysis of THP-1 cells transduced with sgRNA constructs targeting FBXL6 or non-targeting control (sgCtrl) cloned into the pCDH backbone used in PDX experiments. Transduced cells were selected with puromycin and harvested after the indicated time points. CUL1 served as a loading control. **(c)** Competitive growth assay for validating the pCDH-sgRNA constructs. AML Cas9 cell lines were transduced with the individual sgRNAs targeting FBXL6 (sgFBXL6) or POLII (sgPOLII), or non-targeting control (sgCtrl) at 30-50% efficiency. The ratio of sgRNA expressing to non-transduced cells was measured by flow cytometry at the indicated time points after infection and normalized to day 4. A dropout below 80% on day 18 compared to day 4 is marked by red bars. ***; $P < 0.001$; **, $P < 0.01$; *, $P < 0.05$, by One sample t-test. [PDX samples for a were provided by Prof. Dr. I. Jeremias (Vick et al., 2015); pCDH-sgRNA constructs targeting FBXL6 for b, c were cloned by R. Ludwig]

For compatibility with the established protocols for PDX models at the AHS, the sgRNAs targeting FBXL6 were subcloned into the pCDH vector by Romina Ludwig. To confirm the functionality of the pCDH-sgRNA constructs, THP-1 and MOLM-13 cells were transduced at 30-50% infection efficiency for a competitive growth assay. In parallel, a fraction of infected THP-1 cells was selected for transduced cells using puromycin and used for knockout verification. Indeed, immunoblots of THP-1 whole-cell extracts showed an efficient depletion of FBXL6 with all three different sgRNAs (Fig. 17b). Flow cytometry of THP-1 and MOLM-13 cells transduced for the competitive growth assay recapitulated the dropout effect seen with the original sgRNA constructs (Fig. 17c). To exclude sgRNA-specific effects, two sgRNAs (sgFBXL6_5 and sgFBXL6_6) were chosen for first *in-vivo* experiments.
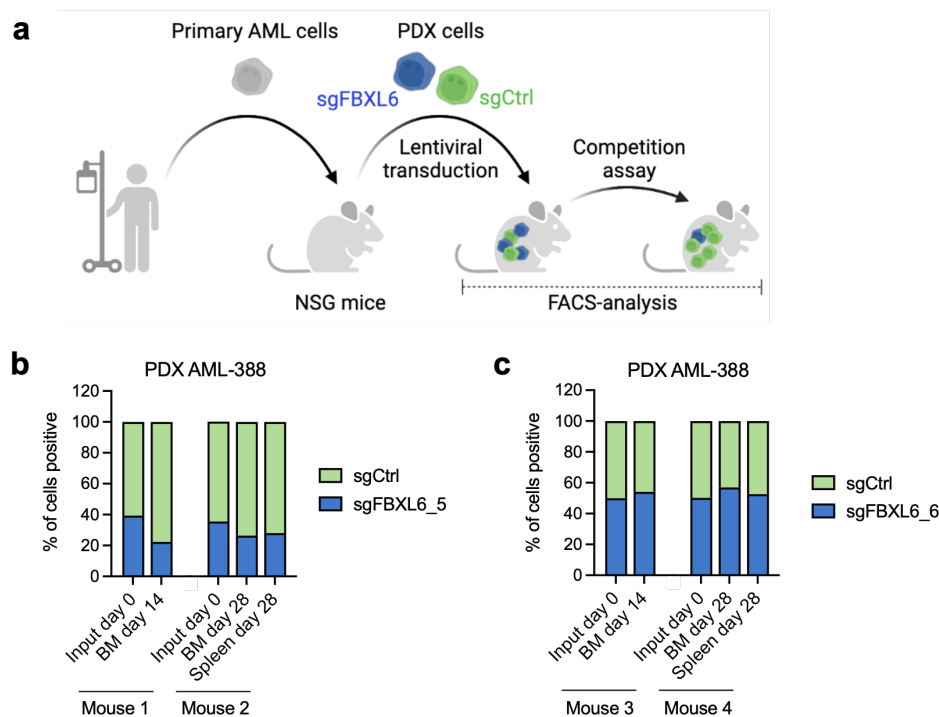
Figure 18 FXBL6 might be essential for AML maintenance *in vivo*. (a) Schematic overview of the competition assay-based PDX (patient-derived xenograft) model for FBXL6 knockout versus non-targeting sgRNA (sgCtrl) in NSG (NOD scid gamma) mice performed by the group of Prof. Dr. I. Jeremias. In brief, PDX cells were generated by tail-vein injection of primary AML cells into NSG mice. Re-isolated PDX cells were transduced with a Cas9 expression construct and amplified via serial transplantation of donor mice. Cas9-PDX cells were transduced with either sgFBXL6 or sgCtrl containing a blue (blue fluorescent protein, BFP; sgFBXL6) or a green (T-sapphire; sgCtrl) fluorescent marker. Cells were sorted by FACS for pure populations and mixed 1:1 before injection into recipient mice. After two or three weeks, mice were sacrificed. Cells isolated from bone marrow (BM) and spleen were analyzed by flow cytometry to determine the ratio between sgFBXL6 and sgCtrl. **(b-c)** Relative number of cells positive for the indicated sgRNA construct as a percentage of all human cells (PDX sample AML-388) in the bone marrow or spleen (as indicated) determined by flow cytometry after sacrificing. The input sample on day 0 represents the mixture of sorted cells before injecting into the mice. [Data in b and c was provided by R. Ludwig, J. Schmid, Prof. Dr. I. Jeremias]

The *in-vivo* competition-based experiments were set up according to the established protocol of the group of Prof. Dr. Irmela Jeremias and carried out by Romina Ludwig and Jan Philipp Schmid at the AHS (Fig. 18a). In brief, PDX-Cas9 cells were transduced with sgRNA constructs targeting FBXL6 or non-targeting control containing either a blue (BFP, sgFBXL6) or a green (T-Sapphire, sgCtrl) fluorescence marker. After recovery of four days, cells were sorted for pure populations and mixed 1:1 before injecting them into NSG mice for the

competition assay. After two or three weeks, mice were sacrificed. The earlier time point represents the early-onset stage of the disease while at the later time point of three weeks, mice have usually developed full-blown leukemia with metastases affecting the spleen. Cells isolated from bone marrow (BM) and spleen were analyzed by flow cytometry to determine the ratio between sgFBXL6 and sgCtrl. Cells infected with sgFBXL6_5 showed markedly impaired PDX leukemia growth in mice sacrificed after two or three weeks (Fig. 18b). The effect was more pronounced at the earlier timepoint, suggesting a disadvantage of FBXL6-depleted cells primarily with respect to homing into the bone marrow niche next to impaired proliferation of PDX cells in mice. However, cells infected with sgFBXL6_6 did not recapitulate the results from the other sgRNA (Fig. 18c), despite comparable behavior in *in-vitro* experiments (Fig. 17).

Thus, further experiments including a repetition of this first PDX model and the selection of a different set of sgRNAs and/or PDX samples are required to elucidate the effects of FBXL6 depletion *in vivo*.

4.4 FBXL6 acts as a K63-type ubiquitin ligase toward PPM1G

Ubiquitin ligases accomplish their biological function by modifying substrate proteins on the post-translational level. F-box proteins specifically regulate this process by acting as substrate-recognition adaptors of multi-subunit ligase complexes. Thus, identifying the ubiquitylation substrates of FBXL6 was considered one of the most important tasks in this project.

4.4.1 Ubiquitylation substrate identification via integrated data analysis

Initial work on FBXL6 carried out by Dr. David Brockelt comprised three different mass spectrometry-based screens to identify FBXL6 substrates. A short time after the project was handed over, the bioinformatic workup of those screens was completed by collaborators at the chair proteomics and bioanalytics at TUM headed by Prof. Dr. Bernhard Küster. Based on the recent findings about the so-far undescribed AML-specific cleaved form of FBXL6 (Fig. 11), an additional interactome screen was performed. In the following, data from all approaches will be integrated and subjected to cross-validation of substrate candidates.

Given that AML cells specifically harbor FBXL6-54kDa, which was only weakly or not at all present in HL-60 and HEK293T cells, another interactome screen was set up in MV4-11 cells, which show cleaved FBXL6 (Fig. 11), very high FBXL6 expression levels (Fig. 11) and a pronounced dependency on FBXL6 expression (Fig. 4). Similar to the previously conducted FLAG-IP from HL-60 cells (Fig. 6), MV4-11 cells were transduced to overexpress FLAG-tagged FBXL6 versus empty vector control and harvested in biological triplicates to perform a single-step FLAG immunoprecipitation. In contrast to the HL-60 interactome, where an N-terminal FLAG-tag was used, a C-terminal FLAG-tag was deployed to enrich both upper- and lower-running FBXL6 (described in section 4.1.3). Purified proteins were eluted from the beads using 3XFLAG-peptide, of which 5% were used for quality control, while the remaining volume was subjected to mass spectrometric analysis. Immunoblot analysis of input samples showed sufficient overexpression of FL-FBXL6 with a strong signal corresponding to the cleaved form (Fig. 19a). Silver staining of the quality control samples revealed an efficient and even enrichment of the bait protein among all three replicates (Fig. 19b). Using a BSA (bovine

serum albumin) standard in the silver staining analysis, the total amount of purified FL-FBXL6 was estimated to be 20 µg per replicate. The eluates were precipitated with 20% TCA, dried, reconstituted in a small volume of LDS buffer, and visualized with Coomassie staining after SDS-PAGE. To exclude the high amounts of 3XFLAG-peptide, which would interfere with the mass spectrometric analysis, the gel was cut below 15 kDa and the upper part of the stained gel was sent to the BayBioMS@MRI core facility, where Dr. Piero Giansanti performed mass spectrometry and data processing. A total of 456 proteins were specifically enriched in FL-FBXL6 samples over EV controls (Log2FC > 2), of which 400 proteins were statistically significant (Fig. 19c). Co-purification of the SCF-complex components SKP1 and CUL1 strengthened the hypothesis of FBXL6 being part of a functional ubiquitin ligase, replicating the results from the interactomes performed by Dr. D. Brockelt from HL-60 and HEK293T cells (Fig. 6).
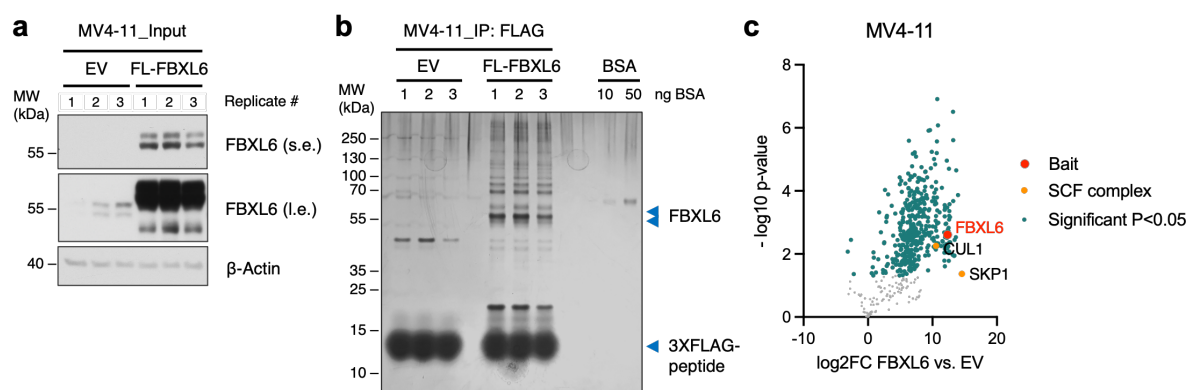
Figure 19 Interactome screening for FBXL6 substrates in MV4-11 cells. (a) Immunoblot analysis of whole-cell lysates prepared under standard conditions from MV4-11 cells transduced to express FLAG-tagged FBXL6 (FL-FBXL6) or empty vector control (EV). β-Actin served as a loading control. S.e., short exposure; l.e., long exposure. **(b)** Silver staining of FLAG immunoprecipitation (FLAG-IP) of samples in (a). After immobilization on anti-FLAG-resin and elution with 3XFLAG octapeptide, 2.5% of the eluates were separated by SDS-PAGE and visualized by silver staining before sending the remaining sample for mass spectrometric analysis. **(c)** Mass spectrometric analysis of samples in (b). Co-purified proteins were identified by mass spectrometry and log2 ratios of averaged FBXL6/EV LFQ (label-free quantification) values were plotted against the negative Log10 of the calculated p-value by Student's t-test. FC, fold change; SCF, SKP1-CUL1-F-box protein complex. [MS Data for c provided by BayBioMS@MRI core facility, Dr. P. Giansanti]

In an effort to identify robust interaction partners, which bind repeatedly to FBXL6, independent of a specific genetic background and a certain form of FBXL6, the data from all three interactome screens (presented in Fig. 6 and Fig. 19) were combined in a cross-validation approach. The cut-off for enriched proteins was set at a 2-fold enrichment (log2FC > 1) in FBXL6 samples versus EV controls to not exclude weak but relevant interactors. To avoid excluding biologically relevant substrate candidates, that were not significantly enriched, there was no cut-off for the p-values calculated in statistical tests. This procedure identified 342 proteins to be enriched in at least two of the interactome screens, while 115 proteins were enriched in all three (Fig. 20a). To enhance the probability of identifying true ubiquitylation substrates over other interaction partners, the 342 proteins were additionally cross-validated with the ubiquitome screen (DiGly-IP) from MOLM-13 cells (presented in Fig. 6). For 59 out of 342 proteins, a decrease of at least 30% in ubiquitylated peptides upon FBXL6 knockdown versus control was observed (Fig. 20b). In the next processing step, agarose-binding proteins, that were detected in more than 300 out of 716 affinity-based

interaction screens deposited on the CRAPome database (Mellacheruvu et al. 2013) and therefore deemed unspecific binders, were removed. For the remaining 24 cross-validated substrate candidates a total rank was calculated by summarizing the individual ranks among the 24 candidates from each of the four mass spectrometric screens (Fig 20c). Literature search and functional annotation clustering using the bioinformatic resource DAVID (Sherman et al., 2022) revealed that many of the candidate proteins were involved in essential pathways
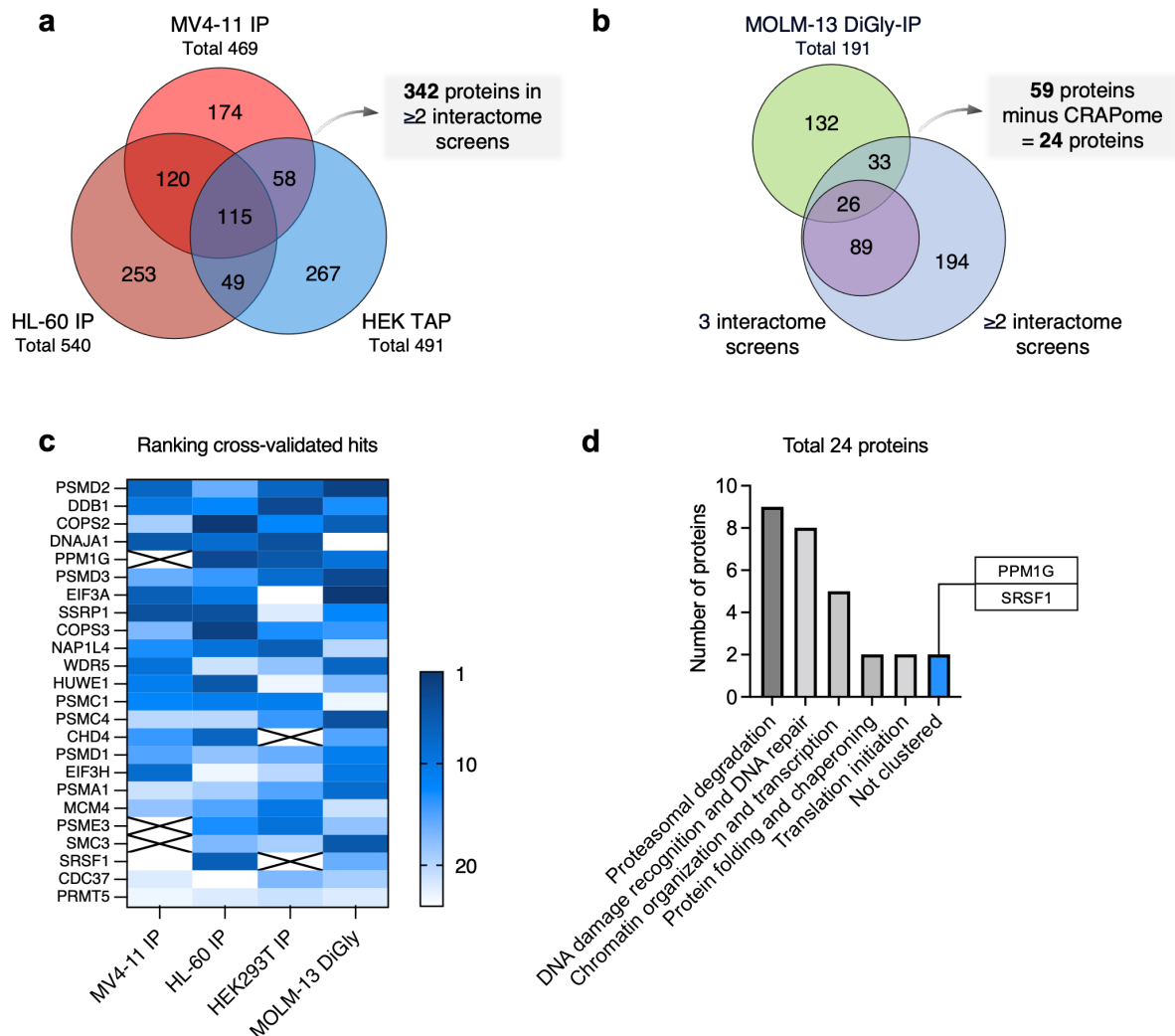
Figure 20 Cross-validation of mass spectrometry-based screens for FBXL6 substrate proteins. (a) Venn-diagram of proteins co-purified with overexpressed FBXL6 in the three different interactome screens: i) one-step FLAG-immunoprecipitations (IP) from MV4-11 (Fig. 19) and ii) HL-60 cells (Fig. 6), and iii) tandem-affinity purification (TAP) from HEK293T cells (Fig. 6). Proteins that were at least two-fold enriched in FBXL6 samples versus empty vector controls were analyzed for overlaps using the BioVenn web tool (Hulsen et al., 2008). Circle sizes represent the number of proteins identified in each condition. **(b)** Venn-diagram of proteins enriched in at least two interactome screens (total overlap in (a)) and found to be less ubiquitylated upon FBXL6 knockdown in the DiGly-IP from MOLM-13 cells (Fig. 6). The cut-off for differentially ubiquitylated peptides was set to 30% in FBXL6-depleted versus control cells. The 59 proteins within the overlap were searched for agarose-binding proteins in the CRAPome database (Mellacheruvu et al., 2013). An arbitrary cut-off of 300/716 identifications in affinity-based screens deposited on CRAPome was set to exclude unspecific binding partners, yielding 24 substrate candidates. **(c)** Heat map for ranking the cross-validated substrate candidates according to the sum of their ranks among the 24 candidate proteins in the individual substrate screens. Missing values are marked by a cross. Proteins with the overall highest rank are listed on top and proteins with the lowest rank on the bottom of the heat map. **(d)** Functional clustering of the 24 substrate candidates based on the DAVID functional annotation tool (Sherman et al., 2022) and literature search.

of the cell such as proteasomal proteins or general regulators of the DNA damage response and protein expression (Fig. 20d). Since FBXL6 depletion caused defects in AML cell proliferation of moderate effect size, it seemed reasonable to search for respective substrate proteins outside these common essential clusters. Notably, two of the candidate proteins were not found in any cluster, among which the protein phosphatase PPM1G represented the most interesting hit due to its rank among the top five of the 24 candidates and its implication in cell cycle control and cell growth (Kamada et al., 2020; Khoronenkova et al., 2012; Sun et al., 2016). The second non-clustered protein was SRSF1 which functions as a splicing factor and ranked at position 22 out of 24 (Das & Krainer, 2014). For PPM1G, two ubiquitin-remnant peptides were identified, which were 50% and 30% less abundant in FBXL6-depleted cells versus control, while the total abundance of the protein was unchanged. In the interactome screens, PPM1G was highly enriched in FBXL6 versus EV samples from both HL-60 (log2FC 4.4) and HEK293T cells (log2FC 9.4). Thus, PPM1G was chosen to be evaluated regarding its role as FBXL6 substrate.

Together, the integration of a multi-angled screening approach identified potential FBXL6 substrates, of which PPM1G represented the most promising candidate.

4.4.2 PPM1G specifically interacts with FBXL6

After cross-validation of FBXL6 substrate screens identified PPM1G as the most promising substrate candidate, a panel of validation experiments was set up together with Daniela Koch, who contributed to this part of the project while working on her medical doctorate in the group of Prof. Dr. Florian Bassermann.

First, semi-endogenous FLAG-IPs were performed from lysates of HL-60 and THP-1 cells to confirm the interaction between PPM1G and FBXL6. Both cell lines were transduced and FACS-sorted for pure populations to overexpress either C- or N-terminally FLAG-tagged FBXL6 or empty vector as a negative control. Immunoblot analysis of the IP samples revealed a weak but clear co-IP of endogenous PPM1G with both C- and N-FL-FBXL6 in HL-60 cells (Fig. 21a). However, there was no specific PPM1G co-IP detectable in THP-1 cells. Co-IP of the SCF complex components SKP1 and CUL1 were detected in all FL-FBXL6 IP samples and not in EV controls, confirming previous experiments (Fig. 6). Comparing the IP levels of the two FBXL6 forms with the amount of co-purified interaction partners, it was concluded that both FBXL6-54kDa and FBXL6-59kDa bind to PPM1G and are effective in forming the SCF complex. Since ubiquitylation of substrate proteins often leads to their proteasomal degradation, overexpression of the responsible ubiquitin ligase would supposedly result in decreased protein levels of the substrate (Komander & Rape, 2012). Here, FBXL6 overexpression did not alter the total amount of PPM1G in immunoblots of the input samples (Fig. 21a), providing a first hint toward non-proteolytic ubiquitylation.

To evaluate whether PPM1G specifically binds to FBXL6 instead of binding generally to proteins of the FBXL family, different FLAG-tagged FBXL-proteins were overexpressed alongside FL-FBXL6 in HEK293T cells. Despite varying expression levels in the input samples among the different F-box proteins, comparable FLAG-IP levels were achieved (Fig. 21b). For FBXL6, a very strong interaction with PPM1G was detected, while FBXL1 (alias SKP2) and FBXL7 showed no binding to PPM1G. For FBXL16 and FBXL3, a weak co-IP of PPM1G was found, which seemed neglectable compared to the interaction with FBXL6. Co-

immunoprecipitation of the SCF complex components SKP1 and CUL1 validated the performance of the experiment for all FBXL proteins.

Together, immunoprecipitation experiments recapitulated the binding of PPM1G to FBXL6 found in the interactome screens from HL-60 and HEK293T cells. As closely related proteins of the FBXL family failed to bind PPM1G or showed much weaker interaction with PPM1G, the binding to FBXL6 was considered to be a specific interaction.
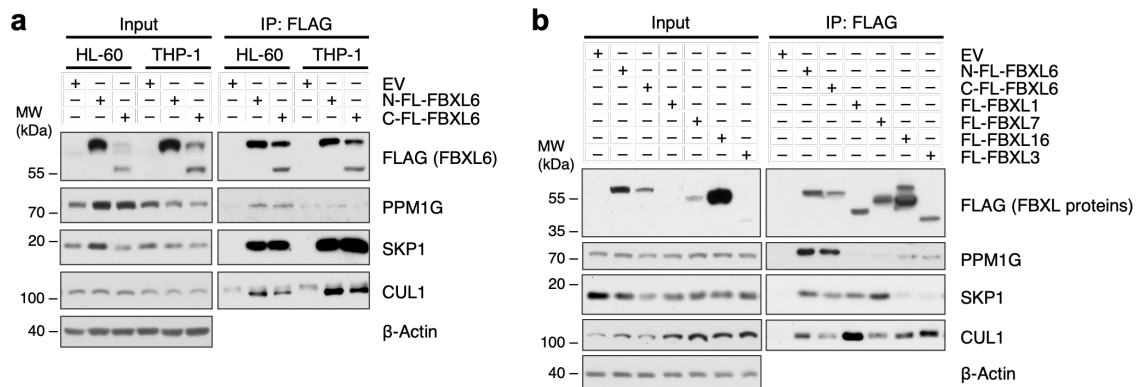
Figure 21 PPM1G specifically interacts with FBXL6. (a) Immunoprecipitation (IP) of FLAG-FBXL6 (FL-FBXL6) from HL-60 and THP-1 cells transduced with the indicated overexpression constructs or empty vector control (EV) and sorted for pure populations before harvesting and freezing of cell pellets at -80°C. Lysates using the standard lysis buffer were subjected to FLAG-IP and analyzed by immunoblot analysis. β-Actin served as a loading control. **(b)** Immunoprecipitation of FLAG-tagged proteins of the FBXL family or EV control overexpressed in HEK293T cells. 24 hrs after transient transfection with the indicated constructs, cells were harvested, and pellets were frozen at –80°C before cell lysis. Lysates were subjected to FLAG-IP and analyzed by immunoblot analysis. β-Actin served as a loading control. [Data for a and b provided by D. Koch]

4.4.3 FBXL6 modulation does not influence PPM1G protein stability

Ubiquitin ligases often influence the protein stability of their respective substrates by targeting them for proteasomal degradation. In a first attempt to test whether modulation of FBXL6 levels influences the protein abundance of PPM1G, AML cell lines were transduced with shRNA constructs targeting FBXL6 or non-targeting control. Immunoblot analysis of lysates from HL-60 and THP-1 cells after 4 days of culturing showed no change in total protein levels for PPM1G upon FBXL6 knockdown (Fig. 22a). This finding was reproduced in a similar experiment with MV4-11 and NOMO-1 cells harvested seven days after transduction (Fig. 22b). Thus, FBXL6 knockdown did not affect PPM1G total protein abundance, independently of the cell lines used or the duration of FBXL6 depletion.

In a second approach, the protein stability of PPM1G was assessed in a well-established assay using cycloheximide (CHX) to inhibit the ribosome and thereby stall protein translation in a time-dependent manner (Dietachmayr et al., 2020; Fung et al., 2018). Immunoblot analysis of THP-1 cells expressing either EV control or FL-FBXL6 revealed that PPM1G levels were decreased upon CHX treatment (Fig. 22c). Simultaneous proteasomal inhibition using MG132 reversed this effect, indicating PPM1G is degraded via the proteasome. FBXL6 overexpression did not enhance or accelerate the destabilization of PPM1G, as it would have been expected for a ligase-substrate relationship inducing proteasomal degradation of the substrate. This experiment also showed that FBXL6-54kDa was degraded by the proteasome to a similar extent as the short-lived control protein IκB-α,

while the FBXL6-59kDa was stable for the whole duration of the experiment. This accounted for endogenous as well as ectopically expressed FBXL6 and hinted at specific mechanisms differing between the two forms of FBXL6.

Taken together, PPM1G protein abundance and stability were not altered upon FBXL6 modulation.
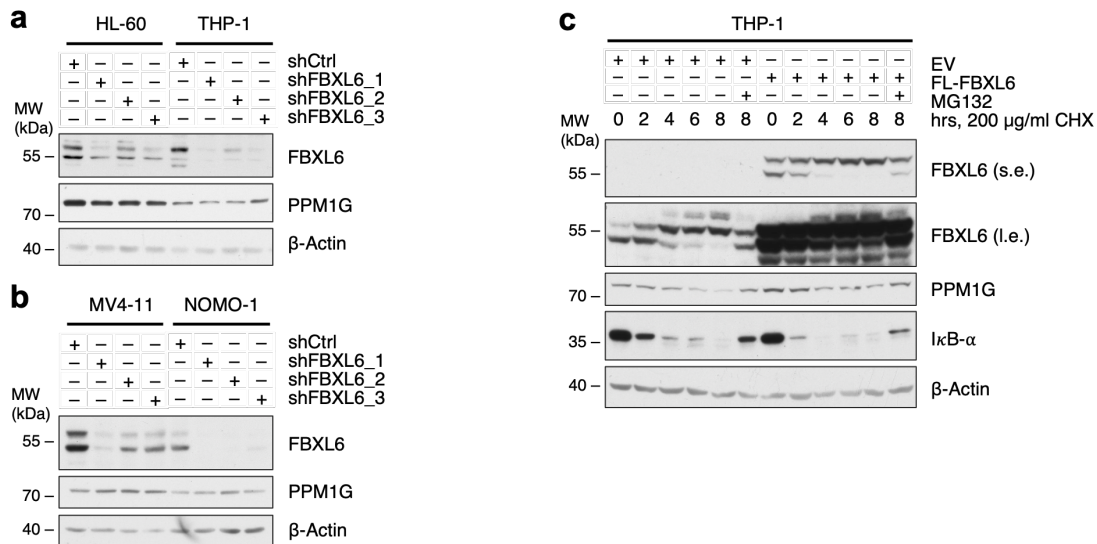
Figure 22 PPM1G stability is not altered upon FBXL6 modulation. (a) Immunoblot analysis of HL-60 and THP-1 cells harvested four days after transduction with shRNA constructs targeting FBXL6 or non-targeting control (ahCtrl). **(b)** Immunoblot analysis of MV4-11 and NOMO-1 cells harvested seven days after transduction with shRNA constructs targeting FBXL6 or non-targeting control (shCtrl). **(c)** Immunoblot analysis of THP-1 cells stably expressing empty vector (EV) or FLAG-tagged FBXL6 (FL-FBXL6) treated with 200 µg/ml cycloheximide (CHX) and 10 µM MG132. Cells were harvested at the indicated time in hours (hrs) after starting the treatment and whole-cell extracts were subjected to immunoblot analysis. Whole-cell extracts in a-c were prepared under standard lysis conditions. β-Actin served as a loading control. S.e., short exposure; l.e., long exposure.

4.4.4 FBXL6 ubiquitylates PPM1G via K63-linkage

After confirming the interaction between FBXL6 and PPM1G (Fig 21.), *in-vivo*-ubiquitylation assays were performed by Daniela Koch to establish PPM1G as a substrate of SCF-FBXL6. First, HEK293T cells were transfected with the indicated combinations of plasmids encoding for HA-ubiquitin, FL-PPM1G, and C-/N-MYC-FBXL6 to investigate the effect of FBXL6 overexpression on PPM1G ubiquitylation. Before harvesting, cells were treated with the proteasome inhibitor MG132 to allow the accumulation of ubiquitylated proteins that would otherwise be degraded by the proteasome. Whole-cell extracts were subjected to FLAG-IP under denaturing conditions, to ensure purification of FL-PPM1G without co-purification of interaction partners. Immunoblot analysis revealed a strong increase in ubiquitylated PPM1G upon FBXL6 overexpression, independent of applying the MYC tag on the C- or N-terminus of FBXL6 (Fig. 23a). The detected ubiquitin signal showed the characteristic laddering pattern from approximately the size of the protein toward higher molecular weights, representing poly-ubiquitylated forms of PPM1G. To investigate whether the increased ubiquitylation of PPM1G was specific for FBXL6 overexpression, other members of the FBXL family were tested in a similar experiment. Notably, only FBXL6 overexpression led to a strong increase of PPM1G ubiquitylation, while FBXL3, FBXL5, and FBXL16 did not have an effect (Fig. 23b). At first glance, FBXL1 might also increase PPM1G

ubiquitylation to a certain extent, but FBXL1 seemed to be co-purified with FL-PPM1G, indicated by a band on the corresponding height in MYC immunoblots. Since FBXL1 (SKP2) is known to be auto-ubiquitylated (Wirbelauer et al., 2000), the increase in the ubiquitylation signal was presumably due to the impure enrichment of FL-PPM1G in this condition.
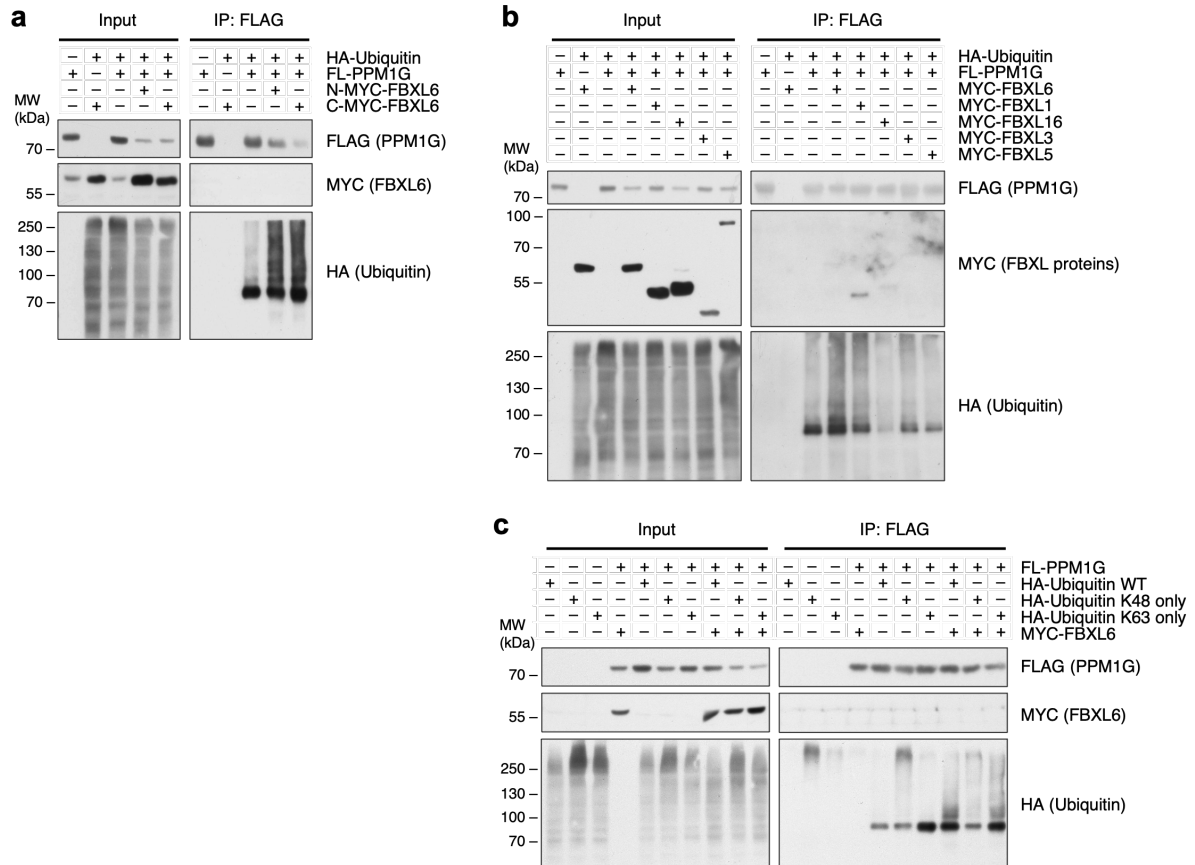
Figure 23 FBXL6 ubiquitylates PPM1G via K63-type linkage. (a) *In-vivo*-ubiquitylation assay of FLAG-tagged PPM1G (FL-PPM1G). HEK293T cells were transfected with the indicated plasmids encoding for HA-ubiquitin, FL-PPM1G, and C- or N-terminally MYC-tagged FBXL6 (C-/N-MYC-FBXL6). After 24 hours, cells were treated with 10 µM MG132 for 3 hours before harvesting. Whole-cell extracts from standard lysis were subjected to FLAG-IP under denaturing conditions with subsequent immunoblot analysis. **(b)** *In-vivo*-ubiquitylation assay of FL-PPM1G from HEK293T cells analogous to (a). Alongside MYC-tagged FBXL6, other FBXL proteins with N-terminal MYC tag were expressed as indicated. **(c)** *In-vivo*-ubiquitylation assay of FL-PPM1G from HEK293T cells upon N-MYC-FBXL6 overexpression with wild type (WT) and mutant HA-ubiquitin. Ubiquitin mutants harbor lysine to arginine mutations in six out of seven lysine residues, allowing only the indicated poly-ubiquitin linkage type. Procedure as in (a). [Data for a-c provided by D. Koch]

Since PPM1G protein stability was unaffected by FBXL6 modulation (Fig 22.), it was conceivable that FBXL6 might attach ubiquitin moieties not via the most common, degradative linkage on lysine 48 (K48), but via the second most common, non-degradative linkage on lysine 63 (K63). To test this hypothesis, mutant forms of ubiquitin that bear lysine to arginine exchanges in six out of seven residues leaving only one specific lysine to form poly-ubiquitin chains were used in another *in-vivo*-ubiquitylation assay. Recapitulating the results in Fig. 23a and 23b, overexpression of FBXL6 increased PPM1G ubiquitylation when wild type (WT) HA-ubiquitin was co-expressed (Fig. 23c). Strikingly, only the ubiquitin mutant that exclusively allows for K63-linkage reproduced the FBXL6-mediated increase in PPM1G ubiquitylation while co-expression of the K48-only mutant had no effect. The ubiquitylation

levels were similar between WT ubiquitin and K63-only mutant, suggesting that FBXL6 predominantly caused PPM1G ubiquitylation via K63-linkage.

Polyubiquitylation via K63 can serve as a signal for different cellular mechanisms including altered protein localization (Komander & Rape, 2012). To investigate whether FBXL6-mediated K63-type polyubiquitylation might affect the localization of PPM1G in AML cells, FBXL6-depleted versus control cells were subjected to immunofluorescence staining with a PPM1G-specific antibody. MOLM-13 cells transduced with sgRNA constructs and sorted for pure populations were chosen for this experiment since these cells showed a strong dependency on FBXL6 in previous assays (Fig. 4, Fig. 15). Confocal microscopy showed a clear nuclear localization of PPM1G in AML cells, which was not affected by FBXL6-depletion (Fig. 24), suggesting that FBXL6-mediated ubiquitylation might have other effects than altered localization.

Overall, *in-vivo*-ubiquitylation assays revealed specific poly-ubiquitylation activity of FBXL6 toward PPM1G via lysine 63, thereby solidifying the hypothesis of FBXL6 and PPM1G acting as a ligase-substrate pair. The biological consequences of FBXL6-mediated PPM1G-ubiquitlyation remain elusive at this point.
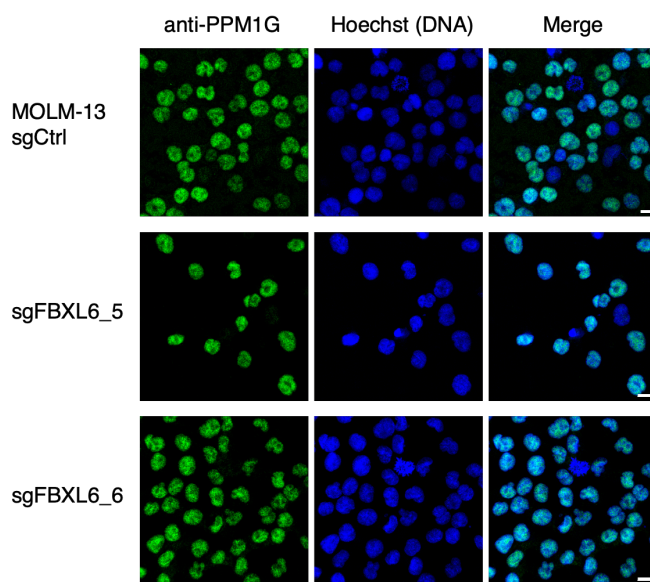
Figure 24 FBXL6 depletion does not alter PPM1G subcellular localization. Representative images of immunofluorescence staining (IF) with subsequent confocal microscopy. MOLM-13 Cas9 cells transduced with the indicated sgRNA constructs were sorted for transduced cells on day 3 after infection, attached to plastic 8-well slides (120.000 cells/well) and fixed with 4% PFA on day 6 after infection. After permeabilization and blocking, cells were stained with the primary antibody anti-PPM1G (green) followed by incubation with a fluorochrome-coupled secondary antibody. Nuclei were counterstained using Hoechst33258 (blue). Scale bars represent 10 µm.

4.5   Investigation of AML-specific up-stream regulatory processes of FBXL6

Given that AML cells showed a so-far undescribed second form of FBXL6 (Fig. 11) which was specifically affected by myeloid differentiation (Fig. 14), a crucial part of this project was to unravel the underlying up-stream regulatory mechanisms of FBXL6.

4.5.1   FBXL6 is regulated by protease cleavage at the N-terminus

Based on the results from the ectopic expression of FBXL6 isoform 1 with a C- or N-terminal FLAG-tag in AML cells (Fig. 12), it was hypothesized that FBXL6 is specifically cleaved to produce a C-terminal fragment of 54 kDa. To validate protease cleavage as the

underlying mechanism for the distinct FBXL6 forms, an *in-vitro*-cleavage assay was performed. Since an enrichment of FBXL6-54kDa was observed when leaving the lysates for several hours on ice in previous experiments (data not shown), incubation times of up to 4 hrs on ice and up to 2 hrs at 25°C were chosen to enable potential protease cleavage. Indeed, THP-1 whole-cell extracts displayed a shift from mostly the upper form in lysates without incubation to the predominant appearance of the FBXL6-54kDa within 4 hrs of incubation on ice (Fig. 25a, lanes 1-3). After an incubation period of 2 hrs at 25°C, nearly no upper form was detectable, while an even lower-running third band appeared (Fig. 25a, lane 4). Of note, the standard lysis buffer used here contained a panel of protease inhibitors at commonly used concentrations (aprotinin, leupeptin, soybean trypsin inhibitor, PMSF, TPCK, TLCK; see section 3.1.14), which apparently was not sufficient to inhibit processing of FBXL6. When the inhibitor cocktail was supplemented with the protease inhibitors AEBSF, Bestatin, E-64, and Pepstatin A, the shift in the FBXL6 band pattern was markedly delayed (Fig. 25a, lanes 5-8). To determine which of the additional protease inhibitors was responsible for the delay in FBXL6 cleavage, THP-1 lysates were subjected to an *in-vitro*-cleavage assay with individual addition of the inhibitors. Strikingly, the serine protease inhibitor AEBSF alone was able to fully replicate the effect of the expanded inhibitor cocktail (Fig. 25b, lane 5). Individual addition of the other inhibitors targeting metalloproteases (Bestatin), cysteine proteases (E-64), or aspartic acid proteases (Pepstatin) resulted in the same FBXL6 band pattern as the standard inhibitor cocktail (Fig. 25b). Even though additional protease inhibitors could not completely abolish the processing of FBXL6 *in vitro*, these results solidified protease cleavage as the
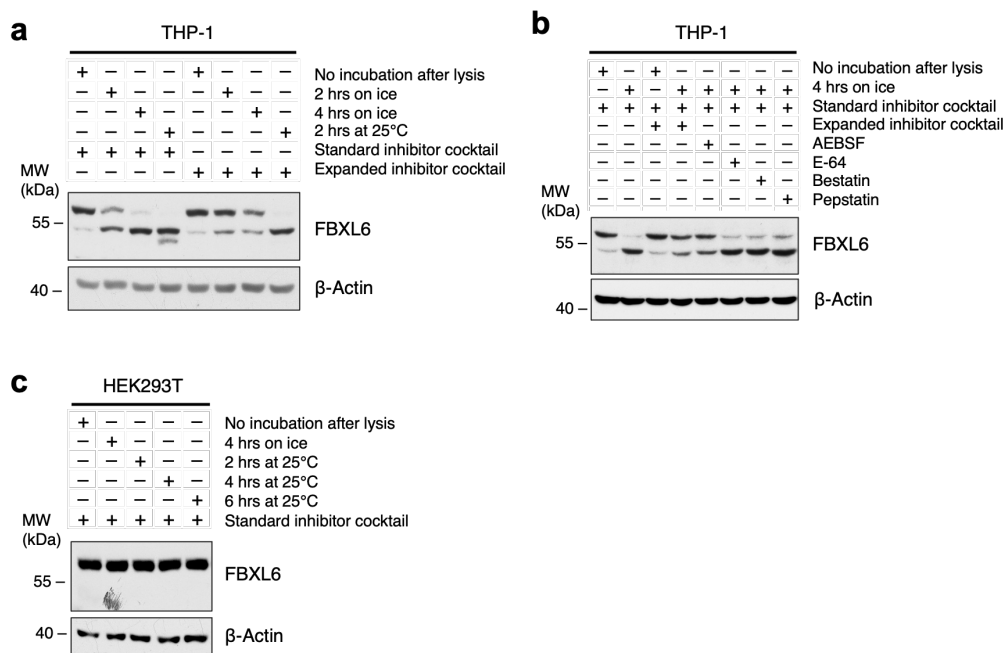
Figure 25 FBXL6 is cleaved by a serine-type protease *in vitro* in AML cell lysates. (a-c) Immunoblot analysis of *in-vitro*-cleavage assays under different conditions. **(a)** *In-vitro*-cleavage assay of THP-1 cell lysates which were incubated for the indicated time points on ice or at 25°C or denatured by addition of Laemmli buffer without incubation after cell lysis. The standard inhibitor cocktail contained (aprotinin, leupeptin, soybean trypsin inhibitor, PMSF, TPCK, TLCK; see section 3.1.14). The expanded inhibitor cocktail consisted of the standard cocktail plus 0.5 mM AEBSF, 20 µM Bestatin, 10 µM E-64, and 20 µM Pepstatin. β-Actin served as a loading control. **(b)** *In-vitro*-cleavage assay of THP-1 cell lysates analogous to (a) with individual addition of the indicated protease inhibitors specific for serine proteases (AEBSF, 0.5 mM), cysteine proteases (E-64, 10 µM), metalloproteases (Bestatin, 20 µM), or aspartic acid proteases (Pepstatin, 20 µM). **(c)** *In-vitro*-cleavage assay of HEK293T cell lysates analogous to (a).

underlying mechanism of the distinct FBXL6 band pattern and pointed toward a protease of the serine-type family to be responsible for FBXL6 cleavage.

Immunoblot analysis of a large panel of cell lines from various cancer entities indicated that the appearance of the FBXL6-54kDa was specific for AML cell lines (Fig 11). To test whether FBXL6 is eventually cleaved *in vitro* in cells that do not readily show FBXL6-54kDa under standard lysis conditions, the *in-vitro*-cleavage assay was conducted in HEK293T cells. Immunoblot analysis revealed, that even after an incubation of 6 hrs at 25°C, lysates from HEK293T showed only one band for FBXL6 at the full-length size of 59 kDa (Fig. 25c). Hence, FBXL6 cleavage might be regulated by AML-specific signals such as post-translational modifications, or executed by an enzyme that is specifically expressed in AML cells.

Aiming to evaluate the proposed cleavage mechanism of FBXL6 by a serine protease in living cells, AML cell lines were treated with AEBSF in culture. First, THP-1 and MV4-11 cells were treated with 100 µM ABSF for up to 6 hrs before cell lysis. Immunoblot analysis revealed that FBXL6 cleavage was efficiently inhibited after 1 hour of treatment before cells went into apoptosis after 3 hrs as marked by caspase-3 cleavage (Fig. 26a). In a similar experiment, MV4-11 cells were treated with different concentrations of AEBSF for 3 hrs. Immunoblot analysis showed that a concentration of 50 µM AEBSF was sufficient to completely inhibit FBXL6 cleavage in living cells (Fig. 26b).

Together, these results indicate that FBXL6 is processed by protease-cleavage in AML cell lysates and in living AML cells, which can be inhibited in a dose- and time-dependent manner by the serine protease-specific inhibitor AEBSF.
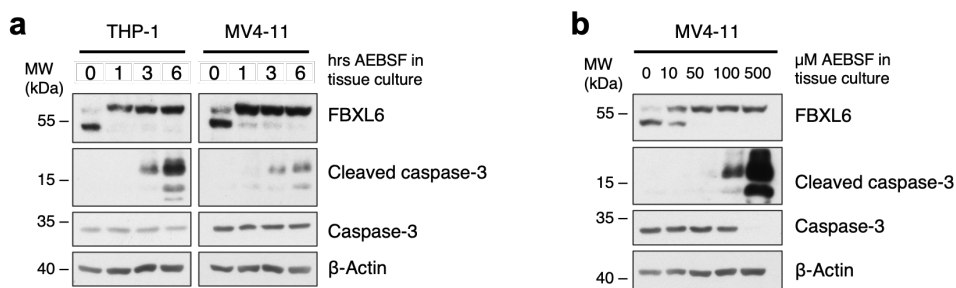
Figure 26 AEBSF inhibits FBXL6 cleavage in a dose- and time-dependent manner in living cells. (a) Immunoblot analysis of THP-1 and MV4-11 cells treated with 100 µM AEBSF before harvesting at the indicated time points and subjecting to standard cell lysis. **(b)** Immunoblot analysis after cell lysis of MV4-11 cells treated with AEBSF at the indicated concentrations for 3 hrs. (a-b) β-Actin served as a loading control.

4.5.2 FBXL6 is cleaved between Leu47 and Ser50

In order to identify the protease-cleavage site within the protein sequence of FBXL6, a dual mass spectrometry-based experiment combining top-down and bottom-up proteomics was set up in collaboration with the proteomics core facility of the Max Planck Institute (MPI) of Biochemistry in Martinsried, Germany. C-terminally FLAG-tagged FBXL6 versus EV control was overexpressed in THP-1 cells and purified via FLAG-IP for two different mass spectrometric analyses. For the bottom-up proteomics approach, the two bands corresponding to FBXL6 were cut out from a Coomassie-stained SDS-gel and subjected to trypsin-digest for differential identification of peptides produced from FBXL6-59kDa versus FBXL6-54kDa. For the additional top-down proteomics analysis, the purified proteins were

left intact and directly injected into the mass spectrometer for determining the total protein mass of full-length and cleaved FBXL6 (see schematic in Fig. 27).
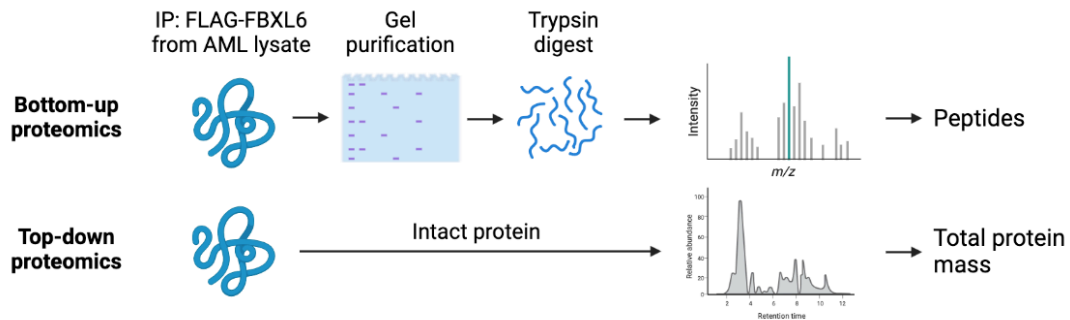
Figure 27 Schematic of the dual mass spectrometry-based approach to identify the cleavage site of FBXL6. FLAG-FBXL6 versus empty vector control was purified via immunoprecipitation (IP) from THP-1 cells and divided into two samples. One sample was separated via SDS-PAGE and stained with Coomassie. Bands corresponding to FBXL6 were isolated and subjected to trypsin digest for peptide identification (bottom-up proteomics). The remaining sample was used for direct injection into the mass spectrometer to determine the total protein mass of cleaved and full-length FBXL6 (top-down proteomics).

For the differential peptide identification, 20% of the purified proteins were separated by SDS-PAGE and visualized with Coomassie-staining for isolating FBXL6 (Fig. 28a). The two corresponding bands at approximately 59 kDa and 54 kDa were cut-out and sent to Martinsried for further processing. Mass spectrometric analysis by Dr. Barbara Steigenberger revealed that the higher-running band produced peptides within the first 58 amino acids of the FBXL6 sequence, while these were missing in the lower-running band (Fig. 28b). Peptides from 70 to 455 amino acids were detected in comparable amounts from both upper-and lower-running bands, indicating that FBXL6 was cleaved within the first 69 amino acids of the protein sequence.

For the total protein mass analysis, the remaining 80% of eluted proteins were concentrated using centrifugal protein concentrators with a molecular weight cut-off of 10 kDa, enabling a sufficient target protein concentration while reducing the amount of FLAG-peptide used for elution. For quality control, equivalent amounts of the initial eluate, the concentrator flow through, and the final eluate were separated by SDS-PAGE and subjected to silver staining (Fig. 28c). After confirming sufficient amounts of FBXL6, final eluates were denatured using 1% TFA and sent to Martinsried for analysis by Victoria Sanchez. To extract the protein masses corresponding to FBXL6, first, all values present in the EV control were omitted. In the second step, a fragment search was performed where the detected protein masses were compared to *in-silico* generated C-terminal fragments of FBXL6. Strikingly, one of the detected protein masses showed a deviation of only 0.03 Da compared to the calculated molecular weight of FBXL6 lacking the first 47 amino acids, providing a strong indication for cleavage of FBXL6 at this position (Fig. 28d). Additional values with only minor deviations from the calculated fragment weight pointed toward the cleavage of FBXL6 between the amino acids Leu47 and Ser50, while neglecting other post-translational modifications to contribute to the molecular weight of FBXL6.

Taken together, the mass spectrometric data from top-down and bottom-up proteomics approaches solidified the hypothesis of FBXL6 cleavage in the N-terminal region, supposedly between the amino acids Leu47 and Ser50.
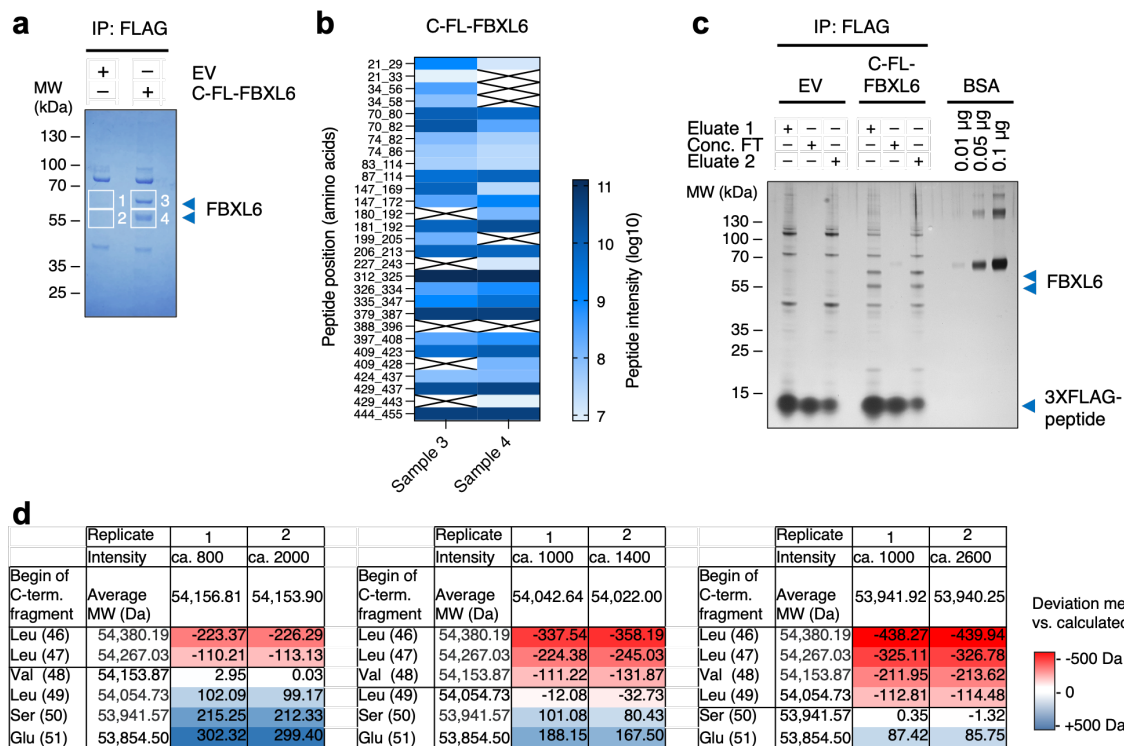
Figure 28 Mass spectrometric analysis identifies the FBXL6 cleavage site between Leu47 and Ser50. (a) Coomassie staining of eluted proteins using 3XFLAG-peptide after FLAG-IP from THP-1 cell lysates (standard conditions) expressing empty vector control (EV) or C-terminally FLAG-tagged FBXL6 (C-FL-FBXL6) after separation via SDS-PAGE. Rectangles mark the isolated gel slices (1-4) for bottom-up proteomics. **(b)** Peptide intensities measured by mass spectrometry from samples 3 and 4 in (a). **(c)** Silver staining of the remaining eluates from (a) which were subjected to centrifugal protein concentration for top-down proteomics. Equivalent amounts of original eluate (Eluate 1), concentrator flow through (Conc. FT), and concentrated eluate (Eluate 2) were loaded for quality control. Bovine serum albumin (BSA) served as a measure for purified protein amount. **(d)** Comparison of total protein masses determined by mass spectrometry with calculated molecular weights based on the FBXL6 amino acid sequence. Values are derived from two biological replicates. [Data for b generated by Dr. B. Steigenberger. Data for d provided by V. Sanchez.]

Table (d):

	Replicate	1	2
	Intensity	ca. 800	ca. 2000
Begin of C-term. fragment	Average MW (Da)	54,156.81	54,153.90
Leu (46)	54,380.19	-223.37	-226.29
Leu (47)	54,267.03	-110.21	-113.13
Val (48)	54,153.87	2.95	0.03
Leu (49)	54,054.73	102.09	99.17
Ser (50)	53,941.57	215.25	212.33
Glu (51)	53,854.50	302.32	299.40

	Replicate	1	2
	Intensity	ca. 1000	ca. 1400
Begin of C-term. fragment	Average MW (Da)	54,042.64	54,022.00
Leu (46)	54,380.19	-337.54	-358.19
Leu (47)	54,267.03	-224.38	-245.03
Val (48)	54,153.87	-111.22	-131.87
Leu (49)	54,054.73	-12.08	-32.73
Ser (50)	53,941.57	101.08	80.43
Glu (51)	53,854.50	188.15	167.50

	Replicate	1	2
	Intensity	ca. 1000	ca. 2600
Begin of C-term. fragment	Average MW (Da)	53,941.92	53,940.25
Leu (46)	54,380.19	-438.27	-439.94
Leu (47)	54,267.03	-325.11	-326.78
Val (48)	54,153.87	-211.95	-213.62
Leu (49)	54,054.73	-112.81	-114.48
Ser (50)	53,941.57	0.35	-1.32
Glu (51)	53,854.50	87.42	85.75

Deviation measured vs. calculated MW: -500 Da / 0 / +500 Da

Since the protein structure of FBXL6 has not been solved to this date, the artificial intelligence-based webtool Alphafold was deployed to investigate the predicted 3D protein structure of FBXL6 to gain insights whether cleavage of FBXL6 has a biological relevance. Based on the amino acid sequence of the query protein and empirically solved 3D structures of related proteins, Alphafold generates 3D models at amino acid accuracy (Varadi et al., 2022). The predicted 3D structure of full-length FBXL6 showed a large C-terminal horseshoe-like domain, which is often found in members of the FBXL family and described as a substrate-binding domain (Mason & Laman, 2020; Schulman et al., 2000) (Fig. 29a). The F-box fold was modeled to reside orthogonal to the C-terminal domain. The remaining N-terminal part was forming a loop with unstructured regions and a structured region inside the horseshoe-like domain. Interestingly, the cleavage site identified by mass spectrometry resided within this structured N-terminal part, while the protein domains responsible for SCF complex formation and substrate binding are left intact. Even though the model confidence for the relative position of the N-terminal part of FBXL6 was very low, the 3D model hinted at

a potential influence of FBXL6 cleavage on either substrate binding or SCF complex formation by steric hindrance (Fig. 29b).
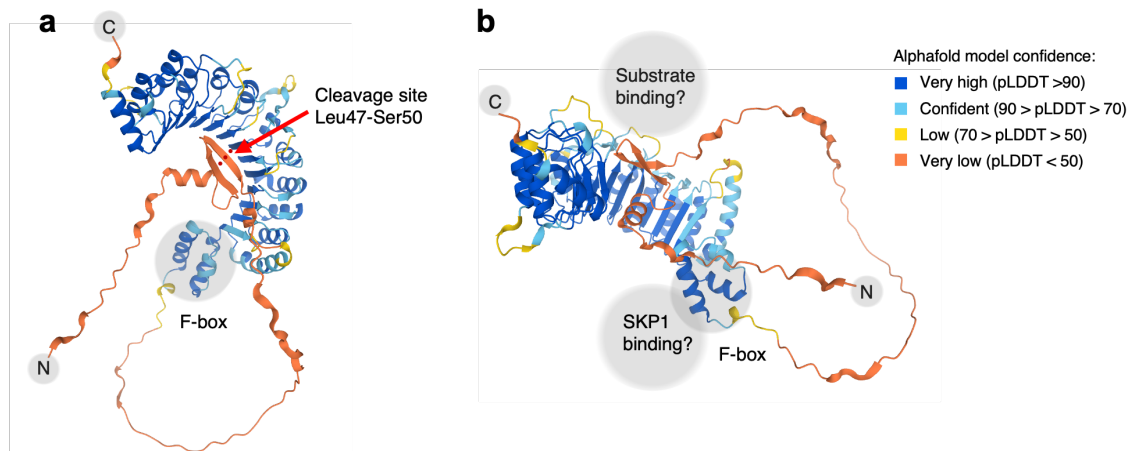
Figure 29 3D protein structure for FBXL6 generated by Alphafold. (a) FBXL6 three-dimensional (3D) protein structure predicted by Alphafold (Sherman et al., 2022). Marked in grey are C-terminus, N-terminus, and F-box domain of FBXL6. The red arrow indicates the identified protease-cleavage site around Leu47-Ser50 in the FBXL6 sequence (Fig. 28). **(b)** Rotated view of the FBXL6 structure shown in (a) with an indication of the supposed binding sites of the SCF complex component SKP1 and the ubiquitylation substrate. The model confidence is visualized in different colors depicting the per residue confidence score (pLDDT) that ranges vom 0 (lowest confidence) to 100 (highest confidence).

4.5.3 Identification of Cathepsin G as the FBXL6-directed protease

Aiming to identify the protease responsible for FBXL6 cleavage, the interactome screens from HL-60 and MV4-11 cells were re-analyzed, focusing on interaction partners harboring proteolytic function. The lists of potential interactors were subjected to functional annotation using the DAVID database (Sherman et al., 2022), and proteins classified by GO terms containing "protease" or "peptidase" were extracted. This approach identified three proteases in the HL-60 interactome and seven for MV4-11, while cathepsin G (CatG, gene name CTSG) was the only protease enriched in both screens (Fig. 30a-b). To narrow down the list of potential FBXL6-specific proteases, the identified cleavage site around Leu47-Ser50 (Fig. 28) was searched in the peptidase database MEROPS (Rawlings et al., 2014) for enzymes with cleavage activity toward a similar motif. The query yielded 32 human proteases, which could be reduced to ten candidates after filtering for serine-type proteases (Fig. 30c, Fig. 25). Strikingly, two out of four major serine-proteases expressed in myeloid cells were found in this list of candidates, namely neutrophil elastase (NE, gene name ELANE) and CatG.

In order to test, whether CatG or NE have cleavage activity toward FBXL6, an *in-vitro*-cleavage assay with specific protease-inhibitors was performed. THP-1 cells were lysed in standard lysis buffer containing the standard protease inhibitors plus increasing amounts of either CatG-specific inhibitor or NE-specific inhibitor. Immunoblot analysis revealed that addition of NE inhibitor had no effect on FBXL6 cleavage even at the highest concentration of 250 µM, while the CatG-specific inhibitor nearly abolished FBXL6 processing already at 50 µM (Fig. 30d).
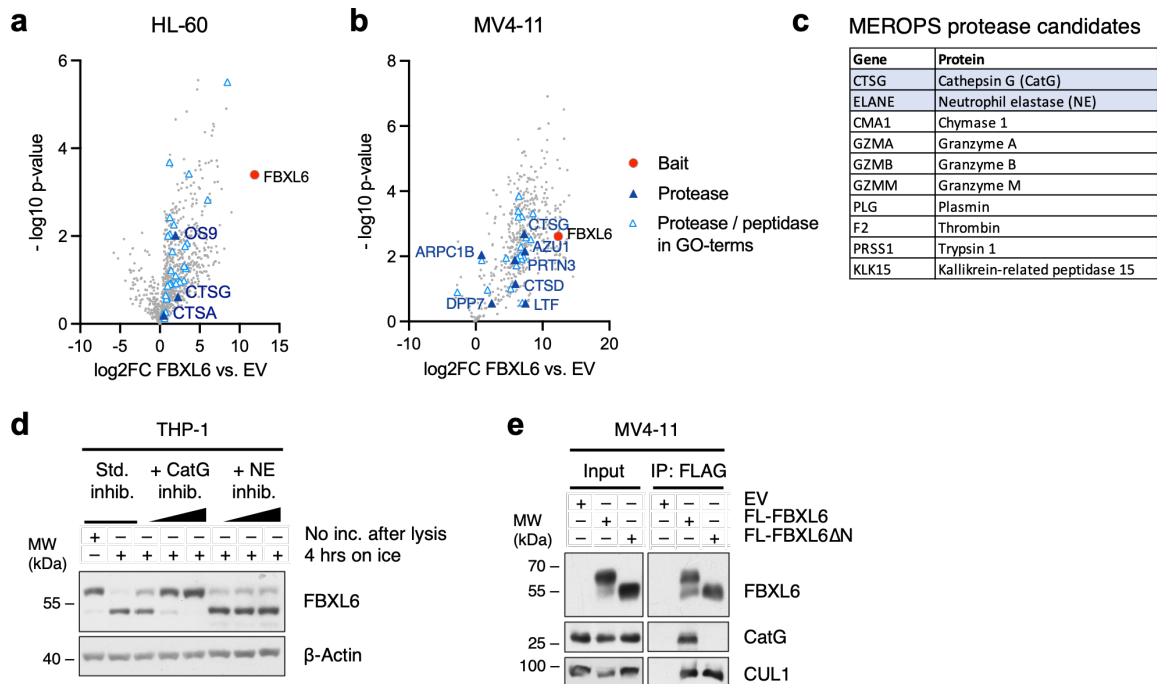
Figure 30 Identification of CatG as the FBXL6-directed protease. (a-b) Volcano plots of mass spectrometry (MS)-based interactome analysis of FBXL6 purified from (a) HL-60 (described in section 2.3.3) and (b) MV4-11 cells (described in section 4.4.1) after functional annotation of binding partners using DAVID webtool (Sherman et al., 2022). Highlighted are proteins classified by GO (gene ontology)-terms containing "protease" or "peptidase". **(c)** Results from the MEROPS database (Rawlings et al., 2014) search for enzymes with cleavage activity toward a similar sequence motif as identified for FBXL6 (Fig 28). The output of 32 human enzymes was filtered for proteases of the serine-type family. Proteases that are known to be expressed in myeloid cells are marked in blue. **(d)** *In-vitro*-cleavage assay of cell lysates from THP-1 cells using specific protease-inhibitors for Cathepsin G (CatG) and neutrophil elastase (NE) at increasing concentrations (2.5 μM, 25 μM or 250 μM) in addition to the standard inhibitor cocktail (Std. inhib.). β-Actin served as a loading control. Inc, incubation. **(e)** FLAG-IP of full-length FBXL6 and FBXL6ΔN, a fragment mutant starting at Val48 representing the cleaved form of FBXL6, from MV4-11 cells with subsequent immunoblot analysis. CUL1 served as a loading control. EV, empty vector. [MS Data for a provided by J. Krumm, MS data for b provided by Dr. P. Giansanti]

For validation of the interaction between FBXL6 and CatG found in the interactome screens, a semi-endogenous immunoprecipitation was conducted. Next to EV control and FL-FBXL6, the C-terminal fragment mutant of FBXL6 (FBXL6ΔN), which started at Val48 based on the identified cleavage site (Fig. 28), was overexpressed in MV4-11 cells. Assuming that a protease dissociates from its substrate after cleavage is completed, it would be expected that only the intact protein binds to CatG. Immunoblot analysis of whole-cell extracts confirmed a similar running height of the FL-FBXL6ΔN fragment mutant with the cleaved form generated from FL-FBXL6 (Fig. 30e). The subsequent FLAG-IP showed binding of CatG to full-length FBXL6 only, while FBXL6ΔN failed to pull down the protease (Fig. 30e), thus solidifying CatG to be the FBXL6-directed protease.

Since FBXL6 cleavage was found specifically in a subset of AML cell lines and not in cells from other cancer entities, samples from Fig. 11 were probed with anti-CatG antibody to evaluate whether CatG protein levels correlate with FBXL6 cleavage. Across all tested cell lines, CatG protein expression was clearly associated with the appearance of cleaved FBXL6 (Fig. 31a-b). Furthermore, the FBXL6 band pattern was remarkably altered upon myeloid differentiation induced by TPA or ATRA (Fig. 14). To test whether the observed effect was caused by CatG cleavage, immunoblots from Fig. 14 were analyzed with anti-CatG antibody.

Indeed, CatG protein levels were massively decreased upon forced myeloid differentiation (Fig. 31c-d), solidifying the hypothesis of FBXL6 cleavage by CatG .

Taken together, these results identify the serine-protease CatG to specifically cleave FBXL6 in AML cells.
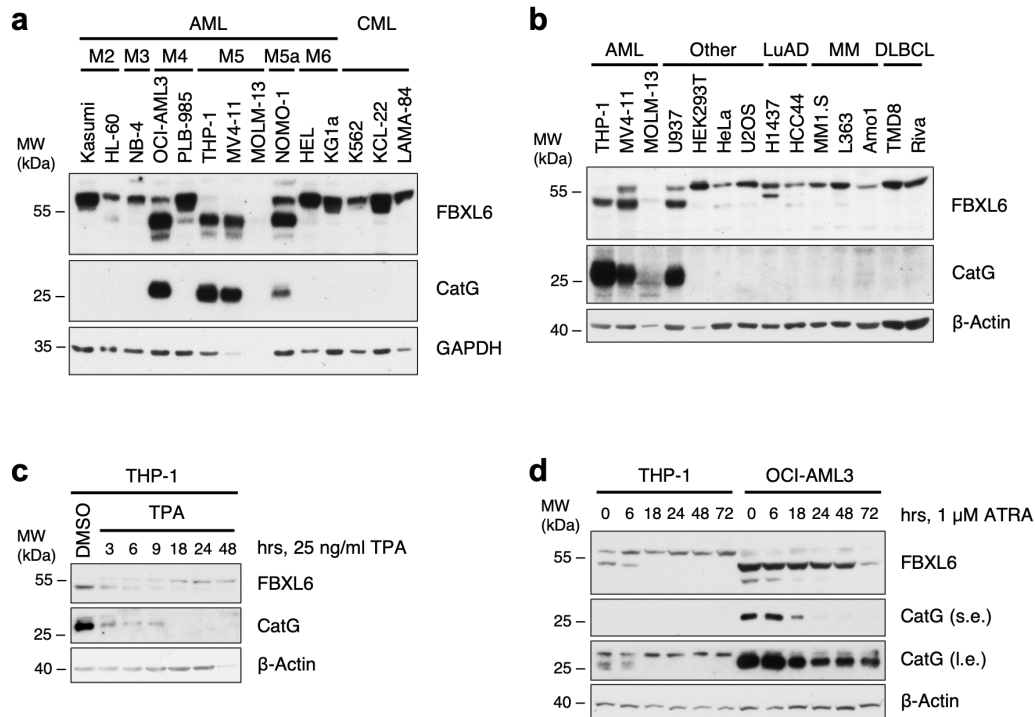
Figure 31 CatG protein levels correlate with FBXL6 cleavage. (a-b) Immunoblot analysis of whole-cell extracts from various cell lines prepared under standard conditions (samples from Fig. 11) probed with Cathepsin G antibody. **(c-d)** Immunoblot analysis of AML cell lysates treated with TPA or ATRA for forced myeloid differentiation prepared under standard conditions (samples from Fig. 14) probed with Cathepsin G antibody. S.e., short exposure; l.e., long exposure. β-Actin served as a loading control.

4.5.4 Overexpression of FBXL6 does not affect TPA-induced differentiation

Since the shift in FBXL6 band pattern upon myeloid differentiation could be attributed to protease cleavage by CatG, the biological relevance thereof should be investigated. To test, whether acute overexpression of full-length FBXL6 or FBXL6ΔN, which supposedly mimics the function of cleaved FBXL6, could counteract TPA-induced myeloid differentiation, a doxycycline-inducible system was employed in MV4-11 cells. After lentiviral transduction with Flag-tagged FBXL6, FL-FBXL6ΔN or EV, cells were selected with puromycin to eliminate non-transduced cells. For acute overexpression of FBXL6, cells were treated with DMSO (-Doxy) or with doxycycline (+Doxy) for 24 hrs before inducing differentiation with TPA for 24 hrs. Immunoblot analysis of cell lysates confirmed successful overexpression and showed a similar shift in the FBXL6 band pattern for overexpressed full-length FBXL6 (Fig. a). Of note, a marginal promotor leakiness was detected in the -Doxy controls, which was likely due to the very high expression levels achieved by lentiviral transduction. To avoid misinterpretation of the results due to promotor leakiness, -Doxy controls were included throughout the experiment. CD11b surface staining with subsequent flow cytometric analysis revealed that overexpression of neither full-length FBXL6 nor FBXL6ΔN affected TPA-induced myeloid differentiation (Fig. 32b). Thus, enrichment of full-length FBXL6 upon TPA treatment was

considered to be a bystander effect of CatG protein loss during myeloid differentiation (Fig. 31).
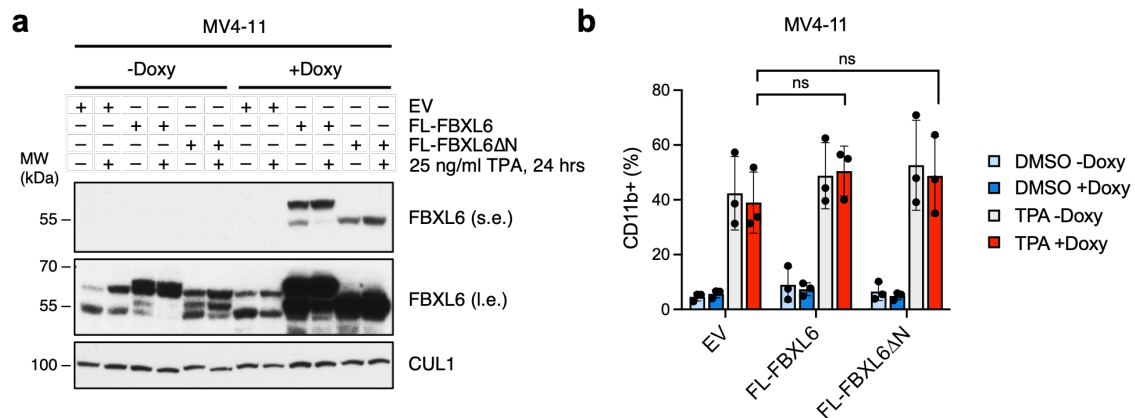
Figure 32 Overexpression of full-length FBXL6 or FBXL6ΔN does not affect TPA-induced differentiation. (a) Immunoblot analysis of MV4-11 cells transduced with doxycycline-inducible expression constructs for FLAG-tagged full-length (FL-FBXL6) or fragment mutant FBXL6 representing the cleaved form (FL-FBXL6ΔN) or empty vector control (EV). Cells were treated for 24 hrs with DMSO (-Doxy) or with 1 μg/ml doxycycline (+Doxy) to induce expression before the addition of 25 ng/ml TPA or vehicle control (DMSO) for 24 hrs. Whole-cell extracts were prepared under standard conditions. CUL1 served as a loading control. S.e., short exposure; l.e., long exposure. **(b)** Quantification of cells in (a) positive for CD11b surface staining in flow cytometric analysis. ns, not significant by Student's t-test.

4.5.5 Cleavage of FBXL6 is an artifact during cell lysis

After identifying CatG as the responsible protease for FBXL6 cleavage in AML cells, thorough literature research on CatG was performed. Surprisingly, several publications reported on excessive proteolytic activity of CatG in standard lysis buffers which led to major pitfalls in interpreting immunoblot data generated from cells with high expression of CatG and other myeloid serine-proteases (Franzoso et al., 1994; Schoenherr et al., 2019; Schuster et al., 2007). For instance, STAT5 was initially described as a proteolytic substrate of CatG with potential relevance in myeloid differentiation until Schuster et al. proved that cleaved STAT5 is absent in living cells but represents an artifact during high salt cell lysis (Schuster et al., 2007). Since cleaved STAT5 could not be detected in lysates prepared under denaturing conditions by boiling the cells in an SDS-containing buffer, Schuster et al. concluded that CatG does not cleave STAT5 in living cells.

To evaluate whether FBXL6 cleavage is naturally occurring in living cells or instead a cell lysis artifact, different lysis conditions were applied to MV4-11 cell pellets of equal size. Next to the standard protocol for cell lysis applied for all previous cell lysates within this project, cells were lysed under denaturing conditions by boiling in SDS-containing buffers. According to Schuster et al., a buffer containing 2% SDS was used as well as lysis and boiling in 1X or 2X Laemmli buffer according to Schoenherr et al., who described a similar phenomenon for CatG-activity induced by depletion of RUNX1-ETO (Schoenherr et al. 2019). Immunoblot analysis showed a substantially decreased amount of cleaved FBXL6 under denaturing lysis compared to the standard lysis buffer (Fig. 33a). Notably, a small portion of cleaved FBXL6 was still detectable in all three denaturing conditions. To exclude any CatG activity before protein denaturation was completed, the experiment was repeated with the standard lysis buffer supplemented with excessive amounts of the CatG-specific inhibitor. Additionally, the protocol for the denaturing lysis using SDS buffer was improved by

immediate resuspension of fresh cell pellets without storage on ice in between. This time, both MV4-11 and THP-1 lysates failed to show any cleaved species of FBXL6 under standard lysis with up to 500 µM CatG inhibitor or denaturing lysis with SDS buffer (Fig. 33b). Therefore, it had to be concluded that cleavage of FBXL6 is a mere artifact during standard cell lysis and lacks any biological relevance in AML cells.
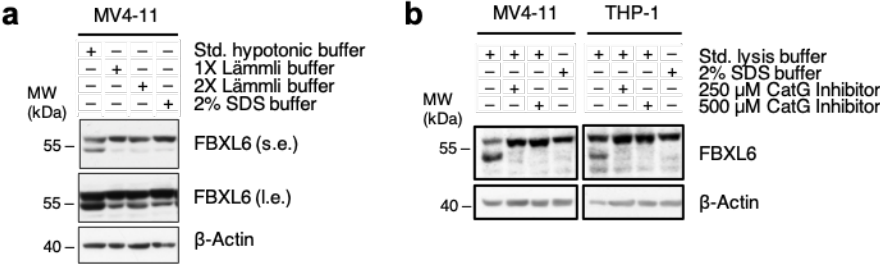
Figure 33 Cleavage of FBXL6 is an artifact of cell lysis. (a) Immunoblot analysis of lysates prepared under standard (Std. lysis buffer) or denaturing conditions (Laemmli and SDS buffers) from MV4-11 pellets of equal size. 1X Laemmli buffer contained 2% SDS, 2X Laemmli buffer contained 4% SDS. S.e., short exposure; l.e., long exposure. **(b)** Immunoblot analysis of lysates from MV4-11 and THP-1 cells prepared analogous to (a) with addition of excessive amounts of CatG-specific inhibitor to the standard lysis buffer. (a-b) β-Actin served as a loading control.

5 Discussion

Acute myeloid leukemia (AML) is an aggressive malignancy of the myeloid system with an extremely poor prognosis resulting from failure to achieve complete remission and a high relapse rate (Park et al., 2020). Even though extensive research on the genomic level in the last decades has led to sophisticated risk stratification strategies and the development of novel agents including FLT3 and IDH inhibitors, AML treatment still largely relies on chemotherapy and hematopoietic stem cell transplantation (Burnett & Stone, 2020; Rowe, 2019). Thus, the identification of new actionable vulnerabilities is critically needed. Investigating post-translational modifications (PTM) such as ubiquitylation holds great promise to provide new target structures in AML, as recent reports suggest. Next to the identification of the SCF-type ubiquitin ligase FBXL2 as a tumor suppressor in AML (B. B. Chen et al., 2012), the NEDD8 inhibitor pevonedistat showed promising results in clinical trials when combined with azacytidine in AML patients (Adès et al., 2022). However, systematic discovery campaigns for vulnerabilities in AML among E3 ubiquitin ligases such as the family of F-box proteins were still missing.

Against this background, Dr. David Brockelt performed a CRISPR/Cas9-based screen in AML cell lines with libraries targeting all SCF-type ubiquitin ligases in the group of Prof. Dr. Florian Bassermann. This approach identified the barely studied F-box protein FBXL6 as a promising new dependency in AML (Fig. 4). Preliminary data pointed toward FBXL6 being a functional substrate-recognition adaptor of an E3 ubiquitin ligase with nuclear localization, as immunoprecipitation assays and chromatin fractionations showed (Fig. 5-6). The systematic characterization of FBXL6 as a new vulnerability in AML and the underlying molecular mechanisms including up- and down-stream regulatory pathways, was still pending when the project was handed over to become the main topic of this thesis.

5.1 FBXL6 as a novel vulnerability in AML

5.1.1 Identification of FBXL6 by CRISPR/Cas9-based essentiality screening

CRISPR/Cas9-based gene essentiality screens on a whole-genome scale were first applied in 2014 in leukemia cells and have since then been widely used across various cancer entities (DepMap Consortium, 2018; Shalem et al., 2014; T. Wang et al., 2014). Due to the competition-based principle, large-scale approaches with sgRNA libraries targeting the entire genome often reveal only the most central oncogenes that have by now been extensively studied, while masking many other, eventually less prominent dependencies. For investigating a distinct pathway or a certain group of genes, a focused library approach can overcome this limitation, as has already been shown for epigenetic regulators or microRNAs (Henser-Brownhill et al., 2017; Kurata & Lin, 2018). Recent reports showing a link between SCF-type ubiquitin ligases and AML provided an additional rationale for the custom design of a sgRNA library focusing on all human F-box proteins instead of using a commercially available genome-wide library. Notably, the CRISPR/Cas9 screen by Dr. D. Brockelt recapitulated strong dependencies within the group of F-box protein genes seen in genome-wide screens in AML such as Cyclin F (FBXO1) and FBXW11 (Erb et al., 2017; T. Wang et al., 2017), confirming the validity of the experiment. At the same time, FBXL6 was one of the strongest hits in the SCF-focused screen (Fig. 4), while the whole-genome screens showed a

moderate dependency that would not stand out beside other more essential hits. Still, in both large-scale dropout screens in AML, FBXL6 ranked among the top 20 of all 72 F-box protein genes, reflecting a robust dropout phenotype of FBXL6 depletion in pooled CRISPR/Cas9 screens.

5.1.2 FBXL6 in primary AML patient samples and public datasets

Analysis of over 700 primary AML patient samples in the MLL cohort revealed a vast upregulation of FBXL6 mRNA compared to healthy bone marrow which was one of the highest upregulated hits among over 1,000 analyzed ubiquitin-related genes (Fig. 7). Since FBXL6 expression was high across all AML subtypes, FBXL6 activity in AML does presumably not depend on any specific oncogenic driver(s) or the activation of particular signaling pathways. Systematic analysis of the MLL cohort and two additional datasets (TCGA and BeatAML2.0) consistently revealed a slightly decreased overall survival in the FBXL6 high versus low group, even though none of the observed differences were huge or significant. Furthermore, high FBXL6 expression significantly correlated with adverse prognosis according to ELN stratification and further characteristics which can be associated with poorer outcome such as FLT3 or NPM1 mutations (Fig. 7-8).

The pro-tumorigenic role of FBXL6 in AML was undermined by the analysis of expression data from various cancer cell lines from DepMap, where FBXL6 mRNA levels were second highest in the myeloid lineage compared to the other 23 lineages, and highly increased when compared to non-cancerous fibroblasts (Fig. 10). Since most of the analyzed cell lines showed highly elevated FBXL6 expression compared to non-cancer cells, an oncogenic role of FBXL6 in different cancer entities can be assumed. This hypothesis was strengthened by analysis of the essentiality screens from DepMap, where a total of 74 cell lines from 21 entities showed a perturbation effect upon FBXL6 deletion below the threshold, while none of the non-cancer controls scored (Fig. 10). Indeed, very recent publications demonstrated the tumor-promoting role of FBXL6 in different solid tumors including hepatocellular carcinoma, gastric carcinoma, and renal cell carcinoma (Li et al., 2021; Meng et al., 2023; Shi et al., 2020; Y. Yu et al., 2022). Since solid tumors differ strongly in their pathogenic mechanisms and deregulated pathways from hematologic malignancies, the mechanism of action of FBXL6 may be completely different in AML than in the described types of carcinomas. Even among solid tumors, two contrasting roles have been observed for FBXL6. While in hepatocellular carcinoma FBXL6 confers K63-linked ubiquitylation toward HSP90AA1 for protein stabilization, phosphorylated p53 is targeted for proteasomal degradation by K48 polyubiquitylation by FBXL6 in colorectal cancer (Li et al., 2021; Shi et al., 2020).

Collectively, the analyses of mRNA expression in primary patient samples and cancer cell lines strongly suggest a role of FBXL6 as a novel oncogene in AML. However, a similar analysis on the protein level would be even more desirable since ubiquitin ligases are known to be regulated on the post-translational level. In addition to the activation of SCF-type ligases by neddylation of the central cullin scaffold, F-box proteins are commonly regulated by proteasomal degradation through (auto-)ubiquitylation (Schmidt et al., 2009; Wirbelauer et al., 2000; Zhou & Howley, 1998). Therefore, large proteomics datasets from primary patient samples and corresponding healthy tissue would be of high interest for the identification of novel vulnerabilities in AML and other types of cancer. Efforts in this direction are already the

subject of current research, as seen in a very recent publication on the proteogenomic subtypes of AML (Jayavelu et al., 2022). Unfortunately, FBXL6 has not been detected in any of the primary AML patient samples or healthy bone marrow controls, reflecting one of the major challenges of current proteomic approaches: limited sensitivity. As the methodology on the level of laboratory work and computational data analysis is currently rapidly improved, even more conclusive datasets will certainly be generated in the near future (Rosenberger et al., 2023; The et al., 2022).

5.1.3 FBXL6 in pre-clinical *in-vitro* and *in-vivo* AML models

Further evidence for FBXL6 exerting a pro-tumorigenic role in AML was generated in pre-clinical *in-vitro* and *in-vivo* models. Competition assays in AML cell lines showed a marked growth disadvantage of FBXL6-depleted cells compared to control cells, thus confirming the results of the CRISPR/Cas9 screen (Fig. 4). Given that the effect was present in MOLM-13, OCI-AML3, and MV4-11 cells, which harbor different genetic aberrations, this finding further supports the hypothesis that FBXL6 essentiality is independent of a specific genetic background. A consistent decrease in viable cell numbers measured by cell counting and MTS assay suggested a reduction in cell proliferation capacity rather than a metabolic defect (Fig. 15). FBXL6-depleted cells did not show more cell death, arrest in a specific cell cycle phase, or increased myeloid differentiation, thus strengthening the assumption of a slowed-down proliferation rate (Fig. 16). Another possible approach to unravel the cellular consequences of FBXL6 depletion in AML cells would be to perform transcriptomic or proteomic analyses of MOLM-13 cells transduced with sgFBXL6 versus sgCtrl. Considering the timeframe in which anti-proliferative effects were observed for FBXL6 depletion, it would be of high interest to harvest the samples between day 3 and day 6 after infection, ideally in a time-resolved manner. Applying RNA-Seq (RNA sequencing) for gene expression analysis and mass spectrometry for proteomic analysis with a very high detection sensitivity would provide conclusive data in an unbiased approach to identify deregulated pathways by bioinformatic enrichment analysis.

Even though the mechanistic determinants for the FBXL6-dependency of AML cells are still unclear, the repeatedly seen effects in cell line-based assays prompted the question of whether FBXL6 is also essential *in vivo*. A competition-based patient-derived xenograft (PDX) mouse model was set up with two different sgRNAs targeting FBXL6 versus non-targeting control. sgFBXL6_5 markedly impaired PDX leukemia at both early and late time points (Fig. 18). The earlier timepoint showed a more pronounced effect, which reflected the observations from *in-vitro* proliferation and competition assays and suggested a defect of FBXL6-depleted cells primarily with respect to homing into the bone marrow niche next to impaired proliferation of PDX cells in mice. Another reason for a stronger tumor suppressive effect of FBXL6 depletion at early time points compared to later time points might be cellular compensatory mechanisms like the upregulation of genes/proteins that are able to substitute for the function of FBXL6. Since cancer cells are characterized by high genomic instability, they are capable of adapting expression patterns quickly (Hanahan & Weinberg, 2000). Unexpectedly, the second sgRNA did not recapitulate these promising results, even though both sgRNA constructs showed comparable behavior in the *in-vitro* validation experiments (Fig. 17). A possible explanation for the discrepancies between the two sgRNA constructs might be found in CRIPSR/Cas9-specific mechanisms, such as the correct repair of the Cas9-induced DNA double-strand break. Since the FBXL6 knockout was not confirmed in the

murine bone marrow samples, only sgFBXL6_5 might have caused a knockout, whereas sgFBXL6_6 might have failed to deplete FBXL6. To robustly show that FBXL6 has anti-proliferative effects *in vivo*, additional experiments will be necessary. First, the PDX model should be repeated to generate biological replicates using both sgRNA constructs and a third independent sgRNA. Choosing additional PDX samples with high FBXL6 expression will help to solidify the obtained results, as variability among PDX samples derived from AML patients with different genetic aberrations has been shown before by the group of Prof. Dr. Irmela Jeremias for other vulnerabilities in AML (Bahrami et al., 2023). Next to repeating the PDX mouse model, it would be highly interesting to apply a syngeneic transplantation-based AML mouse model, where murine bone marrow cells are transduced with AML drivers with or without additional FBXL6 overexpression prior to transplantation into recipient mice. Such models are well established for the AML-driving aberrations FLT3-ITD, MLL-ENL, AML-ETO, HOXA9, and MEIS1 (Cozzio et al., 2003; Kelly et al., 2002; Mohr et al., 2017; Yan et al., 2004). Since the FLT3-ITD-positive cell line MOLM-13 showed highest dependency on FBXL6 expression in this study, and FBXL6 mRNA expression slightly correlated with FLT3 mutation counts in AML patient samples, initial experiments might be performed in the FLT3-ITD transplantation-based mouse model (Höckendorf et al., 2016; Kelly et al., 2002). Comparing FLT3-ITD-expressing bone marrow with and without forced expression of FBXL6 regarding the onset of leukemia by sequential blood analyses as well as with regard to survival might help to unambiguously demonstrate the oncogenic nature of FBXL6.

5.2 PPM1G is a ubiquitylation substrate of FBXL6

Ubiquitin ligases exert their biological function by modifying substrate proteins on a post-translational level. The pivotal role of F-box proteins as substrate recognition adaptors of multi-subunit ligases highlights the importance of substrate protein identification for FBXL6 in AML.

5.2.1 Multi-angled screening reveals PPM1G as a substrate of FBXL6

Combination and cross-validation of three interactome screens and one ubiquitylation-specific functional screen identified 24 potential substrates of FBXL6 (Fig. 20). Among these substrate candidates, many proteins were involved in key essential cellular pathways including DNA damage recognition and translation initiation. The phenotypic observations in AML cells upon FBXL6 depletion argued for prioritizing substrate candidates outside these common essential clusters. The protein phosphatase PPM1G has been described as a tumor suppressor that regulates different proteins involved in cell survival, cell growth, and DNA damage response (Kamada et al., 2020), and was found as one of the most significant cross-validation hits from the substrate screens (Fig. 20). In immunoprecipitation experiments, the interaction between FBXL6 and PPM1G could be confirmed, while other members of the FBXL-type family of ligases failed to bind PPM1G or showed a neglectable interaction compared to FBXL6 (Fig. 21). The total protein abundance of PPM1G was unchanged upon FBXL6 modulation and PPM1G was not destabilized by FBXL6 overexpression in a cycloheximide time course, which strongly suggested a non-degradative effect of FBXL6 on PPM1G (Fig. 21-22). Importantly, only overexpression of FBXL6 caused an increase in PPM1G-ubiquitylation which was found to be K63-linked polyubiquitylation in *in-vivo-ubiquitylation* assays (Fig. 23).

K63-type ubiquitylation represents the second most common form of polyubiquitylation and is known to have effects on protein interactions, protein activity, and subcellular localization (Komander & Rape, 2012). PPM1G is described to reside predominantly in the nucleus, while re-localization to the cytoplasm was observed under certain conditions such as binding to a PP2A regulatory subunit (Kumar et al., 2019; Liu et al., 2013). This shuttling of PPM1G between nucleus and cytosol results in an altered dephosphorylation-substrate spectrum (Kumar et al., 2019). Hypothesizing that FBXL6 might affect the localization of PPM1G by ubiquitylation via K63-linkage, confocal imaging with immunofluorescent staining of endogenous PPM1G was performed of FBXL6-depleted AML cells versus control (Fig. 24). PPM1G showed a nuclear localization in MOLM-13 cells which was not changed upon FBXL6 knockout, suggesting a different role of FBXL6-mediated ubiquitylation on PPM1G.

To elucidate in which way PPM1G is affected by FBXL6, future experiments may investigate the effect of FBXL6 depletion or overexpression on dephosphorylation substrates downstream of PPM1G. Several different substrates of PPM1G are known, including the histones H2A-H2B, the deubiquitinating enzyme USP7, and the cell cycle inhibitor p27 (Khoronenkova et al., 2012; Kimura et al., 2006; Sun et al., 2016). Thereby PPM1G exerts its functions as a tumor suppressor through the regulation of cell growth and DNA-damage response. For instance, DNA damage stimulates a tumor suppressive function of PPM1G: the dephosphorylation of USP7, which finally leads to the upregulation of p53 to induce a cell cycle arrest (Khoronenkova et al., 2012). Likewise, PPM1G-mediated dephosphorylation of p27 induces a cell cycle arrest by stabilization of p27 (Sun et al., 2016). Research on PPM1G has mainly been focused on solid tumors such as hepatocellular carcinoma, while its role in hematologic malignancies is still unclear (Chaudhary & Maddika, 2014; D. Chen et al., 2021; Kumar et al., 2019). Therefore, an unbiased approach seems useful to investigate the downstream effects of PPM1G under FBXL6 modulation in AML cells. It would be highly interesting to generate a PPM1G interactome by immunoprecipitation with subsequent mass spectrometry under FBXL6 knockout or overexpression versus control. The obtained lists of FBXL6-affected interactors could then be cross-validated with a second unbiased screen looking at differentially phosphorylated proteins upon FBXL6 modulation that could be identified in a phospho-proteomics experiment. Even though no functions of PPM1G have been described beyond specific dephosphorylation of substrate proteins, there might be other, so far undescribed activities of PPM1G in AML cells. The mass spectrometric screen for PPM1G interactors might shed light on novel PPM1G functions.

Furthermore, evidence for a direct connection between PPM1G-ubiquitylation and the phenotypic effects of FBXL6 depletion is still pending. For established substrate-ligase pairs the phenotypic effects of the ligase-knockout can usually be reversed or rescued by simultaneous depletion of the substrate (Fung et al., 2018). Due to the non-degradative nature of the FBXL6-mediated ubiquitylation of PPM1G, mere modulation of PPM1G expression by knockout or overexpression will likely not be conclusive since the protein abundance of PPM1G is not affected by FBXL6. A possible approach would be to establish a knockout of PPM1G in AML cells and investigate the phenotypic effects of simultaneous overexpression of wild type PPM1G versus a point mutant that cannot be ubiquitylated by FBXL6 anymore. To this end, the respective lysine residues which were differentially ubiquitylated upon FBXL6-depletion in the DiGly-IP (Fig. 6) will have to be confirmed by single amino acid exchanges from lysine to arginine using site-directed mutagenesis and *in-vivo*-ubiquitylation

experiments. Further evidence for PPM1G being an AML-relevant ubiquitylation substrate of FBXL6 will eventually lead to a deeper understanding of the cellular function of FBXL6 and the cell biological effects of aberrant overexpression of FBXL6 in AML.

5.2.2 Recent publications on FBXL6 substrates in solid tumors

Two very recent publications have described FBXL6 as a vulnerability in two solid tumor entities. While this confirms our findings that FBXL6 has pro-tumorigenic functions, different ubiquitylation substrates were identified. One study identified the major cellular chaperone HSP90AA1 as a K63-type ubiquitylation substrate in hepatocellular carcinoma (Shi et al., 2020). The second study provided evidence for degradative ubiquitylation of the tumor suppressor p53 (Li et al., 2021). Even though F-box proteins are known to specifically bind to more than one substrate (Cardozo & Pagano, 2004), it seems very unlikely that HSP90AA1 and p53 are ubiquitylated by FBXL6 in AML, since neither of the two proteins scored under the applied criteria for substrate identification. HSP90AA1 was enriched in two out of three interactome screens, which is not surprising under the circumstances of ectopic overexpression of FBXL6 since HSP90 ensures correct protein folding (Schopf et al., 2017). However, the detected ubiquitin-remnant peptides of HSP90AA1 were not changed in their abundance upon FBXL6 depletion in the DiGly-IP. For p53, neither of the four proteomic substrate screens described above yielded hints for a link between p53 and FBXL6 in AML.

Another recent study demonstrated the implication of FBXL6 in the quality control of mitochondrial ribosomal proteins (Lavie et al., 2023). Experiments conducted in cervical cancer cells showed that FBXL6 interacts with ribosomal proteins while residing in the cytoplasm. Given that FBXL6 was found to be solely localized in the nucleus of AML cells (Fig. 13), the activity toward cytosolic ribosomal proteins can be neglected for AML.

5.3 Excessive protease activity marks a pitfall for AML research

The detection of a so far undescribed second form of FBXL6 in immunoblots, which was specifically present in AML cell lines and not in any other tested cancer entity prompted the question of how FBXL6 is regulated in AML (Fig. 11). Importantly, a distinct shift of the FBXL6 band pattern in favor of the higher running form was observed upon forced myeloid differentiation of AML cell lines, independent of the applied differentiating agent (Fig. 14). As blocked differentiation is a hallmark of AML (Döhner et al., 2015), a regulatory mechanism dependent on the stemness status of myeloid cells was considered of high relevance for this project. The running height of the bands, with the upper band corresponding to the predicted molecular weight of the canonical FBXL6 amino acid sequence, and the finding that both bands were i) depleted by FBXL6 knockout/knockdown and ii) generated by ectopic expression of FBXL6 isoform 1 cDNA led to the hypothesis of proteolytic cleavage as the underlying mechanism (Fig. 12). Indeed, *in-vitro*-cleavage assays indicated that FBXL6 is cleaved by a member of the serine-type family of proteases (Fig. 25-26). A dual approach combining bottom-up and top-down proteomics identified the cleavage site in the N-terminal part of FBXL6 between Leu47 and Ser50, generating a C-terminal fragment of FBXL6 with fully intact F-box and LRR domains (Fig. 28). Lacking a solved 3D structure of FBXL6, artificial intelligence-based modeling of the FBXL6 protein structure indicated that the cleaved unstructured N-terminal part might alter the substrate specificity of FBXL6 (Fig. 29).

Functional annotation of the FBXL6 interactome screens pointed toward Cathepsin G (CatG) as the responsible protease, which could be confirmed by *in-vitro*-cleavage assays using a CatG-specific inhibitor and immunoprecipitation assays (Fig. 30).

While searching the literature for CatG and its implications in the stemness of AML, several publications surfaced which reported on excessive proteolytic activity of CatG during cell lysis which led to major misinterpretations of immunoblot data. For STAT5, which was believed to be a CatG substrate that specifically affects the stemness of AML cells, preparation of cell lysates under denaturing conditions using an SDS-containing buffer proved that CatG-mediated cleavage of STAT5 does not occur naturally in living cells (Schuster et al., 2007). A similar artifact has previously been reported for the cleavage of STAT3 by neutrophil elastase (NE) as well as the processing of p65 by CatG already in 1994 (Franzoso et al., 1994; Kato et al., 2004). In each case, this phenomenon could be explained by insufficient protease inhibition during standard cell lysis despite the addition of widely used inhibitors or commercially available cocktails for protease inhibition. Physiologically, myeloid cells produce high levels of serine proteases for immune-related roles such as generating peptides for antigen presentation or regulation of cytokine activity by cleavage (Pham, 2006). To prevent uncontrolled cleavage of cellular proteins, proteases are stored in cytoplasmic granules of living cells (Kettritz, 2016). As soon as all cellular compartments are broken down during cell lysis, the released proteases may cleave proteins that normally reside in other cellular compartments. Since FBXL6 was found to be localized in the nucleus, an artifact seemed plausible. Preparation of cell lysates under denaturing conditions in comparison to the standard lysis that was applied throughout this study, unfortunately, confirmed that CatG-mediated cleavage of FBXL6 is a mere technical artifact and lacks any biological relevance (Fig. 33).

Since many of the commonly used AML cell lines express high levels of CatG (Fig. 11) and presumably also other serine proteases (Kettritz, 2016), special precautions must be taken when preparing extracts from these cells. For instance, denaturing cell lysis using an SDS-containing buffer might be the first choice whenever cell extracts are not processed further but are directly used for immunoblot analysis. Conversely, if the native conformation of extracted proteins is crucial for example in immunoprecipitation studies, additional protease inhibitors or higher concentrations thereof may be used. In the case of FBXL6 in AML cells, the addition of a CatG-specific inhibitor abolished FBXL6 cleavage (Fig. 33). A recent study on the proteomic and phospho-proteomic landscapes of AML described a protocol for thawing bone marrow aspirates from a biobank in the presence of di-isopropyl fluorophosphate (DFP) to avoid cleavage artifacts by serine proteases in mass spectrometric measurements (Kramer et al., 2022). Due to its potent neurotoxicity, DFP is commonly substituted by the less toxic but also less reactive inhibitors AEBSF and PMSF, which were also used in this study and inhibited CatG insufficiently (Hedstrom, 2001). DFP might still be used in crucial experiments under strict safety measures. Additional strategies to avoid cleavage artifacts by serine proteases in AML cells comprise the usage of cell lines with generally low protease expression levels or the generation of protease knockout cells, as demonstrated in a study on the transcription profile of HOXA9 (Zhong et al., 2018). Notably, HOXA9 was rapidly degraded in cell extracts from human AML cell lines and primary murine HSPCs (hematopoietic stem/progenitor cells), which could only be overcome by a triple-knockout of the serine proteases CatG, NE, and proteinase-3, while high concentrations of AEBSF or PMSF failed to inhibit proteolysis of HOXA9 (Zhong et al., 2018).

Some pieces of data in this study must be re-evaluated after the cleavage of FBXL6 was discovered to be an artifact during cell lysis. The panel of AML and non-AML cell lines should be reproduced with cell pellets subjected to denaturing lysis to determine the correct total protein levels of FBXL6 across the whole panel (Fig. 11). The same accounts for the investigation of FBXL6 protein abundance upon forced differentiation using TPA or ATRA. FBXL6 might be downregulated or not regulated at all on the protein level upon myeloid differentiation, an effect masked by CatG cleavage (Fig. 14, Fig. 31). Regarding the proteomic screens for substrate identification, only the interactome from MV4-11 cells might be affected by the cleavage artifact, since the cell lines used for the additional screens generally showed rather low CatG expression and cleaved FBXL6. In the MV4-11 interactome, there might be false positive as well as false negative results: the cleaved form of FBXL6 might bind to non-physiologic interaction partners during the immunoprecipitation that might then be misinterpreted as substrate candidates. On the contrary, true interaction partners might also be subjected to misguided proteolytic cleavage in the used lysis buffer and therefore be unable to co-precipitate with FBXL6. From a technical perspective, it might be possible that proteolytic cleavage of E3-ligase substrates affects the generation of tryptic peptides in the sample preparation process prior to mass spectrometry, which might impede correct protein identification. The latter point is likely more important when generating a full (phospho-) proteome as stated by Timothy Ley and colleagues (Kramer et al., 2022), since protein identification in the interactome studies presented above required more than one unique peptide for each protein. Conversely, substrate identification screens such as the herein described DiGly-IP with subsequent identification of ubiquitin-remnant motives might be affected by excessive protease cleavage, since the detection of differential ubiquitylation might depend on one particular tryptic peptide.

In conclusion, cell biological and biochemical assays in AML cells need to be performed with special precautions to avoid artifacts through excessive, unphysiological protease activity. Despite these challenges, FBXL6 could be identified as a novel vulnerability in AML, which ubiquitylates the protein phosphatase PPM1G. Further studies are required to define the molecular and cellular consequences of K63-linked polyubiquitylation of PPM1G by FBXL6.

6   Acknowledgements

Thanks to the scientific and moral support of many people, the time spent working on this dissertation was filled with valuable experiences, learning, inspirational discussions, lots of fun, and personal growth. I wish to thank everyone who has contributed to the success of this work and who made the past seven years special!

First, I want to thank my supervisor Prof. Dr. Florian Bassermann for giving me the opportunity to conduct the research leading to this thesis in his lab, for countless inspiring scientific discussions, and for constantly supporting this project. Next, I want to thank my second thesis advisory committee member and collaborator Prof. Dr. Bernhard Küster and his team – especially Dr. Johannes Krumm and Dr. Yun-Chien Chang for their invaluable support in conducting and discussing mass spectrometry-based experiments throughout the project.

Special thanks go to Dr. Ruth Eichner for being an encouraging and understanding mentor, who initially showed me how to conduct and interpret experiments back in the days of my Master's thesis and supported me throughout, even when she was busy with a hundred other things and the hour was getting (really) late. Your enthusiasm always jumped over easily!

Big thanks go to Dr. David Brockelt, who started this project and was always open for discussions after leaving the lab, and Dr. Ria Spallek for the encouragement and important scientific advice. Moreover, a warm thank you goes to Vinona Wagner and Antje Gabriel for all the shared coffee breaks, scientific debates, creative ideas, and moral support. You made this lab a fun place!

Another special thank you to Daniela Koch and Abirami Augsburger for being invaluable members of the 'Team FBXL6'. Daniela, it was a pleasure to introduce you into the laboratory work on our favorite ubiquitin ligase - thank you for bringing in your own ideas, lots of motivation, and having exciting discussions on the project. Thank you, Abirami, for your constant commitment and crucial support in conducting numerous experiments!

I want to thank all members of the Bassermann lab for being such an open, helpful, and fun group! Thank you for all your constructive input, help with various techniques, wonderful lunch breaks, and for joining the AG Bassermann Lab Hikes!

Moreover, I want to thank all collaboration partners for making this technically versatile work possible. Special thanks to Dr. Piero Giansanti, Dr. Barbara Steigenberger, and Victoria Sanchez for crucial support with mass-spectrometric analyses and data interpretation. Thank you also to Prof. Dr. Irmela Jeremias, Romina Ludwig, and Jan Philipp Schmid for setting up and performing the PDX experiments. Likewise, I want to thank Dr. Wencke Walter and Prof. Dr. Torsten Haferlach for providing support with patient data analysis.

Thank you to all colleagues from the core facilities at TranslaTUM for solving various problems and helping with a lot of motivation and skill, especially Markus Utzt, Dr. Ritu Mishra, and Linda Bachmann.

Finally, my biggest thanks go to my husband Dominik, my whole family, and my dearest friends (including 'die alten Mädels und Julia') for constant support, understanding, encouragement, and patience. Thank you for believing in me!

7 Publications

7.1 Articles in peer-reviewed journals

Michael Heider, Ruth Eichner, Jacob Stroh, Volker Morath, **Anna Kuisl**, Jana Zecha, Jannis Lawatscheck, Kheewoong Baek, Anne-Kathrin Garz, Martina Rudelius, Friedrich-Christian Deuschle, Ulrich Keller, Simone Lemeer, Mareike Verbeek, Katharina S. Götze, Arne Skerra, Wolfgang A. Weber, Johannes Buchner, Brenda A. Schulman, Bernhard Kuster, Vanesa Fernandez-Saiz, and Florian Bassermann. "The IMiD target CRBN determines HSP90 activity toward transmembrane proteins essential in multiple myeloma". **Molecular Cell** (2021) 18;81(6):1170-1186.e10.

Svenja Lier, Andreas Sellmer, Felix Orben, Stephanie Heinzlmeir, Lukas Krauß, Christian Schneeweis, Zonera Hassan, Carolin Schneider, Arlett Patricia Gloria Schäfer, Herwig Pongratz, Thomas Engleitner, Rupert Öllinger, **Anna Kuisl**, Florian Bassermann, Christoph Schlag, Bo Kong, Stefan Dove, Bernhard Kuster, Roland Rad, Maximilian Reichert, Matthias Wirth, Dieter Saur, Siavosh Mahboobi, Günter Schneider. "A novel Cereblon E3 ligase modulator with antitumor activity in gastrointestinal cancer". **Bioorganic Chemistry** (2022) 119:105505

7.2 Conference contributions

Anna Kuisl, Ruth Eichner, Susan Kläger, Vanesa Fernandez-Saiz, Bernhard Küster, Florian Bassermann. „Unbiased interactome analysis of CD147/MCT1 reveals mediators of resistance to immunomodulatory drugs in multiple myeloma". Jahrestagung der Deutschen, Österreichischen und Schweizerischen Gesellschaften für Hämatologie und Medizinische Onkologie, Berlin, 2019. Poster.

8 References

Adès, L., Girshova, L., Doronin, V. A., Díez-Campelo, M., Valcárcel, D., Kambhampati, S., Viniou, N. A., Woszczyk, D., De Paz Arias, R., Symeonidis, A., Anagnostopoulos, A., Munhoz, E. C., Platzbecker, U., Santini, V., Fram, R. J., Yuan, Y., Friedlander, S., Faller, D. V., & Sekeres, M. A. (2022). Pevonedistat plus azacitidine vs azacitidine alone in higher-risk MDS/chronic myelomonocytic leukemia or low-blast-percentage AML. *Blood Advances*, *6*(17), 5132–5145. https://doi.org/10.1182/BLOODADVANCES.2022007334

Bahrami, E., Schmid, J. P., Jurinovic, V., Becker, M., Wirth, A. K., Ludwig, R., Kreissig, S., Duque Angel, T. V., Amend, D., Hunt, K., Öllinger, R., Rad, R., Frenz, J. M., Solovey, M., Ziemann, F., Mann, M., Vick, B., Wichmann, C., Herold, T., … Jeremias, I. (2023). Combined proteomics and CRISPR-Cas9 screens in PDX identify ADAM10 as essential for leukemia in vivo. *Molecular Cancer*, *22*(1), 107. https://doi.org/10.1186/s12943-023-01803-0

Bai, C., Sen, P., Hofmann, K., Ma, L., Goebl, M., Harper, J. W., & Elledge, S. J. (1996). SKP1 connects cell cycle regulators to the ubiquitin proteolysis machinery through a novel motif, the F-box. *Cell*, *86*(2), 263–274. https://doi.org/10.1016/S0092-8674(00)80098-7

Bassermann, F., Eichner, R., & Pagano, M. (2014). The ubiquitin proteasome system — Implications for cell cycle control and the targeted treatment of cancer. *Biochimica et Biophysica Acta (BBA) - Molecular Cell Research*, *1843*(1), 150–162. https://doi.org/10.1016/J.BBAMCR.2013.02.028

Bateman, A., Martin, M. J., Orchard, S., Magrane, M., Ahmad, S., Alpi, E., Bowler-Barnett, E. H., Britto, R., Bye-A-Jee, H., Cukura, A., Denny, P., Dogan, T., Ebenezer, T. G., Fan, J., Garmiri, P., da Costa Gonzales, L. J., Hatton-Ellis, E., Hussein, A., Ignatchenko, A., … Zhang, J. (2023). UniProt: the Universal Protein Knowledgebase in 2023. *Nucleic Acids Research*, *51*(D1), D523–D531. https://doi.org/10.1093/NAR/GKAC1052

Baumann, U., Fernández-Saíz, V., Rudelius, M., Lemeer, S., Rad, R., Knorn, A. M., Slawska, J., Engel, K., Jeremias, I., Li, Z., Tomiatti, V., Illert, A. L., Targosz, B. S., Braun, M., Perner, S., Leitges, M., Klapper, W., Dreyling, M., Miething, C., … Bassermann, F. (2014). Disruption of the PRKCD-FBXO25-HAX-1 axis attenuates the apoptotic response and drives lymphomagenesis. *Nature Medicine*, *20*(12), 1401–1409. https://doi.org/10.1038/NM.3740

Bennett, J. M., Catovsky, D., Daniel, M. -T, Flandrin, G., Galton, D. A. G., Gralnick, H. R., & Sultan, C. (1976). Proposals for the classification of the acute leukaemias. French-American-British (FAB) co-operative group. *British Journal of Haematology*, *33*(4), 451–458. https://doi.org/10.1111/J.1365-2141.1976.TB03563.X

Bestilny, L. J., & Riabowol, K. T. (2000). A role for serine proteases in mediating phorbol ester-induced differentiation of HL-60 cells. *Experimental Cell Research*, *256*(1), 264–271. https://doi.org/10.1006/excr.2000.4821

Bhoj, V. G., & Chen, Z. J. (2009). Ubiquitylation in innate and adaptive immunity. *Nature*, *458*(7237), 430–437. https://doi.org/10.1038/NATURE07959

Bottomly, D., Long, N., Schultz, A. R., Kurtz, S. E., Tognon, C. E., Johnson, K., Abel, M., Agarwal, A., Avaylon, S., Benton, E., Blucher, A., Borate, U., Braun, T. P., Brown, J., Bryant, J., Burke, R., Carlos, A., Chang, B. H., Cho, H. J., … Tyner, J. W. (2022). Integrative analysis of drug response and clinical outcome in acute myeloid leukemia. *Cancer Cell*, *40*(8), 850-864.e9. https://doi.org/10.1016/j.ccell.2022.07.002

Buetow, L., & Huang, D. T. (2016). Structural insights into the catalysis and regulation of E3 ubiquitin ligases. *Nature Reviews. Molecular Cell Biology*, *17*(10), 626. https://doi.org/10.1038/NRM.2016.91

Burnett, A., & Stone, R. (2020). AML: New Drugs but New Challenges. In *Clinical Lymphoma, Myeloma and Leukemia* (Vol. 20, Issue 6, pp. 341–350). Elsevier Inc. https://doi.org/10.1016/j.clml.2020.02.005

Cardozo, T., & Pagano, M. (2004). The SCF ubiquitin ligase: Insights into a molecular machine. In *Nature Reviews Molecular Cell Biology* (Vol. 5, Issue 9, pp. 739–751). https://doi.org/10.1038/nrm1471

Carrano, A. C., Eytan, E., Hershko, A., & Pagano, M. (1999). SKP2 is required for ubiquitin-mediated degradation of the CDK inhibitor p27. *Nature Cell Biology 1999 1:4*, *1*(4), 193–199. https://doi.org/10.1038/12013

Catherman, A. D., Skinner, O. S., & Kelleher, N. L. (2014). Top Down Proteomics: Facts and Perspectives. *Biochemical and Biophysical Research Communications*, *445*(4), 683. https://doi.org/10.1016/J.BBRC.2014.02.041

Cenciarelli, C., Chiaur, D. S., Guardavaccaro, D., Parks, W., Vidal, M., Pagano, M., Pediatrics, ‡, & Kaplan, *. (1999). Identification of a family of human F-box proteins. *Current Biology*, *9*(20), 1177–1179. http://current-biology.com/supmat/supmatin.htm.

Chaudhary, N., & Maddika, S. (2014). WWP2-WWP1 Ubiquitin Ligase Complex Coordinated by PPM1G Maintains the Balance between Cellular p73 and ΔNp73 Levels. *Molecular and Cellular Biology*, *34*(19), 3754–3764. https://doi.org/10.1128/mcb.00101-14

Chen, B. B., Glasser, J. R., Coon, T. A., Zou, C., Miller, H. L., Fenton, M., McDyer, J. F., Boyiadzis, M., & Mallampalli, R. K. (2012). F-box protein FBXL2 targets cyclin D2 for ubiquitination and degradation to inhibit leukemic cell proliferation. *Blood*, *119*(13), 3132–3141. https://doi.org/10.1182/BLOOD-2011-06-358911

Chen, D., Zhao, Z., Chen, L., Li, Q., Zou, J., & Liu, S. (2021). PPM1G promotes the progression of hepatocellular carcinoma via phosphorylation regulation of alternative splicing protein SRSF3. *Cell Death and Disease*, *12*(8). https://doi.org/10.1038/S41419-021-04013-Y

Chen, Q., Xie, W., Kuhn, D. J., Voorhees, P. M., Lopez-Girona, A., Mendy, D., Corral, L. G., Krenitsky, V. P., Xu, W., Parseval, L. M. De, Webb, D. R., Mercurio, F., Nakayama, K. I., Nakayama, K., & Orlowski, R. Z. (2008). Targeting the p27 E3 ligase SCF(Skp2) results in p27- and Skp2-mediated cell-cycle arrest and activation of autophagy. *Blood*, *111*(9), 4690–4699. https://doi.org/10.1182/BLOOD-2007-09-112904

Ciechanover, A., & Ben-Saadon, R. (2004). N-terminal ubiquitination: more protein substrates join in. *Trends in Cell Biology*, *14*(3), 103–106. https://doi.org/10.1016/J.TCB.2004.01.004

Coux, O., Tanaka, K., & Goldberg, A. L. (1996). Structure and functions of the 20S and 26S proteasomes. *Annual Review of Biochemistry*, *65*, 801–847. https://doi.org/10.1146/ANNUREV.BI.65.070196.004101

Cozzio, A., Passegué, E., Ayton, P. M., Karsunky, H., Cleary, M. L., & Weissman, I. L. (2003). Similar MLL-associated leukemias arising from self-renewing stem cells and short-lived myeloid progenitors. *Genes & Development*, *17*(24), 3029–3035. https://doi.org/10.1101/GAD.1143403

Dammer, E. B., Na, C. H., Xu, P., Seyfried, N. T., Duong, D. M., Cheng, D., Gearing, M., Rees, H., Lah, J. J., Levey, A. I., Rush, J., & Peng, J. (2011). Polyubiquitin linkage profiles in three models of proteolytic stress suggest the etiology of Alzheimer disease. *The Journal of Biological Chemistry*, *286*(12), 10457–10465. https://doi.org/10.1074/JBC.M110.149633

Das, S., & Krainer, A. R. (2014). Emerging functions of SRSF1, splicing factor and oncoprotein, in RNA metabolism and cancer. In *Molecular Cancer Research* (Vol. 12, Issue 9, pp. 1195–1204). American Association for Cancer Research Inc. https://doi.org/10.1158/1541-7786.MCR-14-0131

Daver, N., Wei, A. H., Pollyea, D. A., Fathi, A. T., Vyas, P., & DiNardo, C. D. (2020). New directions for emerging therapies in acute myeloid leukemia: the next chapter. In *Blood Cancer Journal* (Vol. 10, Issue 10). Springer Nature. https://doi.org/10.1038/s41408-020-00376-1

Davis, H. E., Morgan, J. R., & Yarmush, M. L. (2002). Polybrene increases retrovirus gene transfer efficiency by enhancing receptor-independent virus adsorption on target cell membranes. *Biophysical Chemistry*, *97*(2–3), 159–172. https://doi.org/10.1016/S0301-4622(02)00057-1

DepMap Consortium. (2018). *DepMap: The Cancer Dependency Map Project at Broad Institute*. https://depmap.org/portal/

Dickinson, A. M., Norden, J., Li, S., Hromadnikova, I., Schmid, C., Schmetzer, H., & Jochem-Kolb, H. (2017). Graft-versus-Leukemia Effect Following Hematopoietic Stem Cell Transplantation for Leukemia. *Frontiers in Immunology*, *8*(JUN), 1. https://doi.org/10.3389/FIMMU.2017.00496

Dietachmayr, M., Rathakrishnan, A., Karpiuk, O., von Zweydorf, F., Engleitner, T., Fernández-Sáiz, V., Schenk, P., Ueffing, M., Rad, R., Eilers, M., Gloeckner, C. J., Clemm von Hohenberg, K., & Bassermann, F. (2020). Antagonistic activities of CDC14B and CDK1 on USP9X regulate WT1-dependent mitotic transcription and survival. *Nature Communications*, *11*(1). https://doi.org/10.1038/S41467-020-15059-5

Döhner, H., Estey, E., Grimwade, D., Amadori, S., Appelbaum, F. R., Büchner, T., Dombret, H., Ebert, B. L., Fenaux, P., Larson, R. A., Levine, R. L., Lo-Coco, F., Naoe, T., Niederwieser, D., Ossenkoppele, G. J., Sanz, M., Sierra, J., Tallman, M. S., Tien, H.-F., … Bloomfield, C. D. (2017). Diagnosis and management of AML in adults: 2017 ELN recommendations from an international expert panel. *Blood*, *129*(4), 424–447. https://doi.org/10.1182/blood-2016-08-733196

Döhner, H., Wei, A. H., Appelbaum, F. R., Craddock, C., DiNardo, C. D., Dombret, H., Ebert, B. L., Fenaux, P., Godley, L. A., Hasserjian, R. P., Larson, R. A., Levine, R. L., Miyazaki, Y., Niederwieser, D., Ossenkoppele, G., Sierra, J., Stein, E. M., Tallman, M. S., Tien, H.-F., … Löwenberg, B. (2022). Diagnosis and management of AML in adults: 2022 recommendations from an international expert panel on behalf of the ELN. *Blood*, *140*(12). https://doi.org/10.1182/blood.2019000962

Döhner, H., Weisdorf, D. J., & Bloomfield, C. D. (2015). Acute Myeloid Leukemia. *New England Journal of Medicine*, *373*(12), 1136–1152. https://doi.org/10.1056/NEJMra1406184

Dong, Y., Shi, O., Zeng, Q., Lu, X., Wang, W., Li, Y., Wang, Q., Wang, Q., & Wang, Q. (2020). Leukemia incidence trends at the global, regional, and national level between 1990 and 2017. *Experimental Hematology and Oncology*, *9*(1). https://doi.org/10.1186/s40164-020-00170-6

Erb, M. A., Scott, T. G., Li, B. E., Xie, H., Paulk, J., Seo, H. S., Souza, A., Roberts, J. M., Dastjerdi, S., Buckley, D. L., Sanjana, N. E., Shalem, O., Nabet, B., Zeid, R., Offei-Addo, N. K., Dhe-Paganon, S., Zhang, F., Orkin, S. H., Winter, G. E., & Bradner, J. E. (2017). Transcription control by the ENL YEATS domain in acute leukaemia. *Nature*, *543*(7644), 270–274. https://doi.org/10.1038/NATURE21688

Fernández-Sáiz, V., Targosz, B. S., Lemeer, S., Eichner, R., Langer, C., Bullinger, L., Reiter, C., Slotta-Huspenina, J., Schroeder, S., Knorn, A. M., Kurutz, J., Peschel, C., Pagano, M., Kuster, B., & Bassermann, F. (2013). SCFFbxo9 and CK2 direct the cellular response to growth factor withdrawal via Tel2/Tti1 degradation and promote survival in multiple myeloma. *Nature Cell Biology*, *15*(1), 72–81. https://doi.org/10.1038/NCB2651

Franzoso, G., Biswas, P., Poli, G., Carlson, L. M., Brown, K. D., Tomita-Yamaguchi, M., Fauci, A. S., & Siebenlist, U. K. (1994). A Family of Serine Proteases Expressed Exclusively in Myelo-Monocytic Cells Specifically Processes the Nuclear Factor-КB Subunit p65 In Vitro and May Impair Human Immunodeficiency Virus Replication in These Cells. *The Journal of Experimental Medicine*, *180*, 1445–1456. http://rupress.org/jem/article-pdf/180/4/1445/1105797/1445.pdf

Fung, E., Richter, C., Yang, H., Schäffer, I., Fischer, R., Kessler, B. M., Bassermann, F., & D'Angiolella, V. (2018). FBXL13 directs the proteolysis of CEP192 to regulate centrosome homeostasis and cell migration. *EMBO Reports*, *19*(3). https://doi.org/10.15252/EMBR.201744799

Grisolano, J. L., O'neal, J., Cain, J., Tomasson, M. H., & Rowley, J. D. (2003). An activated receptor tyrosine kinase, TELPDGFR, cooperates with AML1ETO to induce acute myeloid leukemia in mice. In *PNAS August* (Vol. 5, Issue 16). www.pnas.orgcgidoi10.1073pnas.1531730100

Hanahan, D., & Weinberg, R. A. (2000). The hallmarks of cancer. *Cell*, *100*(1), 57–70. https://doi.org/10.1016/S0092-8674(00)81683-9

Hedstrom, L. (2001). An Overview of Serine Proteases. *Current Protocols in Protein Science*, *26*(1), 21.10.1-21.10.8. https://doi.org/10.1002/0471140864.PS2110S26

Henser-Brownhill, T., Monserrat, J., & Scaffidi, P. (2017). Generation of an arrayed CRISPR-Cas9 library targeting epigenetic regulators: from high-content screens to in vivo assays. *Epigenetics*, *12*(12),

1065–1075. https://doi.org/10.1080/15592294.2017.1395121/SUPPL_FILE/KEPI_A_1395121_SM5055.RAR

Hershko, A., & Ciechanover, A. (1998). THE UBIQUITIN SYSTEM. In *Annu. Rev. Biochem* (Vol. 67). www.annualreviews.org

Hicke, L., & Dunn, R. (2003). Regulation of membrane protein transport by ubiquitin and ubiquitin-binding proteins. *Annual Review of Cell and Developmental Biology*, *19*, 141–172. https://doi.org/10.1146/ANNUREV.CELLBIO.19.110701.154617

Höckendorf, U., Yabal, M., Herold, T., Munkhbaatar, E., Rott, S., Jilg, S., Kauschinger, J., Magnani, G., Reisinger, F., Heuser, M., Kreipe, H., Sotlar, K., Engleitner, T., Rad, R., Weichert, W., Peschel, C., Ruland, J., Heikenwalder, M., Spiekermann, K., … Jost, P. J. (2016). RIPK3 Restricts Myeloid Leukemogenesis by Promoting Cell Death and Differentiation of Leukemia Initiating Cells. *Cancer Cell*, *30*(1), 75–91. https://doi.org/10.1016/J.CCELL.2016.06.002

Hu, C. W., Qiu, Y., Ligeralde, A., Raybon, A. Y., Yoo, S. Y., Coombes, K. R., Qutub, A. A., & Kornblau, S. M. (2019). A quantitative analysis of heterogeneities and hallmarks in acute myelogenous leukaemia. *Nature Biomedical Engineering*, *3*(11), 889–901. https://doi.org/10.1038/s41551-019-0387-2

Hulsen, T., de Vlieg, J., & Alkema, W. (2008). BioVenn - A web application for the comparison and visualization of biological lists using area-proportional Venn diagrams. *BMC Genomics*, *9*(1), 1–6. https://doi.org/10.1186/1471-2164-9-488/FIGURES/4

Jayavelu, A. K., Wolf, S., Buettner, F., Alexe, G., Häupl, B., Comoglio, F., Schneider, C., Doebele, C., Fuhrmann, D. C., Wagner, S., Donato, E., Andresen, C., Wilke, A. C., Zindel, A., Jahn, D., Splettstoesser, B., Plessmann, U., Münch, S., Abou-El-Ardat, K., … Oellerich, T. (2022). The proteogenomic subtypes of acute myeloid leukemia. *Cancer Cell*, *40*(3), 301-317.e12. https://doi.org/10.1016/j.ccell.2022.02.006

Jiang, H., Bian, W., Sui, Y., Li, H., Zhao, H., Wang, W., & Li, X. (2022). FBXO42 facilitates Notch signaling activation and global chromatin relaxation by promoting K63-linked polyubiquitination of RBPJ. *Science Advances*, *8*(38), 4831. https://doi.org/10.1126/SCIADV.ABQ4831

Jin, J., Cardozo, T., Lovering, R. C., Elledge, S. J., Pagano, M., & Harper, J. W. (2004). Systematic analysis and nomenclature of mammalian F-box proteins. *Genes & Development*, *18*(21), 2573. https://doi.org/10.1101/GAD.1255304

Jing, H., Cao, J., Xiang, S., Yang, B., Ying, M., Shao, X., Liu, Y., Qi, X., Chen, Y., Song, H., Hu, R., Wei, G., & He, Q. (2018). *Ubiquitin-dependent degradation of CDK2 drives the therapeutic differentiation of AML by targeting PRDX2*. https://doi.org/10.1182/blood-2017-10-813139

Juliusson, G., Lazarevic, V., Hö, A.-S., Hagberg, O., & Hö, M. (2012). *Acute myeloid leukemia in the real world: why population-based registries are needed*. https://doi.org/10.1182/blood-2011

Kamada, R., Kudoh, F., Ito, S., Tani, I., Janairo, J. I. B., Omichinski, J. G., & Sakaguchi, K. (2020). Metal-dependent Ser/Thr protein phosphatase PPM family: Evolution, structures, diseases and inhibitors. In *Pharmacology and Therapeutics* (Vol. 215). Elsevier Inc. https://doi.org/10.1016/j.pharmthera.2020.107622

Kansas, G. S., Muirhead, M. J., & Dailey, M. O. (1990). Expression of the CD11/CD18, Leukocyte Adhesion Molecule 1, and CD44 Adhesion Molecules During Normal Myeloid and Erythroid Differentiation in Humans. *Blood*, *76*(12), 2483–2492. https://doi.org/10.1182/BLOOD.V76.12.2483.2483

Kato, T., Sakamoto, E., Kutsuna, H., Kimura-Eto, A., Hato, F., & Kitagawa, S. (2004). Proteolytic Conversion of STAT3α to STAT3γ in Human Neutrophils. *Journal of Biological Chemistry*, *279*(30), 31076–31080. https://doi.org/10.1074/jbc.m400637200

Kelly, L. M., Liu, Q., Kutok, J. L., Williams, I. R., Boulton, C. L., & Gilliland, D. G. (2002). FLT3 internal tandem duplication mutations associated with human acute myeloid leukemias induce myeloproliferative disease in a murine bone marrow transplant model. *Blood*, *99*(1), 310–318. https://doi.org/10.1182/BLOOD.V99.1.310

Kettritz, R. (2016). Neutral serine proteases of neutrophils. *Immunological Reviews*, *273*(1), 232–248. https://doi.org/10.1111/imr.12441

Khoronenkova, S. V., Dianova, I. I., Ternette, N., Kessler, B. M., Parsons, J. L., & Dianov, G. L. D. (2012). ATM-Dependent Downregulation of USP7/HAUSP by PPM1G Activates p53 Response to DNA Damage. *Molecular Cell*, *45*(6), 801–813. https://doi.org/10.1016/j.molcel.2012.01.021

Khoury, J. D., Solary, E., Abla, O., Akkari, Y., Alaggio, R., Apperley, J. F., Bejar, R., Berti, E., Busque, L., C Chan, J. K., Chen, W., Chen, X., Chng, W.-J., Choi, J. K., Colmenero, I., Coupland, S. E., P Cross, N. C., De Jong, D., Tarek Elghetany, M., … Hochhaus, A. (2022). The 5th edition of the World Health Organization Classification of Haematolymphoid Tumours: Myeloid and Histiocytic/Dendritic Neoplasms. *Leukemia*, *36*, 1703–1719. https://doi.org/10.1038/s41375-022-01613-1

Khwaja, A., Bjorkholm, M., Gale, R. E., Levine, R. L., Jordan, C. T., Ehninger, G., Bloomfield, C. D., Estey, E., Burnett, A., Cornelissen, J. J., Scheinberg, D. A., Bouscary, D., & Linch, D. C. (2016). Acute myeloid leukaemia. *Nature Reviews Disease Primers*, *2*. https://doi.org/10.1038/nrdp.2016.10

Kim, J. T., Lim, M. J., Yoo, M.-A., Kim, K.-W., & Yeom, Y. Il. (2003). Regulation of E2F-mediated Transcription by FBXL-6 in HCT116 Cells. *Journal of Korean Association of Cancer Prevention*, *8*(4), 267–274.

Kim, W., Bennett, E. J., Huttlin, E. L., Guo, A., Li, J., Possemato, A., Sowa, M. E., Rad, R., Rush, J., Comb, M. J., Harper, J. W., & Gygi, S. P. (2011). Systematic and quantitative assessment of the ubiquitin-modified proteome. *Molecular Cell*, *44*(2), 325–340. https://doi.org/10.1016/j.molcel.2011.08.025

Kimura, H., Takizawa, N., Allemand, E., Hori, T., Iborra, F. J., Nozaki, N., Muraki, M., Hagiwara, M., Krainer, A. R., Fukagawa, T., & Okawa, K. (2006). A novel histone exchange factor, protein phosphatase 2Cγ, mediates the exchange and dephosphorylation of H2A-H2B. *Journal of Cell Biology*, *175*(3), 389–400. https://doi.org/10.1083/jcb.200608001

Kingston, R. E., Chen, C. A., & Okayama, H. (1999). Calcium Phosphate Transfection. *Current Protocols in Immunology*, *31*(1), 10.13.1-10.13.9. https://doi.org/10.1002/0471142735.IM1013S31

Kipreos, E. T., & Pagano, M. (2000). The F-box protein family. *Genome Biology 2000 1:5*, *1*(5), 1–7. https://doi.org/10.1186/GB-2000-1-5-REVIEWS3002

Koeffler, H. P. (2010). Is there a role for differentiating therapy in non-APL AML? *Best Pract Res Clin Heamatol.*, *23*(4), 503–508. https://doi.org/10.1016/j.beha.2010.09.014

Komander, D. (2009). The emerging complexity of protein ubiquitination. In *Biochemical Society Transactions* (Vol. 37, Issue 5, pp. 937–953). https://doi.org/10.1042/BST0370937

Komander, D., & Rape, M. (2012). The ubiquitin code. *Annual Review of Biochemistry*, *81*, 203–229. https://doi.org/10.1146/annurev-biochem-060310-170328

Kramer, M. H., Zhang, Q., Sprung, R., Day, R. B., Erdmann-Gilmore, P., Li, Y., Xu, Z., Helton, N. M., George, D. R., Mi, Y., Westervelt, P., Payton, J. E., Ramakrishnan, S. M., Miller, C. A., Link, D. C., Dipersio, J. F., Walter, M. J., Reid Townsend, R., & Ley, T. J. (2022). Proteomic and phosphoproteomic landscapes of acute myeloid leukemia. *Blood*, *140*(13). https://doi.org/10.1182/blood.2019000962

Kumar, P., Tathe, P., Chaudhary, N., & Maddika, S. (2019). PPM1G forms a PPP-type phosphatase holoenzyme with B56δ that maintains adherens junction integrity. *EMBO Reports*, *20*(10). https://doi.org/10.15252/embr.201846965

Kurata, J. S., & Lin, R. J. (2018). MicroRNA-focused CRISPR-Cas9 library screen reveals fitness-associated miRNAs. *RNA (New York, N.Y.)*, *24*(7), 966–981. https://doi.org/10.1261/RNA.066282.118

Lau, A. W., Fukushima, H., & Wei, W. (2012). The Fbw7 and Beta-TRCP E3 ubiquitin ligases and their roles in tumorigenesis. *Frontiers in Bioscience: A Journal and Virtual Library*, *17*(6), 2197. https://doi.org/10.2741/4045

Lavie, J., Lalou, C., Mahfouf, W., Dupuy, J.-W., Lacaule, A., Cywinska, A. A., Lacombe, D., Duchêne, A.-M., Raymond, A.-A., Rezvani, H. R., Ngondo, R. P., & Bénard, G. (2023). The E3 ubiquitin ligase FBXL6 controls the quality of newly synthesized mitochondrial ribosomal proteins. *Cell Reports*, *42*(6), 112579. https://doi.org/10.1016/j.celrep.2023.112579

Li, Y., Cui, K., Zhang, Q., Li, X., Lin, X., Tang, Y., Prochownik, E. V., & Li, Y. (2021). FBXL6 degrades phosphorylated p53 to promote tumor growth. *Cell Death and Differentiation*, *28*(7), 2112–2125. https://doi.org/10.1038/s41418-021-00739-6

Li, Y., Hu, K., Xiao, X., Wu, W., Yan, H., Chen, H., Chen, Z., & Yin, D. (2018). FBW7 suppresses cell proliferation and G2/M cell cycle transition via promoting γ-catenin K63-linked ubiquitylation. *Biochemical and Biophysical Research Communications*, *497*(2), 473–479. https://doi.org/10.1016/J.BBRC.2018.01.192

Lichtman, M. A. (2013). A historical perspective on the development of the cytarabine (7days) and daunorubicin (3days) treatment regimen for acute myelogenous leukemia: 2013 the 40th anniversary of 7+3. *Blood Cells, Molecules & Diseases*, *50*(2), 119–130. https://doi.org/10.1016/J.BCMD.2012.10.005

Lievens, S., Vanderroost, N., Van Heyden, J. Der, Gesellchen, V., Vidal, M., & Tavernier, J. (2009). Array MAPPIT: High-throughput interactome analysis in mammalian cells. *Journal of Proteome Research*, *8*(2), 877–886. https://doi.org/10.1021/pr8005167

Liu, J., Stevens, P. D., Eshleman, N. E., & Gao, T. (2013). Protein phosphatase PPM1G regulates protein translation and cell growth by dephosphorylating 4E binding protein 1 (4E-BP1). *Journal of Biological Chemistry*, *288*(32), 23225–23233. https://doi.org/10.1074/jbc.M113.492371

Lowry, O. H., Rosebrough, N. J., Farr, A. L., & RandallL, R. J. (1951). Protein measurement with the Folin phenol reagent. *The Journal of Biological Chemistry*, *193*(1), 265–275. https://doi.org/10.1016/s0021-9258(19)52451-6

Mason, B., & Laman, H. (2020). The FBXL family of F-box proteins: variations on a theme. *Open Biology*, *10*(11). https://doi.org/10.1098/rsob.200319

Mellacheruvu, D., Wright, Z., Couzens, A. L., Lambert, J. P., St-Denis, N. A., Li, T., Miteva, Y. V., Hauri, S., Sardiu, M. E., Low, T. Y., Halim, V. A., Bagshaw, R. D., Hubner, N. C., Al-Hakim, A., Bouchard, A., Faubert, D., Fermin, D., Dunham, W. H., Goudreault, M., … Nesvizhskii, A. I. (2013). The CRAPome: a Contaminant Repository for Affinity Purification Mass Spectrometry Data. *Nature Methods*, *10*(8), 730. https://doi.org/10.1038/NMETH.2557

Meng, L., Hu, Y.-T., & Xu, A.-M. (2023). F-box and leucine-rich repeat 6 promotes gastric cancer progression via the promotion of epithelial-mesenchymal transition . *World Journal of Gastrointestinal Oncology*, *15*(3), 490–503. https://doi.org/10.4251/wjgo.v15.i3.490

Mohr, S., Doebele, C., Comoglio, F., Berg, T., Beck, J., Bohnenberger, H., Alexe, G., Corso, J., Ströbel, P., Wachter, A., Beissbarth, T., Schnütgen, F., Cremer, A., Haetscher, N., Göllner, S., Rouhi, A., Palmqvist, L., Rieger, M. A., Schroeder, T., … Oellerich, T. (2017). Hoxa9 and Meis1 Cooperatively Induce Addiction to Syk Signaling by Suppressing miR-146a in Acute Myeloid Leukemia. *Cancer Cell*, *31*(4), 549-562.e11. https://doi.org/10.1016/J.CCELL.2017.03.001

Mrożek, K., Marcucci, G., Nicolet, D., Maharry, K. S., Becker, H., Whitman, S. P., Metzeler, K. H., Schwind, S., Wu, Y. Z., Kohlschmidt, J., Pettenati, M. J., Heerema, N. A., Block, A. M. W., Patil, S. R., Baer, M. R., Kolitz, J. E., Moore, J. O., Carroll, A. J., Stone, R. M., … Bloomfield, C. D. (2012). Prognostic significance of the European LeukemiaNet standardized system for reporting cytogenetic and molecular alterations in adults with acute myeloid leukemia. *Journal of Clinical Oncology*, *30*(36), 4515–4523. https://doi.org/10.1200/JCO.2012.43.4738

Mullis, K. B., & Faloona, F. A. (1987). Specific synthesis of DNA in vitro via a polymerase-catalyzed chain reaction. *Methods in Enzymology*, *155*(C), 335–350. https://doi.org/10.1016/0076-6879(87)55023-6

Owenberg, B. L. ̈, Pabst, T., Maertens, J., Van Norden, Y., Biemond, B. J., Schouten, H. C., Spertini, O., Vellenga, E., Graux, C., Havelange, V., De Greef, G. E., De Weerdt, O., Legdeur, M.-C. J. C., Kuball, J., Van, M., Kooy, M., Gjertsen, B. T., Jongen-Lavrencic, M., Van De Loosdrecht, A. A., …

Ossenkoppele, G. J. (2017). Therapeutic value of clofarabine in younger and middle-aged (18-65 years) adults with newly diagnosed AML. *Blood*, *129*(12), 1636–1645. https://doi.org/10.1182/blood-2016

Park, S., Cho, B. S., & Kim, H. J. (2020). New agents in acute myeloid leukemia (AML). *Blood Research*, *55*(S1), 14–18. https://doi.org/10.5045/br.2020.S003

Petroski, M. D., & Deshaies, R. J. (2005). Function and regulation of cullin-RING ubiquitin ligases. In *Nature Reviews Molecular Cell Biology* (Vol. 6, Issue 1, pp. 9–20). https://doi.org/10.1038/nrm1547

Pham, C. T. N. (2006). Neutrophil serine proteases: specific regulators of inflammation. *Nature Reviews Immunology 2006 6:7*, *6*(7), 541–550. https://doi.org/10.1038/nri1841

Rawlings, N. D., Waller, M., Barrett, A. J., & Bateman, A. (2014). MEROPS: the database of proteolytic enzymes, their substrates and inhibitors. *Nucleic Acids Research*, *42*(D1), D503–D509. https://doi.org/10.1093/NAR/GKT953

Reitsma, J. M., Liu, X., Reichermeier, K. M., Moradian, A., Sweredoski, M. J., Hess, S., & Deshaies, R. J. (2017). Composition and Regulation of the Cellular Repertoire of SCF Ubiquitin Ligases. *Cell*, *171*(6), 1326-1339.e14. https://doi.org/10.1016/j.cell.2017.10.016

Rosenberger, F. A., Thielert, M., & Mann, M. (2023). Making single-cell proteomics biologically relevant. *Nature Methods 2023 20:3*, *20*(3), 320–323. https://doi.org/10.1038/s41592-023-01771-9

Roukens, M. G., Alloul-Ramdhani, M., Moghadasi, S., Op den Brouw, M., & Baker, D. A. (2008). Downregulation of Vertebrate Tel (ETV6) and Drosophila Yan Is Facilitated by an Evolutionarily Conserved Mechanism of F-Box-Mediated Ubiquitination . *Molecular and Cellular Biology*, *28*(13), 4394–4406. https://doi.org/10.1128/mcb.01914-07

Rowe, J. M. (2019). Will new agents impact survival in AML? *Best Practice & Research Clinical Haematology*, *32*(4), 101094. https://doi.org/10.1016/J.BEHA.2019.101094

Sanjana, N. E., Shalem, O., & Zhang, F. (2014). Improved vectors and genome-wide libraries for CRISPR screening. *Nature Methods*, *11*(8), 783–784. https://doi.org/10.1038/NMETH.3047

Sarikas, A., Hartmann, T., & Pan, Z.-Q. (2011). The Cullin Protein Family. *Genome Biology*, *12*(220). http://genomebiology.com/2011/12/4/220

Scheffner, M., Nuber, U., & Huibregtse, J. M. (1995). Protein ubiquitination involving an E1-E2-E3 enzyme ubiquitin thioester cascade. *Nature*, *373*(6509), 81–83. https://doi.org/10.1038/373081A0

Schessl, C., Rawat, V. P. S., Cusan, M., Deshpande, A., Kohl, T. M., Rosten, P. M., Spiekermann, K., Humphries, R. K., Schnittger, S., Kern, W., Hiddemann, W., Quintanilla-Martinez, L., Bohlander, S. K., Feuring-Buske, M., & Buske, C. (2005). The AML1-ETO fusion gene and the FLT3 length mutation collaborate in inducing acute leukemia in mice. *The Journal of Clinical Investigation*, *115*. https://doi.org/10.1172/JCI24225

Schmidt, M. W., Mcquary, P. R., Wee, S., Hofmann, K., & Wolf, D. A. (2009). F-Box-Directed CRL Complex Assembly and Regulation by the CSN and CAND1. *Molecular Cell*, *35*, 586–597. https://doi.org/10.1016/j.molcel.2009.07.024

Schoenherr, C., Wohlan, K., Dallmann, I., Pich, A., Hegermann, J., Ganser, A., Hilfiker-Kleiner, D., Heidenreich, O., Scherr, M., & Eder, M. (2019). Stable depletion of RUNX1-ETO in Kasumi-1 cells induces expression and enhanced proteolytic activity of Cathepsin G and Neutrophil Elastase. *PLoS ONE*, *14*(12). https://doi.org/10.1371/journal.pone.0225977

Schopf, F. H., Biebl, M. M., & Buchner, J. (2017). The HSP90 chaperone machinery. *Nature Reviews. Molecular Cell Biology*, *18*(6), 345–360. https://doi.org/10.1038/NRM.2017.20

Schulman, B. A., Carrano, A. C., Jeffrey, P. D., Bowen, Z., Kinnucan, E. R. E., Finnin, M. S., Elledge, S. J., Harper, J. W., Pagano, M., & Pavletich, N. P. (2000). Insights into SCF ubiquitin ligases from the structure of the Skp1-Skp2 complex. *Nature*, *408*(6810), 381–386. https://doi.org/10.1038/35042620

Schuster, B., Hendry, L., Byers, H., Lynham, S. F., Ward, M. A., & John, S. (2007). Purification and identification of the STAT5 protease in myeloid cells. *Biochemical Journal*, *404*(1), 81–87. https://doi.org/10.1042/BJ20061877

Shalem, O., Sanjana, N. E., Hartenian, E., Shi, X., Scott, D. A., Mikkelsen, T. S., Heckl, D., Ebert, B. L., Root, D. E., Doench, J. G., & Zhang, F. (2014). Genome-scale CRISPR-Cas9 knockout screening in human cells. *Science*, *343*(6166), 84–87. https://doi.org/10.1126/SCIENCE.1247005/SUPPL_FILE/SHALEM.SM.PDF

Shaul, Y. D., & Seger, R. (2007). The MEK/ERK cascade: From signaling specificity to diverse functions. *Biochimica et Biophysica Acta (BBA) - Molecular Cell Research*, *1773*(8), 1213–1226. https://doi.org/10.1016/J.BBAMCR.2006.10.005

Sherman, B. T., Hao, M., Qiu, J., Jiao, X., Baseler, M. W., Lane, H. C., Imamichi, T., & Chang, W. (2022). DAVID: a web server for functional enrichment analysis and functional annotation of gene lists (2021 update). *Nucleic Acids Research*, *50*(W1), W216–W221. https://doi.org/10.1093/NAR/GKAC194

Shi, W., Feng, L., Dong, S., Ning, Z., Hua, Y., Liu, L., Chen, Z., & Meng, Z. (2020). FBXL6 governs c-MYC to promote hepatocellular carcinoma through ubiquitination and stabilization of HSP90AA1. *Cell Communication and Signaling*, *18*(1). https://doi.org/10.1186/s12964-020-00604-y

Skaar, J. R., Pagan, J. K., & Pagano, M. (2013). Mechanisms and function of substrate recruitment by F-box proteins. *Nature Reviews. Molecular Cell Biology*, *14*(6), 369–381. https://doi.org/10.1038/NRM3582

Skopek, R., Palusí Nska, M., Kaczor-Keller, K., Pingwara, R., Papierniak-Wygl, A., Schenk, T., Lewicki, S., Zelent, A., & Szymá Nski, Ł. (2023). Choosing the Right Cell Line for Acute Myeloid Leukemia (AML) Research. *International Journal of Molecular Sciences*, *24*(5377). https://doi.org/10.3390/ijms24065377

Stengel, A., Shahswar, R., Haferlach, T., Walter, W., Hutter, S., Meggendorfer, M., Kern, W., & Haferlach, C. (2020). Whole transcriptome sequencing detects a large number of novel fusion transcripts in patients with AML and MDS. *Blood Advances*, *4*(21), 5393–5401. https://doi.org/10.1182/bloodadvances.2020003007

Suh, E. J., Kim, T. Y., & Kim, S. H. (2006). PP2Cγ-mediated S-phase accumulation induced by the proteasome-dependent degradation of p21WAF1/CIP1. *FEBS Letters*, *580*(26), 6100–6104. https://doi.org/10.1016/J.FEBSLET.2006.10.005

Sun, C., Wang, G., Wrighton, K. H., Lin, H., Songyang, Z., Feng, X.-H., & Lin, X. (2016). Regulation of p27 Kip1 phosphorylation and G1 cell cycle progression by protein phosphatase PPM1G. In *Am J Cancer Res* (Vol. 6, Issue 10). www.ajcr.us/

Swatek, K. N., & Komander, D. (2016). Ubiquitin modifications. In *Cell Research* (Vol. 26, Issue 4, pp. 399–422). Nature Publishing Group. https://doi.org/10.1038/cr.2016.39

Tekcham, D. S., Chen, D., Liu, Y., Ling, T., Zhang, Y., Chen, H., Wang, W., Otkur, W., Qi, H., Xia, T., Liu, X., Piao, H. L., & Liu, H. (2020). F-box proteins and cancer: An update from functional and regulatory mechanism to therapeutic clinical prospects. *Theranostics*, *10*(9), 4150–4167. https://doi.org/10.7150/thno.42735

The, M., Samaras, P., Kuster, B., & Wilhelm, M. (2022). Reanalysis of ProteomicsDB Using an Accurate, Sensitive, and Scalable False Discovery Rate Estimation Approach for Protein Groups. *Molecular & Cellular Proteomics : MCP*, *21*(12). https://doi.org/10.1016/J.MCPRO.2022.100437

Thomas, X. (2019). Acute Promyelocytic Leukemia: A History over 60 Years-From the Most Malignant to the most Curable Form of Acute Leukemia. *Oncology and Therapy*, *7*, 33–65. https://doi.org/10.6084/m9.figshare.7479977

Tsang, M., Gantchev, J., Ghazawi, F. M., & Litvinov, I. V. (2017). Protocol for adhesion and immunostaining of lymphocytes and other non-adherent cells in culture. *BioTechniques*, *63*(5), 230–233. https://doi.org/10.2144/000114610/

Uhlén, M., Fagerberg, L., Hallström, B. M., Lindskog, C., Oksvold, P., Mardinoglu, A., Sivertsson, Å., Kampf, C., Sjöstedt, E., Asplund, A., Olsson, I. M., Edlund, K., Lundberg, E., Navani, S., Szigyarto, C. A. K., Odeberg, J., Djureinovic, D., Takanen, J. O., Hober, S., … Pontén, F. (2015). Proteomics. Tissue-based map of the human proteome. *Science (New York, N.Y.)*, *347*(6220). https://doi.org/10.1126/SCIENCE.1260419

Varadi, M., Anyango, S., Deshpande, M., Nair, S., Natassia, C., Yordanova, G., Yuan, D., Stroe, O., Wood, G., Laydon, A., Zídek, A., Green, T., Tunyasuvunakool, K., Petersen, S., Jumper, J., Clancy, E., Green, R., Vora, A., Lutfi, M., … Velankar, S. (2022). AlphaFold Protein Structure Database: Massively expanding the structural coverage of protein-sequence space with high-accuracy models. *Nucleic Acids Research*, *50*(D1), D439–D444. https://doi.org/10.1093/NAR/GKAB1061

Vick, B., Rothenberg, M., Sandhöfer, N., Carlet, M., Finkenzeller, C., Krupka, C., Grunert, M., Trumpp, A., Corbacioglu, S., Ebinger, M., André, M. C., Hiddemann, W., Schneider, S., Subklewe, M., Metzeler, K. H., Spiekermann, K., & Jeremias, I. (2015). An advanced preclinical mouse model for acute myeloid leukemia using patients' cells of various genetic subgroups and in vivo bioluminescence imaging. *PLoS ONE*, *10*(3). https://doi.org/10.1371/journal.pone.0120925

Wang, T., Wei, J. J., Sabatini, D. M., & Lander, E. S. (2014). Genetic screens in human cells using the CRISPR-Cas9 system. *Science*, *343*(6166), 80–84. https://doi.org/10.1126/SCIENCE.1246981/SUPPL_FILE/WANG.SM.PDF

Wang, T., Yu, H., Hughes, N. W., Liu, B., Kendirli, A., Klein, K., Chen, W. W., Lander, E. S., & Sabatini, D. M. (2017). Gene Essentiality Profiling Reveals Gene Networks and Synthetic Lethal Interactions with Oncogenic Ras. *Cell*, *168*(5), 890. https://doi.org/10.1016/J.CELL.2017.01.013

Wang, Z., Liu, P., Inuzuka, H., & Wei, W. (2014). Roles of F-box proteins in cancer. *Nature Reviews Cancer 2014 14:4*, *14*(4), 233–247. https://doi.org/10.1038/nrc3700

Weinstein, J. N., Collisson, E. A., Mills, G. B., Shaw, K. R. M., Ozenberger, B. A., Ellrott, K., Sander, C., Stuart, J. M., Chang, K., Creighton, C. J., Davis, C., Donehower, L., Drummond, J., Wheeler, D., Ally, A., Balasundaram, M., Birol, I., Butterfield, Y. S. N., Chu, A., … Kling, T. (2013). The cancer genome atlas pan-cancer analysis project. *Nature Genetics*, *45*(10), 1113–1120. https://doi.org/10.1038/ng.2764

Winston, J. T., Koepp, D. M., Zhu, C., Elledge, S. J., Wade Harper, J., & McLean, M. (1999). A family of mammalian F-box proteins. *Current Biology*, *9*(20), 1180–1182. http://www.ncbi.nlm.nih.gov/genbank/query_form.html.

Wirbelauer, C., Sutterlüty, H., Blondel, M., Gstaiger, M., Peter, M., Reymond, F., & Krek, W. (2000). The F-box protein Skp2 is a ubiquitylation target of a Cul1-based core ubiquitin ligase complex: evidence for a role of Cul1 in the suppression of Skp2 expression in quiescent fibroblasts. *The EMBO Journal*, *19*(20), 5362. https://doi.org/10.1093/EMBOJ/19.20.5362

Yada, M., Hatakeyama, S., Kamura, T., Nishiyama, M., Tsunematsu, R., Imaki, H., Ishida, N., Okumura, F., Nakayama, K., & Nakayama, K. I. (2004). Phosphorylation-dependent degradation of c-Myc is mediated by the F-box protein Fbw7. *The EMBO Journal*, *23*(10), 2116–2125. https://doi.org/10.1038/SJ.EMBOJ.7600217

Yan, M., Burel, S. A., Peterson, L. F., Kanbe, E., Iwasaki, H., Boyapati, A., Hines, R., Akashi, K., & Zhang, D. E. (2004). Deletion of an AML1-ETO C-terminal NcoR/SMRT-interacting region strongly induces leukemia development. *Proceedings of the National Academy of Sciences of the United States of America*, *101*(49), 17186–17191. https://doi.org/10.1073/PNAS.0406702101/SUPPL_FILE/06702FIG7.PDF

Yao, F., Zhou, Z., Kim, J., Hang, Q., Xiao, Z., Ton, B. N., Chang, L., Liu, N., Zeng, L., Wang, W., Wang, Y., Zhang, P., Hu, X., Su, X., Liang, H., Sun, Y., & Ma, L. (2018). SKP2- and OTUD1-regulated non-proteolytic ubiquitination of YAP promotes YAP nuclear localization and activity. *Nature Communications*, *9*(1). https://doi.org/10.1038/s41467-018-04620-y

Yates, J. R., Ruse, C. I., & Nakorchevsky, A. (2009). Proteomics by mass spectrometry: approaches, advances, and applications. *Annual Review of Biomedical Engineering*, *11*, 49–79. https://doi.org/10.1146/ANNUREV-BIOENG-061008-124934

Yu, Y., Yao, W., Wang, T., Xue, W., Meng, Y., Cai, L., Jian, W., Yu, Y., & Zhang, C. (2022). FBXL6 depletion restrains clear cell renal cell carcinoma progression. *Translational Oncology*, *26*, 101550. https://doi.org/10.1016/J.TRANON.2022.101550

Yu, Z. K., Gervais, J. L. M., & Zhang, H. (1998). Human CUL-1 associates with the SKP1/SKP2 complex and regulates p21(CIP1/WAF1) and cyclin D proteins. *Proceedings of the National Academy of Sciences of the United States of America*, *95*(19), 11324–11329. https://doi.org/10.1073/PNAS.95.19.11324

Zhong, X., Prinz, A., Steger, J., Garcia-Cuellar, M. P., Radsak, M., Bentaher, A., & Slany, R. K. (2018). HoxA9 transforms murine myeloid cells by a feedback loop driving expression of key oncogenes and cell cycle control genes. *Blood Advances*, *2*(22), 3137–3148. https://doi.org/10.1182/bloodadvances.2018025866

Zhou, P., & Howley, P. M. (1998). Ubiquitination and degradation of the substrate recognition subunits of SCF ubiquitin-protein ligases. *Molecular Cell*, *2*(5), 571–580. https://doi.org/10.1016/S1097-2765(00)80156-2